



**PREPARATION, ISOLATION AND CHARACTERIZATION OF
NANOCELLULOSE FROM SUGARCANE BAGASSE**

DITIRO VICTOR MASHEGO

Submitted in fulfilment of the academic requirements of the degree of

MASTER OF APPLIED SCIENCES IN CHEMISTRY

Faculty of Applied Sciences at the Durban University of Technology, Chemistry
Department, Durban, South Africa

AUGUST 2016

PREFACE

The work described in this thesis was performed by the author under the supervision of Professor. N. Deenadayalu at Durban University of Technology, Durban, South Africa and at the CSIR, NCNSM, Pretoria under the supervision of Professor Suprakas Sinha-Ray from 2014 – 2015. The study presents original work by the author and has not been submitted in any form to another university. Where use is made of the work of others, it has been clearly stated in the text.



Signed:

Date: 22 August 2016

Ditiro Victor Mashego



Signed:

Date: 22 August 2016

Prof. N. Deenadayalu (Supervisor)



Signed:

Date: 22 August 2016

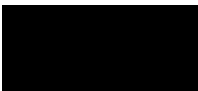
Dr. P. Reddy (Co-Supervisor)



Signed:

Date: 22 August 2016

Prof. S. Ray (Co-Supervisor)



Signed:

Date: 22 August 2016

Prof. A. Dufresne (C-Supervisor)

ACKNOWLEDGEMENTS

First and foremost, I thank God Almighty for the opportunity and privilege afforded to me to undertake this study, without whom nothing would have been possible. He has always been my strength in all things.

My deepest thanks go to my family and friends who were a constant pillar of support throughout my life. Their emotional support and company helped me through the hardest times.

I am indebted to the dedicated and accommodating staff of CSIR Nanotech, Pretoria for their skilful experimental assistance. Their expertise in characterization helped in thoroughly understanding the techniques used.

Finally, I would like to thank the National Research Foundation for funding the study and the Durban University of Technology for the facilities provided.

ABSTRACT

Cellulose is a sustainable, abundant biopolymer derived from a variety of living species such as plants, animals, bacteria and some amoebas. An attractive source of cellulose for industrial uses is agricultural waste, as this use does not jeopardize food supplies and improves the local rural economy. Sugarcane bagasse (SCB) is one of the main biomass wastes from sugar production and represents 30–40 wt % of sugar production waste. In 2008, South Africa produced on average 22 million tons of sugar cane each season from 14 sugar mill supply areas which resulted in 7,9 million tons of “waste” bagasse.

In this study cellulose nanocrystals were prepared from soda pulped sugarcane bagasse by acid hydrolysis followed by separation using centrifugation, ultrasonication and dialysis. Transmission Electron Microscopy (TEM) images showed nanocrystals of approximately 300 nm in length and 20 nm in width. Thermogravimetric Analysis and Differential Thermogravimetry (TGA and DTG) profiles of FD CNC, MCC and Pulped bagasse all had characteristic onset and decomposition temperatures indicating a change in the structure after chemical treatments. Particle size distribution measurements corroborated with the TEM and FE - SEM results and showed that the majority of the nanocrystals were in the 100 – 300 nm range. Attenuated Total Reflectance – Fourier Transform Infra Red (ATR - FTIR) analysis showed functional group changes as the amorphous regions of the polymer were removed revealing the ordered crystalline portions. These were further confirmed by an increase in the Lateral Orientation Index (LOI) of the samples as the nanocrystals were isolated. X - Ray Diffraction (XRD) Crystallinity Index (CrI) calculations showed a steady increase in the crystallinity of the materials from pulped bagasse to MCC to FD CNC.

CONTENTS	Page
<i>Preface</i>	<i>i</i>
<i>Acknowledgements</i>	<i>ii</i>
<i>Abstract</i>	<i>iii</i>
<i>Contents</i>	<i>iv</i>
<i>List of Tables</i>	<i>v</i>
<i>List of Figures</i>	<i>vi</i>
<i>List of Symbols</i>	<i>vii</i>
Chapter 1 INTRODUCTION	1
1.1 Sugarcane Bagasse	1
1.2 Sugarcane Bagasse Pulping	2
1.2.1 Desilication	2
1.2.2 Depithing	3
1.2.3 Alkali Treatment	3
1.2.4 Chlorite Bleaching	3
1.3 Cellulose	4
1.3.1 Introduction	4
1.3.2 Cellulose Nanocrystals	5
1.3.3 Morphology and Dimensions of cellulose nanocrystals	7
1.3.4 Applications of CNCs	9
1.3.5 Paper and paperboard	9
1.3.6 Food	9
1.3.7 Hygiene and adsorbent products	10
1.3.8 Medical, cosmetics and pharmaceutical	10
1.4 Characterization of CNCs	11
Chapter 2 THEORY OF INSTRUMENTATION	13
2.1 Dynamic Light Scattering	13
2.2 Fourier-Transform InfraRed- Attenuated Total Reflectance	15
2.3 Wide angle X-Ray Diffraction	17
2.4 Thermogravimetry and Differential Thermogravimetry	19
2.5 Atomic Force Microscopy	20

2.6	Field Emission- Scanning Electron Microscopy	21
2.7	Transmission Electron Microscopy	24
Chapter 3	LITERATURE REVIEW	28
Chapter 4	MATERIALS AND EXPERIMENTAL METHODOLOGY	58
4.1	Materials and methods	58
4.2	Experimental procedure	59
4.2.1	Neutralisation of pulped bagasse	59
4.2.2	Preparation of cellulose nanocrystals	60
4.2.3	Isolation of cellulose nanocrystals	61
4.3	Characterization of cellulose nanocrystals	61
4.3.1	Particle size determination	61
4.3.2	Thermogravimetry and Differential Thermogravimetry	61
4.3.3	Fourier Transform InfraRed spectroscopy	62
4.3.4	Wide angle X-Ray Diffraction	62
4.3.5	Atomic Force Microscopy	63
4.3.6	Scanning Electron Microscopy	63
4.3.7	Transmission Electron Microscopy	63
Chapter 5	RESULTS	64
5.1	Particle size determination	64
5.2	Thermogravimetry	67
5.2.1	Thermogravimetry	67
5.2.2	Differential Thermogravimetry	70
5.3	Fourier Transform InfraRed spectroscopy	72
5.4	Wide angle X-Ray Diffraction	74
5.5	Atomic Force Microscopy	77
5.6	Scanning Electron Microscopy	79
5.7	Transmission Electron Microscopy	88

Chapter 6	DISCUSSIONS	85
6.1	Dynamic Light Scattering	85
6.2	Fourier Transform InfraRed spectroscopy	87
6.3	Wide Angle X-Ray Diffraction	90
6.3.1	Crystallinity Index (CrI)	91
6.4	Thermogravimetry and Differential Thermogravimetry	93
6.5	Atomic Force Microscopy	95
6.6	Scanning Electron Microscopy	96
6.7	Transmission Electron Microscopy	97
Chapter 7	CONCLUSIONS & RECOMMENDATIONS	100
REFERENCES		102
APPENDICES		118
	<ul style="list-style-type: none"> • Paper submitted to South African Journal of Chemistry 	
Title	:Preparation, Isolation and Characterization of Cellulose Nanocrystals from Soda Pulped Bagasse	
Author(s)	:Ditiro V. Mashego, Prashant Reddy, Suprakas Ray, Alain Dufresne, Nirmala Deenadayalu	

List of Tables

		<i>Page</i>
Table 1.1	Mechanical Properties of Mechanical properties of crystalline cellulose, stainless steel, aluminium, softwood kraft pulp and Kevlar® fibre	16
Table 1.2	Morphological dimensions of previously isolated CNCs from different sources with different morphologies	18
Table 3.1	Summary of the references used in the literature review	55
Table 6.1	FTIR bands observed during the ATR-FTIR analysis	92
Table 6.2	The TCI and LOI indices calculated using FTIR transmission bands	94
Table 6.3	The The XRD peaks and their corresponding 2θ angles.	95
Table 6.4	The CrI indices of CNC prepared and isolated in recent years.	97

<i>List of Figures</i>		<i>Page</i>
Figure 1.1	The process diagram for the production of pulped sugarcane bagasse.	3
Figure 1.2	Amorphous and Crystalline regions of the cellulose polymer.	5
Figure 2.1	A Schematic diagram of a Dynamic Light Scattering instrument.	14
Figure 2.2	A schematic diagram of a Fourier Transform Infra-Red Spectrophotometer	16
Figure 2.3	A cross sectional diagram of an ATR Accessory	17
Figure 2.4	A schematic diagram of an X-ray Diffraction Spectrophotometer	18
Figure 2.5	A Schematic diagram representing a TGA Instrument layout	20
Figure 2.6	A schematic diagram of an Atomic force Microscope	21
Figure 2.7	A schematic diagram of a scanning electron microscope.	23
Figure 2.8	A schematic diagram of a transmission electron microscope	25
Figure 4.1	Dried soda pulped bagasse	58
Figure 4.2	The experimental procedure for the isolation of cellulose nanocrystals from pulped sugarcane bagasse.	59
Figure 4.2	OHAUS MB 35 Moisture Analyser	59
Figure 4.3	Experimental setup for the preparation of CNC	60
Figure 4.4		61
Figure 4.5		62
Figure 5.1	CNC Volume Data	66
Figure 5.2	CNC Number Data	67
Figure 5.3	CNC Number (Black) vs CNC Volume (RED)	67

Figure 5.4	MCC Volume Data	68
Figure 5.5	MCC Number Data	68
Figure 5.6	MCC Number (Black vs MCC Volume (Red)	69
Figure 5.7	The combined TGA profiles of pulped bagasse FD CNC and MCC	70
Figure 5.8	The TGA profile of FD CNC	70
Figure 5.9	The TGA profile of pulped bagasse	71
Figure 5.10	The TGA profile of MCC	71
Figure 5.11	The combined DTG profile of FD CNC, pulped bagasse And MCC	72
Figure 5.12	The DTG profile of FD CNC	72
Figure 5.13	The DTG profile of MCC	73
Figure 5.14	The DTG profile of pulped bagasse	73
Figure 5.15	The ATR-FTIR spectra of pulped bagasse	74
Figure 5.16	The ATR-FTIR profile of FD CNC	75
Figure 5.17	The ATR-FTIR spectrum of MCC	75
Figure 5.18	The combined ATR-FTIR spectra of pulped bagasse MCC and FD CNC	76
Figure 5.19	XRD diffractogram of pulped bagasse	77
Figure 5.20	XRD diffractogram of MCC	77
Figure 5.21	XRD diffractogram of FD CNC	78
Figure 5.22	The combined XRD diffractograms of CNC MCC and pulped bagasse	78
Figure 5.23	CNC 3D AFM micrograph	79
Figure 5.24	CNC height micrograph	80
Figure 5.25	CNC phase micrograph	80

Figure 5.26	CNC phase micrograph	81
Figure 5.27	Pulped bagasse SEM micrograph at X10 k magnification	82
Figure 5.28	Pulped bagasse SEM micrograph at X30k magnification	82
Figure 5.29	MCC SEM micrograph at x 5k Magnification	83
Figure 5.30	MCC SEM micrograph at x30k Magnification	83
Figure 5.31	CNC SEM micrograph at x 10k Magnification	84
Figure 5.32	CNC SEM micrograph at x 30k Magnification	84
Figure 5.33	CNC TEM micrograph showing agglomerated crystals deposited on carbon substrate	85
Figure 5.34	CNC TEM micrograph showing sonicated individual crystal	86
Figure 5.35	CNC TEM micrograph showing individual crystal dimensions	86
Figure 6.1	How tis with different aspect ratios are used to overcome tip convolution in AFM measurements	98
Figure 6.2	Magnified image of TEM micrograph (Figure 44)	101

List of Symbols

P = density

MPa = Mega pascals

GPa = Giga pascals

INTRODUCTION

1.1 Sugarcane Bagasse

The sugarcane plant, *Saccharum officinarum*, is used to produce sugar. The plant has 3 main sections namely the green tops, the millable stem and the roots. For sugar production the stem or stalk is milled and crushed at the front end of the mill where the sugarcane juice is extracted. The dry fibrous residue which is left over is called sugarcane bagasse. 70% of the bagasse produced is used as fuel to generate steam and electricity (Mandal and Chakrabarty 2011; Andrade and Colodette 2014) in a power station. The remainder is used to manufacture paper and paper products. All sugar mills in South Africa produce their own electricity by burning bagasse which makes them energy self-sufficient. Bagasse is composed of cellulose 45–55%, hemicellulose 20–25%, lignin 18–24%, Ash 1–4%, waxes <1% (on a washed and dried basis) (Rainey 2009). Bagasse is composed primarily of bast which is the outer lining of the stems and pith and the internal soft component of the stem after the removal of the juices. Conventionally sugarcane bagasse is separated into pith and refined fibre. Around 6 to 7% of the sugar industry bagasse is used to produce animal feed, paper and furfural products; 2% as pith in the production of animal feed, 4 to 5% as refined fibre by two South African paper mills while the net use of bagasse for furfural production is negligible. Due to its highly heterogeneous nature, bagasse is first treated before it is used in the paper making industry. The pith is believed to have a detrimental effect on paper making as it clogs the mat and retards draining of water from paper during paper production. A process called “depithing” is used to remove pith from the bagasse.

Depithing is believed to remove 30% of the shortest fibre material from the bagasse (Rainey 2009).

Currently bagasse is effectively used in the production process of paper although the mill receives no direct income from the bagasse; the savings in electricity costs are an indirect benefit to them.

The South African sugar industry has sugarcane growers extending from Northern Pondoland in the Eastern Cape to the Mpumalanga Lowveld. There are 14 operational sugar mills in South Africa and one central refinery. In the 2012/13 milling season, 371 662 hectares (ha) was used to plant sugar cane, of which 271 684 ha were harvested to produce 17.3 million tons of cane (SMRI 2013). These sugar mills produced nearly 6 million tons of bagasse.

1.2 Sugarcane Bagasse Pulping

The production of pulped sugarcane bagasse follows the process depicted below in flow diagram. The individual processes are explained in detail in the section that follows.

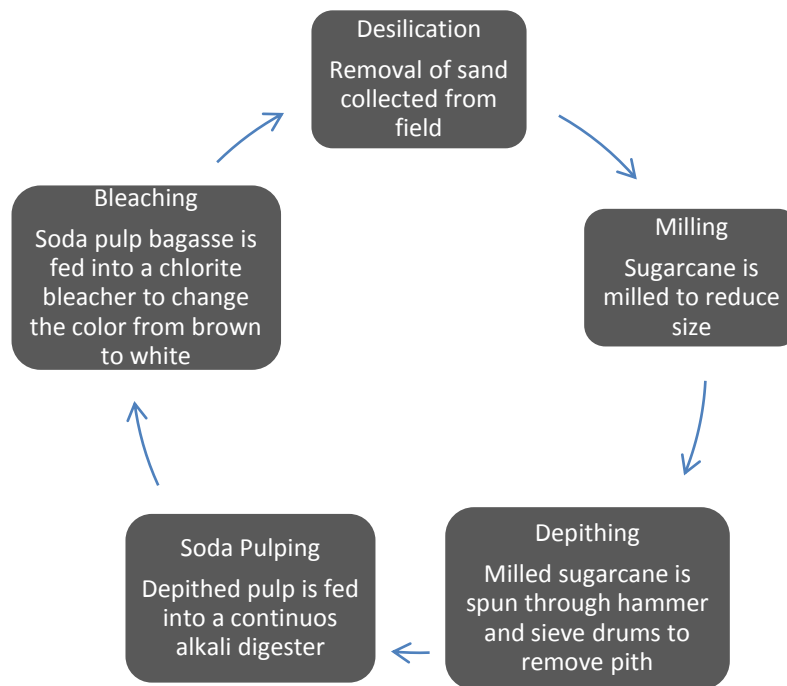


Figure 1.1 The process diagram for the production of pulped sugarcane bagasse.

1.2.1 Desilication

Raw bagasse contains a significant amount of sand, picked up from the harvesting grounds. The bagasse is washed but it still has a high silica content. Screening is performed so as to allow the silica to fall through the mesh and the bagasse is transported via a conveyor to the depithing drums.

1.2.2 Depithing

The milled bagasse contains significant amount of pith. Successfully removing the pith is necessary to produce a satisfactory pulp and to avoid wastage of chemicals. This pith removal is achieved by hammer-milling and screening to remove the pith as “fines”(Lois-Correa 2012). Pithed bagasse is added to a screened drum with rotating hammers. The

centrifugal force of the spinning drum allows adequate separation of the fine pith from the bagasse fibres.

1.2.3 Alkali Treatment

Soda (NaOH) pulping is traditionally the most used chemical pulping process for various non-wood raw materials including bagasse (Andrade and Colodette 2014). The desilicated and depithed bagasse is then passed via conveyor into a continuous alkali digester where it is loaded at fibre to liquor ratio of 5.5: 1. The alkali charged into the digester is of concentration 100-110 g/L and the temperature is ramped to 160 °C over a 45 minute period. The pulp is only removed from the continuous digester once it has an acceptable Kappa number of 12.5 - 13.5. Once the treated pulp is within specification it is washed with excessive water on a belt washer to decrease its pH from the alkali treatment and then passed by a conveyor to the next stage which is the chlorite bleaching.

1.2.4 Chlorite Bleaching

The washed bagasse is then added to second continuous digesters where is it treated with a chlorine dioxide (ClO₂) solution.

1.3 Cellulose

1.3.1 Introduction

Cellulose has been used for a long time as a source of energy, for building materials, paper, textiles and clothing. It is the most abundant natural polymer produced in the biosphere with an estimated production of over 1.5×10^{12} tons (Postek *et al.* 2013). It

is widely distributed in higher plants and marine animals. Wood consists of up to 50% cellulose and is the most important raw material source for cellulose. Cellulose consists of a linear homopolysaccharide composed of β -D-glucopyranose units linked together by β -1-4-linkages. The repeat unit is a dimer of glucose, known as cellobiose (Brinchi *et al.* 2013). Naturally occurring cellulose does not occur as an isolated individual molecule, but rather it is found as assemblies of individual cellulose chain-forming fibres. The fibrils in which these are orientated determine the morphological hierarchy, which pack into larger units called micro fibrils, which are in turn assembled into fibre. These microfibrils have disordered (amorphous) regions and highly ordered (crystalline) regions. In the crystalline regions, cellulose chains are closely packed together by a strong and highly intricate intra- and intermolecular hydrogen-bond network (Zhou and Wu 2012). Figure 1.1 below, shows how the crystallites are distributed within the cellulose polymer.

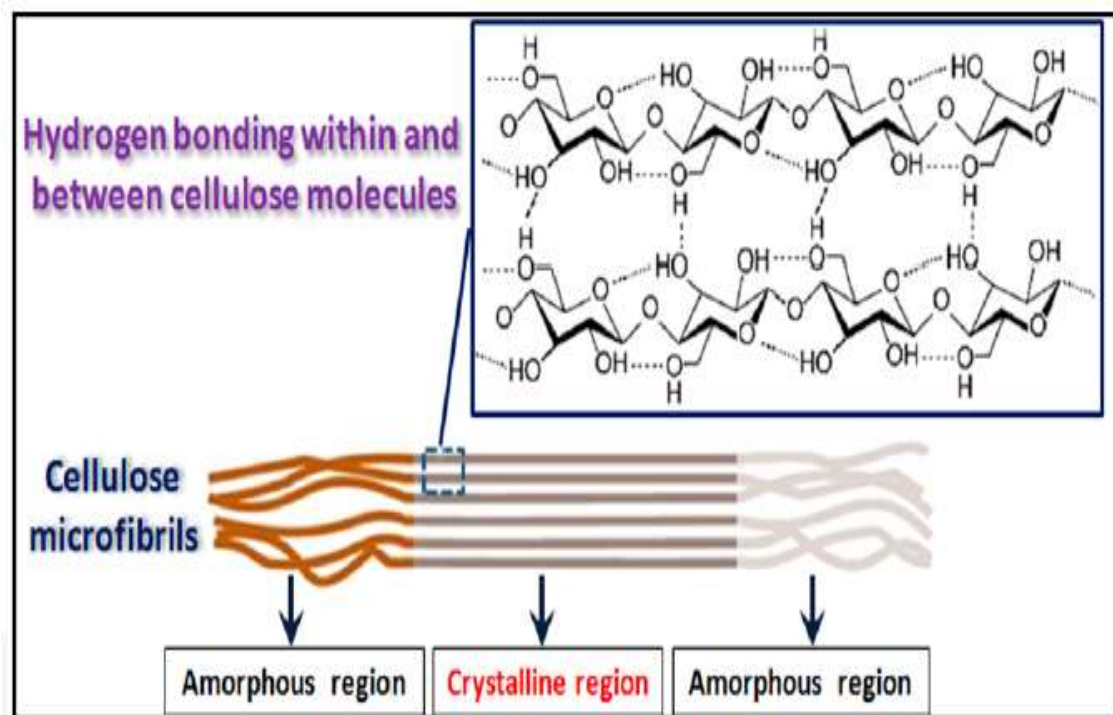


Figure 1.2 Amorphous and crystalline regions of the cellulose polymer.

Adapted from (Zhou and Wu 2012)

1.3.2 Cellulose Nanocrystals (CNCs)

Isolation of cellulose from plant fibres usually involves chemical treatments consisting of alkali extraction and bleaching. Due to its hierarchical structure and semi crystalline nature, cellulose nanoparticles can be easily extracted from naturally occurring biomass via a mechanical or chemical route. CNCs are also named as nanocrystals, whiskers, nanoparticles, nanocrystallites, nanofibers, or nanofibrils all of which are called “cellulose nanocrystals or CNC”. Recently cellulose nanocrystals proved to be a useful material on which to base a new polymer composite industry. CNCs contain very few defects and possess Young’s modulus potentially stronger than Kevlar® (Brinchi *et al.* 2013), and within the range of other reinforcement materials. Table 1.1 below shows the mechanical properties of various materials. All measurements were made using the TAPPI standard T 494 om-01 all tests are carried out at $23^{\circ}\text{C} \pm 1^{\circ}\text{C}$ and $50 \pm 2\%$ relative humidity.

Material	Tensile strength, MPa	Tensile modulus, GPa	Density , g/cm³
Crystalline Cellulose	7500 - 7700	110 – 220	1.6
302 Stainless Steel	1280	210	7.8
Aluminium	330	71	2.7
Softwood Kraft Pulp	700	20	1.5
Kevlar® KM2 fibre	3880	88	14

Table 1.1 Mechanical properties of crystalline cellulose, stainless steel, aluminium, softwood kraft pulp and Kevlar® fibre
Adapted from (Brinchi *et al.* 2013)

The advantages of using CNC are:

- high aspect ratio
- low density
- low energy consumption

- biodegradable
- biocompatible
- sources are renewable, sustainable, and highly abundant.

The abundant hydroxyl groups on the surface of CNCs render them reactive and the surface of CNCs can be modified with various chemical treatments to any desired surface modification, such as esterification, etherification, oxidation, silylation, or polymer grafting, which could successfully functionalize the CNCs and facilitate the incorporation and dispersion of CNCs into different polymer matrices. Due to the properties of CNCs mentioned above, academic and industrial interests have been directed toward the potential applications of CNCs in polymer-based nanocomposites for various fields, such as high performance materials, electronics, catalysis, biomedical, and energy (Zhou and Wu 2012).

1.3.3 Morphology and Dimensions of Cellulose Nanocrystals

The geometrical dimensions (length, L , and width, w) of CNCs vary greatly, depending on the source of the cellulosic material and the conditions under which the hydrolysis is performed. Cellulose nanocrystals show a notable decrease in dimensions and an increase in crystallinity when the hydrolysis time is increased. With excessive increase in the hydrolysis time and temperature, degradation of the CNCs is observed. A continuous and progressive decrease in the thermal stability of the nanoparticles occurs as the hydrolysis time increased, probably because of the high sulfation caused by the sulphuric acid on the surface of the nanocrystals (Sheltami *et al.* 2012). Size uniformity can be promoted by carefully monitoring the filtration, differential centrifugation or

ultracentrifugation steps. The size of CNCs can be studied by microscopy TEM, AFM, FE-SEM or light scattering techniques. Due to the drying step. TEM images usually show agglomerated CNC particles making it difficult to measure accurately measure the size of individual crystals. Typical geometrical characteristics for CNCs originating from different cellulose sources and obtained with a variety of techniques are summarized in Table 1.2. The reported width is generally approximately a few nanometres, but the length of CNCs spans a larger window, from tens of nanometres to several micrometres (Habibi, Lucia and Rojas 2010).

Source	L(nm)	W (nm)	Characterization Technique	Reference
Bacterial	100 - 1000	10 – 50	TEM	(Araki and Kuga 2001)
	100 - 1000	5-10 x 30-50	TEM	(Grunert and Winter 2002; Roman and Winter 2004)
Cotton	100 - 150	5 – 10	TEM	(Araki, Wada and Kuga 2001)
	70 - 170	~7	TEM	(Dong <i>et al.</i> 2012)
	200-300	8	TEM	(Dong <i>et al.</i> 1996)
	255	15	TEM	(Heux, Chauve and Bonini 2000)
	150-210	5 – 11	DDL	(Souza-Lima <i>et al.</i> 2003)
cotton linter	100 -200	10 – 20	SEM-FEG	(M. Roohani 2008)
	25 - 320	6 – 70	TEM	(Elazzouzi-Hafraoui <i>et al.</i> 2008)
	300 - 500	15 – 30	AFM	(Q. Li 2009)
MCC	35 - 265	3 – 48	TEM	(Elazzouzi-Hafraoui <i>et al.</i> 2008)
	250 - 270	23	TEM	(Capadona <i>et al.</i> 2009)
	~500	10	AFM	(Pranger and Tannenbaum 2008)
Ramie	150 - 250	6 – 8	TEM	(Habibi <i>et al.</i> 2008)
	50 - 150	5 – 10	TEM	(Menezes <i>et al.</i> 2009)
Sisal	100 - 500	3 – 5	TEM	(N. L. Garcia de Rodriguez 2006)
	150 - 280	3.5 – 65	TEM	(Siqueira, Bras and Dufresne 2009)
Tunicate		8.8 x 18.2	SANS	(Terech, Chazeau and Cavaille 1999)
	1160	16	DDL	(Souza-Lima <i>et al.</i> 2003)
	500 - 1000	10	TEM	(Anglès and Dufresne 2000)

	1000 - 3000	15- 30	TEM	(Kimura <i>et al.</i> 2005)
	1073	28	TEM	(Heux, Chauve and Bonini 2000)
Valonia	>1000	10 – 20	TEM	(Elazzouzi-Hafraoui <i>et al.</i> 2008)
soft wood	100 - 200	3 – 4	TEM	(Araki <i>et al.</i> 1998, 1999)
	100 - 150	4 – 5	AFM	(S. Beck-Candanedo 2005)
hard wood	140 - 150	4 – 5	AFM	(S. Beck-Candanedo 2005)

Table 1.2 Morphological dimensions of previously isolated CNCs from different
Adapted from literature (Habibi, Lucia and Rojas 2010)

1.3.4 Applications of CNCs

Biocomposites consisting of the polymer matrix and natural cellulose fibres are environmentally-friendly materials which can replace glass fibre-reinforced polymer composites, and are currently used in a wide range of fields such as the automotive and construction industries, electronic components, sports and leisure (Thakur 2015). Nanocellulose can also be used to make aerogels and foams, either homogeneously or in composite formulations. Nanocellulose-based foams are being considered for packaging applications as an alternative to polystyrene-based foams.

1.3.5 Paper and paperboard

CNC have potential application (Missoum *et al.* 2013) in the paper and paperboard industry where they can increase the fibre-fibre bond strength and thereby increasing the strength of the paper (Ahola, Österberg and Laine 2008; Eriksen, Syverud and Gregersen 2008; Taipale *et al.* 2010). CNCs can also be used as a barrier in grease-proof type of papers and as a wet-end additive to enhance retention, dry and wet strength

in commodity type of paper and board products (Hubbe *et al.* 2008; Syverud and Stenius 2009; Aulin, Gällstedt and Lindström 2010; Lavoine *et al.* 2013).

1.3.6 Food

As a food thickener, nanocellulose can be used as a low calorie replacement for carbohydrate additives, as a flavour carrier and suspension stabilizers. It can also be used to produce fillings, crushes, chips, wafers, soups, gravies, puddings etc. The food applications of CNCs were one of the earliest applications of nanocellulose due to the rheological behaviour of the nanocellulose gel.

1.3.7 Hygiene and absorbent products

Different applications in this field include but are not limited to:

- super water absorbent (e.g. material for incontinence pads material)
- nanocellulose used together with super absorbent polymers
- nanocellulose in tissue, non-woven products or absorbent structures
- antimicrobial films

1.3.8 Medical, cosmetic and pharmaceutical

The use of nanocellulose in cosmetics and pharmaceuticals was also early recognized.

A wide range of high-end applications have been suggested:

- freeze-dried nanocellulose aerogels used in sanitary napkins, tampons, diapers or as wound dressing
- the use of nanocellulose as a composite coating agent in cosmetics e.g. for hair, eyelashes, eyebrows or nails
- a dry solid nanocellulose composition in the form of tablets for treating intestinal disorders
- nanocellulose films for screening of biological compounds and nucleic acids encoding a biological compound
- filter medium partly based on nanocellulose for leukocyte free blood transfusion
- a buccodental formulation, comprising nanocellulose and a polyhydroxylated organic compound
- powdered nanocellulose has also been suggested as an excipient or bulking agent in pharmaceutical compositions. An excipient is a natural or synthetic substance formulated alongside the active ingredient of a medication, included for the purpose of bulking-up formulations that contain potent active ingredients
- nanocellulose in compositions of a photoreactive noxious substance purging agent
- elastic cryo-structured gels for potential biomedical and biotechnological application (Syverud and Stenius 2009).

1.4 Characterization of CNC

The morphology of CNCs have been extensively studied. Imaging techniques like as transmission electron microscopy (TEM), scanning electron microscopy (SEM), atomic force microscopy (AFM) are used to determine the CNC morphology and rheology. Wide angle X-ray scattering (WAXS), Fourier-Transform Infra-Red spectroscopy (FTIR) and Raman spectroscopy (RS) are used in the determination of the crystallinity index (CrI), lateral orientation index (LOI) and total crystallinity index (TCI) of the CNCs. Dynamic light scattering techniques (DLS) have also been used to determine the particle size distribution of CNCs. Small incidence angle X-ray diffraction (SAXRD) and solid state ^{13}C cross-polarization magic angle spinning nuclear magnetic resonance (CP/MAS NMR) spectroscopy have been and are currently used to characterize nanocellulose morphology (Mariño *et al.* 2015). These methods have typically been applied for the investigation of dried nanocellulose morphology.

Microscopic techniques such as TEM and SEM require the CNC to be dried. The drying process causes the nanocrystals to agglomerate which makes it difficult to accurately determine the length of a single crystal. It has been reported that nanocellulose suspensions may not be homogeneous and that they consist of various structural components, including cellulose nanocrystals, nanofibrils and nanofibril bundles.

THEORY OF INSTRUMENTS USED IN THIS WORK

2.1 Dynamic Light Scattering

Most Dynamic Light Scattering (DLS) instruments operate by measuring the intensity of light scattered by sample molecules as a function of time. Stationary sample molecules will scatter a constant amount of light at any given time. During the scattering of light, some light referred to as incident light is scattered and some is not. However, since all molecules in solution undergo Brownian motion in relation to the detector there will be interference (constructive or destructive) which causes a change in light intensity. Constructive and destructive interferences within the scattered light occur as a result of the diffusion of the particles within the sample according to Brownian motion with respect to the detector. A schematic representation of a typical dynamic light scattering instrument is given below in Figure 2.2. By measuring the time scale of light intensity fluctuations, DLS can provide information regarding the average size, size distribution, and polydispersity of molecules and particles in solution.

Particles within the sample which diffuse faster will result in the intensity of scattered light to change faster (if the light was bright enough this would be seen as a twinkling effect).

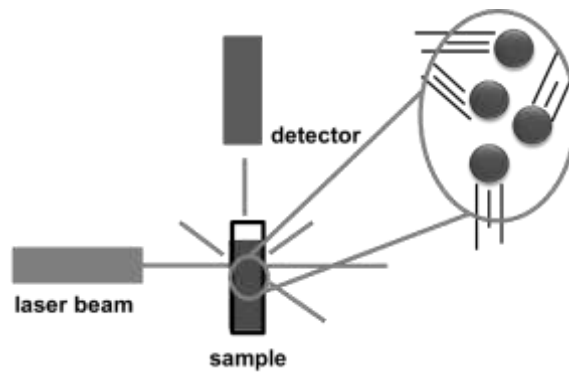


Figure 2.1 A Schematic diagram of a Dynamic Light Scattering instrument.

Adapted from (Nanotechnology 2013)

The speed at which the scattered light changes is thus directly related to the motion of the particles. Molecular diffusion within the sample is affected by the following factors:

- temperature – the higher the temperature the faster the molecules will move
- viscosity of the Solvent – the more viscous the solvent the slower the molecules move
- the size of the molecules – the bigger the molecules, the slower they move

If the temperature and solvent viscosity are constant and known, the variation in the intensity of the scattered light is directly related to the “size” of the molecules. This number is referred to as the hydrodynamic radius (R_h). The hydrodynamic radius is the sphere defined by the molecule rotating in all directions plus the hydration layer, modified by how easy it is to pass the solvent through that volume. It is actually a measure of how easy it is to move the molecule through the solvent.

2.2 Fourier Transform Infra-Red Spectroscopy – Attenuated Total Reflectance

Infrared (IR) spectroscopy is a simple, rapid, and non-destructive instrumental technique that can give evidence for the presence of various functional groups. Infrared spectroscopy depends on the interaction of molecules or atoms with electromagnetic radiation. Infrared radiation causes atoms and groups of atoms of organic compounds to vibrate with increased amplitude about the covalent bonds that connect them. Since the functional groups of organic molecules include specific arrangements of bonded atoms, absorption of IR radiation by an organic molecule will occur at specific frequencies characteristic of the types of bonds and atoms present in the specific functional groups of that molecule. These vibrations are quantized, and as they occur, the compounds absorb IR energy in particular regions of the IR portion of the spectrum (Solomon and Fryhle 2011).

Fourier-transform infrared (FTIR) spectroscopy is based on the idea of the interference of radiation between two beams to yield an interferogram. The interferogram is a signal produced as a function of the change of path length between the two beams. The two domains of distance and frequency are interconvertible by the mathematical method of Fourier-transformation. The basic components of an FTIR spectrometer are shown schematically in Figure 2.3 below. The radiation emerging from the source is passed through an interferometer to the sample before reaching a detector. Upon amplification of the signal, in which high-frequency contributions have been eliminated by a filter, the data are converted to digital form by an analog-to-digital converter and transferred to the computer for Fourier-transformation (Stuart 2005).

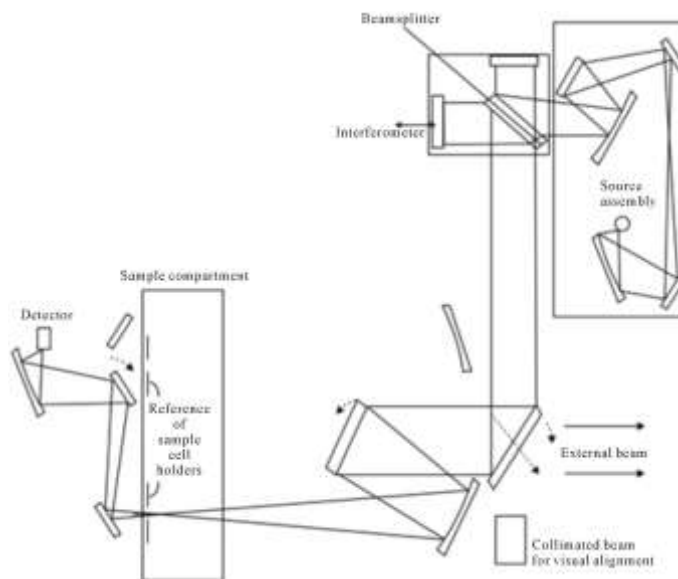


Figure 2.2 A schematic diagram of a Fourier Transform Infra-Red Spectrophotometer

Adapted from literature (Kumar *et al.* 2014)

Attenuated Total Reflectance (ATR) has become the world's most widely used FTIR sampling tool. Speed of analysis is greatly increased by the decrease in sample preparation times, sometimes requiring no sample preparation at all. It also allows for qualitative and quantitative analyses. The main benefit of ATR sampling comes from the very thin sampling path length or depth of penetration of the IR beam into the sample. This is in contrast to traditional FTIR sampling by transmission where the sample must be diluted with IR transparent salt, pressed into a pellet or pressed to a thin film, prior to analysis to prevent totally absorbing bands in the infrared spectrum. (Technologies 2005)

Using ATR sampling, the IR beam is directed into a crystal of relatively higher refractive index than the sample. The IR beam reflects from the internal surface of the crystal and creates an evanescent wave which projects orthogonally into the sample in

contact with the ATR crystal. Some of the energy of the wave is absorbed by the sample and the reflected radiation is returned to the detector. An ATR accessory operating on this principle is shown in Figure 2.4.

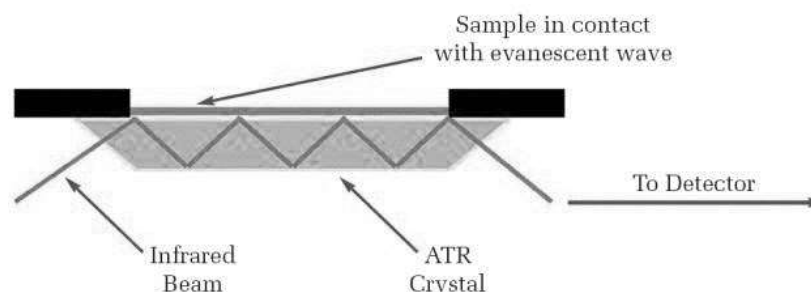


Figure 2.3 A cross sectional diagram of an ATR Accessory
Adapted from Literature(Perkin-Elmer 2005)

2.3 Wide-angle X-Ray Diffraction

X-ray diffraction is a rapid analytical technique that can provide characteristic information on unit cell dimension and is primarily used in the phase identification of crystalline materials. It is based on the constructive interference of monochromatic x-ray radiation and a crystalline material. These x-ray radiation is sourced from a cathode-ray tube and filtered to produce the required monochromatic interference and a diffracted ray are produced by the interaction of the monochromatic radiation and the sample when Bragg's Law is satisfied. This law relates the wavelength of electromagnetic radiation to the diffraction angle and the lattice spacing in a crystalline sample. These diffracted X-rays are then detected, processed and counted. By scanning the sample through a range of 2θ angles, all possible diffraction directions of the lattice should be attained due to the random orientation of the powdered material. Conversion of the diffraction peaks to d-spacings allows identification of the mineral because each

mineral has a set of unique d-spacings. Typically, this is achieved by comparison of d-spacings with standard reference patterns (College 2015). Figure 2.5 below shows a schematic diagram of a typical x-ray diffractometer.

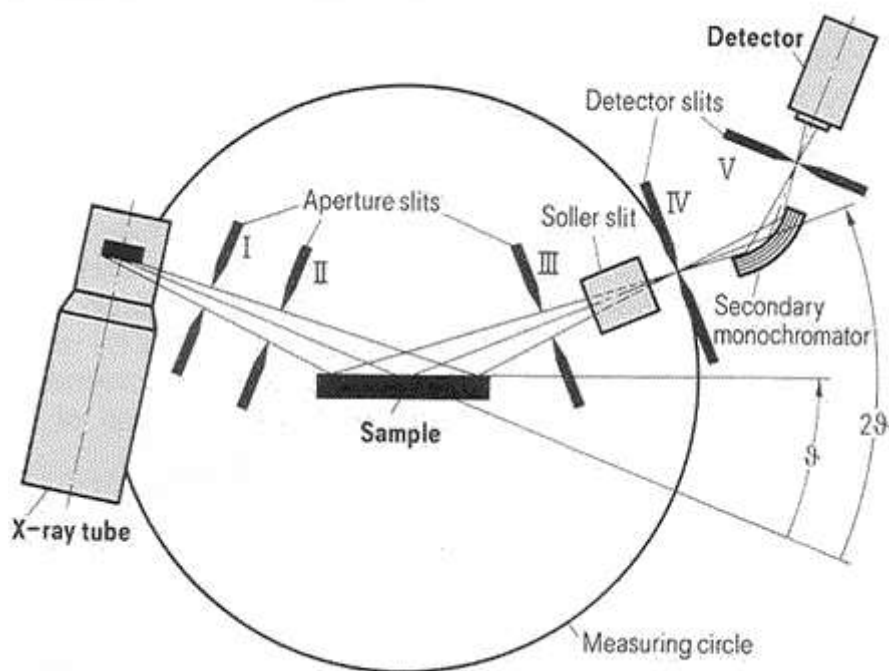


Figure 2.4 A schematic diagram of an X-ray Diffraction Spectrophotometer
Adapted from (Online 2015)

X-ray diffraction (XRD) is principally used to determine the crystalline structure of materials. Powder diffraction is mainly used for “finger print identification” of various solid materials. It is a rapid and non-destructive technique where a finely ground, homogenous sample is analysed to give a unique crystalline pattern. XRD is also used to determine the spaces between atoms and their orientation in crystalline materials.

2.4 Thermogravimetry and Differential Thermogravimetry

Thermogravimetry (TG) is the branch of thermal analysis dedicated to understanding the mass change of a sample in one of two modes, as a function of temperature in the scanning mode or as a function of time in the isothermal mode. Thermal events such as melting, crystallization or glass transition do not result in a change in the mass of the sample. Desorption, absorption, sublimation, vaporization, oxidation, reduction and decomposition are thermal which result in changes in sample mass under investigation. Thermogravimetry is extensively used in the characterization of the decomposition and thermal stability of materials under a variety of conditions and to examine the kinetics of the physicochemical processes occurring in the sample. Thermogravimetric curves are characteristic for a given polymer or compound because of the unique sequence of the physiochemical reaction that occurs over specific temperature ranges and heating rates and are function of the molecular structure.

The four main components of the thermogravimetric instrument are the microbalance, the furnace, the programmer controller, and a computer or data acquisition system. A typical schematic of the components for TGA are shown in Figure 2.6 below.

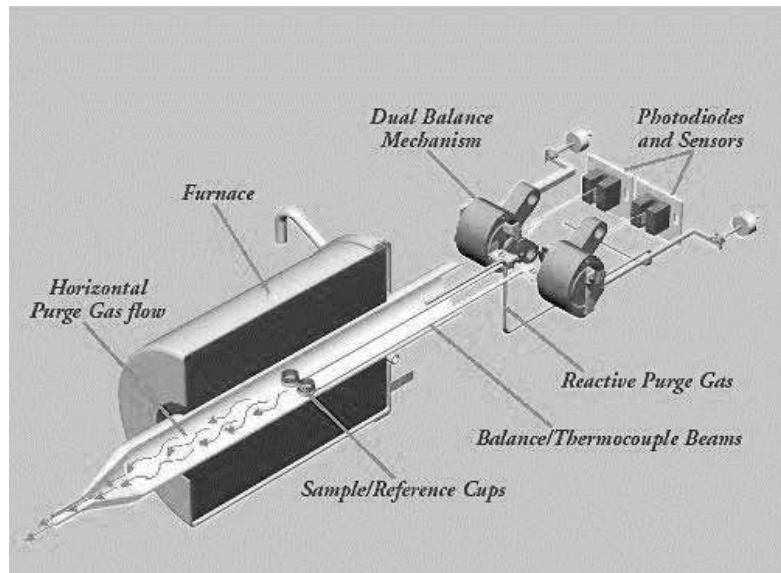


Figure 2.5 A Schematic diagram representing a TGA Instrument layout

Adapted from (University 2012)

Changes in mass are characteristic for each material and strongly depend on the experimental conditions employed. Independent factors such as sample mass, volume and physical form, the shape and nature of the sample holder, the nature and pressure of the atmosphere in the sample chamber, and the scanning rate have significant influences on the characteristics of the recorded TG curve. As the temperature is increased, the sample can undergo absorbed water loss because of waters of crystallization and decomposition of the sample.

2.5 Atomic Force Microscopy

Atomic force microscopy (AFM) or scanning force microscopy (SFM) is a very high-resolution type of scanning probe microscopy (SPM), with demonstrated resolution on the order of fractions of a nanometre, which is more than 1000 times better than the optical diffraction limit. AFM uses a sharp probe tip which is scanned over the surface of a sample and measures the changes in force between the probe tip and the sample. Depending on this separation distance, long range or short range forces will dominate

the interaction. This force is measured by the bending of the cantilever by an optical lever technique: a laser beam is focused on the back of a cantilever and reflected into a photodetector. Small forces between the tip and sample will cause less deflection than large forces. By raster-scanning the tip across the surface and recording the change in force as a function of position, a map of surface topography and other properties can be generated. Figure 2.7 below shows a schematic diagram of an Atomic Force Microscope.

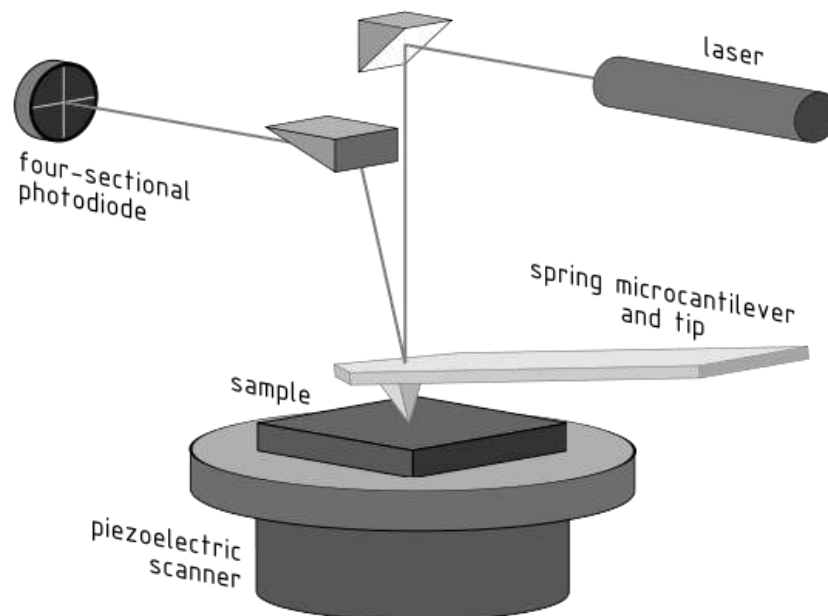


Figure 2.6 A schematic diagram of an Atomic force microscope

Adapted from (Wikipedia 2014)

2.6 Field Emission Scanning Electron Microscopy

The Field Emission Scanning Electron Microscope (FESEM) is microscope that works with electrons instead of light. These electrons are liberated by a field emission source. The object is scanned by electrons according to a zig-zag pattern. The Scanning electron

Microscope (SEM) has allowed researchers to examine a much bigger variety of specimens. The scanning electron microscope has many advantages over traditional microscopes. The SEM has a large depth of field, which allows more of a specimen to be in focus at one time. The SEM also has much higher resolution, so closely spaced specimens can be magnified at much higher levels. Because the SEM uses electromagnets rather than lenses, the researcher has much more control in the degree of magnification.

Traditional microscopes are dwarfed by the scanning electron microscope when resolution, depth of view and multiple specimen magnification is concerned. The high resolution imagery produced by the SEM and the use of magnet over lenses provide superior control and a higher degree of magnification. All of these advantages, as well as the actual strikingly clear images, make the scanning electron microscope one of the most useful instruments in research today (University 2014).

FESEM provides topographical and elemental information at magnifications of 10x to 300,000x, with virtually unlimited depth of field. Compared with convention scanning electron microscopy (SEM), field emission SEM (FESEM) produces clearer, less electrostatically distorted images with spatial resolution down to 1 1/2 nanometres – three to six times better (PhotometricsInc. 2012).

A FESEM has a hot cathode source, usually a tungsten filament similar to that in an incandescent light bulb. The filament is located inside the electron gun. When this filament is heated by passing current through it, it emits light and an electron cloud

forms around the filament. Left on their own, they remain in the cloud and are reabsorbed into the filament when the current is removed.

A positively charged plate (an anode) near the filament and the electron cloud directs the electrons away from the filament. The electron cloud is attracted to the anode plate that the electrons will travel through the hole in the cathode. But in doing so, they gain enough speed that most of them travel right through the hole in the anode plate. This is known as the electron gun. Figure 2.8 below shows a schematic diagram of a scanning electron microscope.

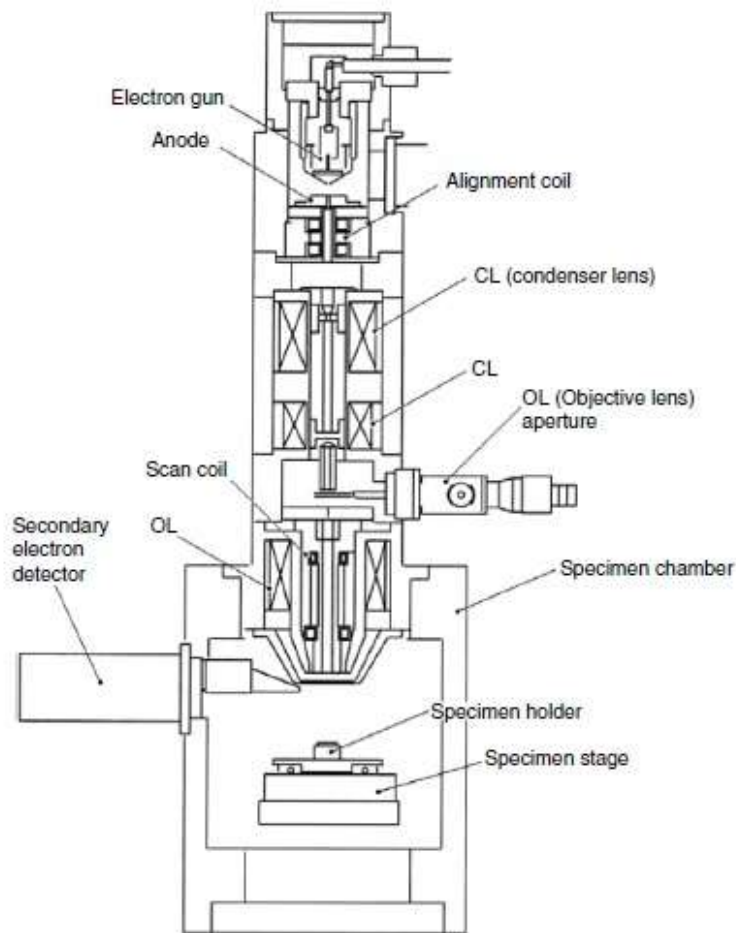


Figure 2.7 A schematic diagram of a field emission scanning electron microscope.

Adapted from Literature (Zhou *et al.* 2007)

The speed of the electrons emitted from this gun is controlled by the amount of potential (accelerating voltage) applied to the cathode and anode plates.

The electrons from the gun come out in almost a spray pattern. An electromagnetic lens is a relatively simple device. By applying current to wire coiled around an iron cylindrical core, a magnetic field is created which acts as a lens. The electromagnetic lenses and electron gun are arranged in a column above the sample chamber. The condenser lens controls the size of the beam, or the amount of electrons traveling down the column. Increasing the size of the beam achieves a better signal to noise ratio, but because the beam diameter is larger, it gives a lower resolution. Depending on the magnification, a compromise between signal to noise and resolution achieves the best image quality.

Sets of plates are positioned around the beam and varying the potential between them, the electron beam can be deflected. If these plates are attached to a scan generator, the beam can be made to scan lines across the sample. The objective lens focuses the beam into a spot on the sample. This is necessary to have an image in proper focus.

2.7 Transmission Electron Microscopy

A transmission electron microscope (TEM) forms an image of an object by firing a beam of electrons through the specimen. The TEM has a high-voltage electricity supply that powers a heated filament called the cathode. The cathode is part of the electron gun. This produces a beam of high energy electrons. The first set of lenses of the TEM, as shown in Figure 2.9 are the condenser lenses, also known as a magnetic lens, concentrates the electrons into a powerful beam. This beam is focused onto specific

parts of the specimen via a set electromagnetic coils. These coils are called the beam deflection coils. The specimen is usually placed on a copper grid and the beam is allowed to pass through it. After the image has been collected it is magnified by a third set of electromagnetic coils, the projection lens. At the base of the machine, a fluorescent screen, the imaging plate, is positioned so that when the beam from the third coil interacts with it an image is formed.

The electron source consists of a cathode and an anode. The cathode is a tungsten filament which emits electrons when being heated. A negative cap confines the electrons into a loosely focused beam. The beam is then accelerated towards the specimen by the positive anode. Electrons at the rim of the beam will fall onto the anode while the others at the centre will pass through the small hole of the anode. The electron source works like a cathode ray tube. Figure 2.9 below shows a schematic diagram of a transmission electron microscope.

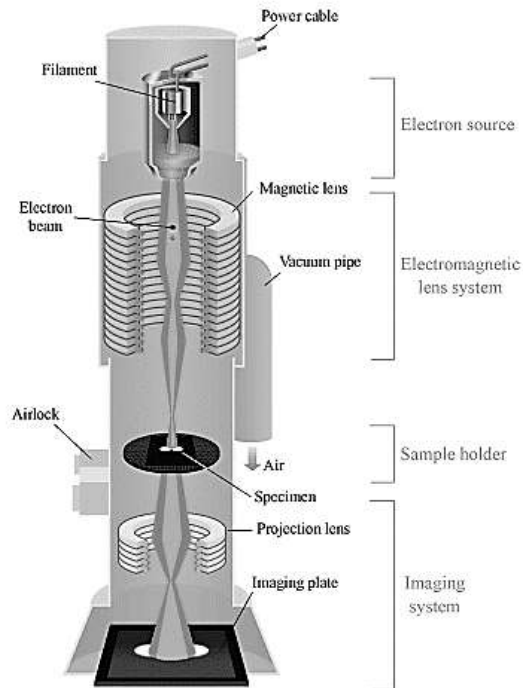


Figure 2.8 A schematic diagram of a transmission electron microscope
Adapted from (Kong 2013)

After leaving the electron source, the electron beam is focused using electromagnetic lens and metal apertures. The discriminatory system only allows electrons within a small energy range to pass through, so the electrons in the electron beam will have a well-defined energy. The electrons are focused by magnetic lenses. These are circular electro-magnets which are used to generate a precise and well defined magnetic field focusing the electrons. A thin disk with a small circular hole is used to restrict the electron beam and filter out unwanted electrons before hitting the specimen. This is called the aperture.

The beam is then passed through the sample positioned on the sample holder and is passed on to the imaging system. The imaging system consists of another

electromagnetic lens system and a screen. The electromagnetic lens system contains two lens systems, one for refocusing the electrons after they pass through the specimen, and the other for enlarging the image and projecting it onto the screen. The screen has a phosphorescent plate which glows when being hit by electrons. Image forms in a way similar to photography (Kong 2013).

LITERATURE REVIEW

Sun *et al.* 2004 from the College of Forestry in the North-Western Science and Technology University of Agriculture and Forestry, Yangling, China isolated cellulose from sugarcane bagasse. Varied concentration of alkali, alkali peroxide, acidic sodium chlorite and an 80% acetic acid and 70 % nitric acid mixture were utilized to yield pure cellulose fractions. The resulting cellulose fraction was subjected to acid hydrolysis and characterized. FT-IR studies showed a decrease in lignin-associated absorbance at 1600 and 1510 cm^{-1} (Sun *et al.* 2004). Slight acetylation was achieved using the acetic-nitric acid mixture, which was evident by an appearance of a band in acetyl ester bands at 1745 ($\text{C}=\text{O}$ ester), 1374 cm^{-1} ($-\text{C}-\text{CH}_3$), and $-\text{C}-\text{O}-$ stretching band at 1261 cm^{-1} (Sun *et al.* 2004). ^{13}C -NMR studies revealed a decrease in the crystallinity of the cellulose via the presence of peaks located up field at 62.4 and 64.8 ppm. These peaks were attributed to the C-6 in cellulose. The study revealed a decrease in the amorphous cellulose content. Though the amorphous content was removed, no notable increase in crystallinity was observed. The ^{13}C -NMR results revealed that the crystallinity of cellulose decreased with the treatment of SCB with acidified sodium chlorite followed by alkali extraction or with an acetic acid-nitric acid mixture extraction under the condition given (Sun *et al.* 2004). Thermal decomposition studies revealed that cellulose preparations with a higher purity were more thermally stable. The TGA curves showed that the decomposition of the cellulose ranged between 205 °C to 305 °C. The DSC thermograms showed exothermic peaks at 205 °C and 430 °C. These peaks were attributed to the thermal disintegration of the cellulose polymer. The study revealed that alkali and acetic-nitric acid mixture delignification of SCB was a viable method for the isolation of cellulose from SCB. Slight acetylation and degradation of the close fibers was also noted.

Zhang *et al* 2007 from the School of Chemistry and Biochemistry, Georgia Institute of Technology, Atlanta, USA synthesized spherical nanoparticles with a wide range in particle size from cellulose fibers. Acid hydrolysis using 36.0 N sulphuric acid was used which yielded spherical nanoparticles. The resulting fiber slurry turned into a milky colloid suspension. It contained different sizes of nanocrystalline cellulose particles (Zhang *et al.* 2007). Capillary electrophoresis was used to determine the electrophoretic motilities of the particles in pure water. AFM studies showed phase and amplitude micrograms of nanocrystals from acid hydrolysis with dimensions of 470 ± 100 nm (2.5 micron scan) (Zhang *et al.* 2007). These were ultra-sonicated at pH 2.5 in an HCl-H₂SO mixture (3:1) (Zhang *et al.* 2007) to monitor changes in particle dimensions as a function of treatment time. The ultrasonication yielded cellulose nanoparticles of diameter 570–60 nm (Zhang *et al.* 2007). High resolution SEM imaging showed spherical nanoparticles with average diameter of 85nm. TEM micrographs showed that the nanoparticles form was generally spherical in shape with an aspect ratio of 0.91 -1.10. ¹³C CP/MAS NMR was used to determine the degree of crystallinity of the produced nanoparticles. The initial pulp had a crystallinity index of 0.61. After alkaline and DMSO pretreatment the crystallinity index then dropped to 0.58. The final spherical nanoparticles had a crystallinity index of 0.82. The final rise in crystallinity was attributed to the acid hydrolysis which favors the degradation of amorphous cellulose. XRD studies performed on the nanoparticles, the starting material and intermediates corresponded with the ¹³C CP/MAS NMR data and also with other values from literature (Zhang *et al.* 2007).

Troedec *et al.* 2008 from the GEMH-ENSCI Group d'Etude des Matériaux Hétérogénés, Ecole Nationale Supérieure de Céramique Industrielle, Limoges Cedex, France studied the influence

of various chemical treatments on the composition and structure of hemp fibers using sodium hydroxide (NaOH), ethylene diamine tetra acetic acid (EDTA), polyethylenimine (PEI), calcium hydroxide ($\text{Ca}(\text{OH})_2$) and calcium chloride (CaCl_2) as chemicals of interest. Each considered treatment modifies either the chemical nature of the surface of natural fibers, or the surface state, like the charge or the conformation of polymers (Troedec *et al.* 2008). NaOH treatments at pH 14 was found to successfully remove waxes and oils on the surface of the hemp fibers. Similar results were obtained with PEI. However, digestion of the fibers in $\text{Ca}(\text{OH})_2$ solution resulted in the deposition of calcium containing nodules on the surface of the fibers (Troedec *et al.* 2008). Immersion of the fibers in a neutral CaCl_2 solution did not have any notable effect on the surface of the hemp fibers. The use of EDTA a strong calcium chelating agent complexes with the calcium in pectin aggregates and promotes separation of the fibers (Troedec *et al.* 2008). Thermal degradation studies of the treated fibers all showed that the treatments resulted in a change in the degradation temperature of the fibers after treatment. All treatments result in the removal of amorphous cellulose and leave a more ordered and temperature resistant molecule. $\text{Ca}(\text{OH})_2$ and EDTA resulted in a decrease in degradation temperatures indicating that the cellulose was more easily degraded by these two treatments. NaOH treatments easily remove the amorphous cellulose fraction and hence increased the degradation temperature to 410 °C (Troedec *et al.* 2008). XRD studies show that treatments with PEI, NaOH and EDTA all increase the crystallinity index. This is due to the fact that these treatments remove the amorphous cellulose from the polymer. PEI forms stable amine carbonate salts with the carbonyl groups from cellulose degrading the amorphous cellulose. NaOH treatments hydrolyses the amorphous cellulose fraction which results in an increased crystallinity index. $\text{Ca}(\text{OH})_2$ and CaCl_2 treatments do not increase the crystallinity index of the hemp fibers. With FTIR analysis the band at 1732 cm^{-1} , characteristic for hemicelluloses, has a low absorbance value for PEI and $\text{Ca}(\text{OH})_2$ and is absent for NaOH treatment. The absorption

band located at 1505 cm⁻¹ is present for all treatments. This peak is for lignin and it is evident that none of the treatments could successfully remove lignin (Troedec *et al.* 2008).

Zhao *et al.* 2010 from the Institute of Applied Chemistry, Department of engineering, Tsinghua University, Beijing China delignified sugarcane bagasse with alkali and peracetic acid and studied the changes brought on by the treatments. FTIR analysis showed increased intensities of the bands at 3400 cm⁻¹ and 2910 cm⁻¹ which were attributed to an increase in the cellulose content of the pulp as compared to the raw SCB (Zhao *et al.* 2010). Bands at 1430 cm⁻¹, 1375 cm⁻¹, 1155 cm⁻¹, 1108 cm⁻¹, 1030 cm⁻¹, and 895 cm⁻¹ had an increase in intensities. These bands are characteristic for cellulose absorption and become more intense after alkali and peracetic acid pretreatment. Bands corresponding to lignin at 1600 and 1510 cm⁻¹ were absent for alkali and Kraft pulp but a slight band at 1510 cm⁻¹ was present for alkali treated solids indicating residual lignin in the bagasse. A strong band at 1732 cm⁻¹ was present for raw SCB indicating a large hemicellulose fraction in the sample. Other treated samples did not display this band indicating deacetylation occurred during the alkali pretreatment. **L**ateral **O**rientation **I**ndices for alkali-treated solid, alkali-PAA pulp, and Kraft pulp were 2.39, 1.11, and 1.79 (Zhao *et al.* 2010), respectively as calculated using infrared ratios. The infrared crystallization index (A~1372/A~2900) for raw bagasse, alkali-treated solid, alkali-PAA pulp, and Kraft pulp were 0.97, 0.670, 1.45, and 0.91, respectively. Alkali-PAA pulp had the highest value, indicating that the pulp had the highest cellulose crystallinity (Zhao *et al.* 2010). XRD studies showed that the Crystallinity Index (CrI = $[(I_{002} - I_{am}) / I_{002}] \times 100$) was 53.3%, 58.5%, 67.9%, and 68.2% for raw bagasse, alkali-treated solid, alkali-PAA pulp, and Kraft pulp, respectively. The increase in CrI values is due to the removal of amorphous lignin and hemicellulose from the SCB. Therefore, according to the above analysis of alkali-PAA pulp and Kraft pulp by FTIR, XRD, TGA, and DTG, it can be concluded that the reason why alkali-PAA pulp had superior mechanical properties relative to Kraft pulp can be explained by the fact that alkali-PAA pulp

had a higher degree of polymerization and cellulose crystallinity, which increased the cellulose intercrossing and fiber strength during paper-sheet formation (Zhao *et al.* 2010).

Mandal and Chakrabarty 2011 from the Department of Polymer Science and Technology, Calcutta University, India isolated nanocellulose from waste sugarcane bagasse (SCB) by acid hydrolysis and centrifugation. They found that successive treatments of SCB with sodium chlorite bleach, sodium sulphite and sodium hydroxide was effective in removing lignin and hemicellulose from SCB. FTIR analysis showed that a peak at 1245 cm^{-1} representative of aryl groups in lignin was present only in the spectra of untreated bagasse. A broad peak at $3500 - 3200\text{ cm}^{-1}$ indicates the free O–H stretching vibration of the OH groups in cellulose molecules was observed for all treated and untreated SCB samples (Mandal and Chakrabarty 2011). They also found a peak at 902 cm^{-1} which continually increased with successive treatments and was attributed to β -glycosidic linkages between glucose units in cellulose. This increase in peak transmission indicated an increase in cellulose II content from SCB to nanocellulose (Mandal and Chakrabarty 2011). TGA and DTG showed that presence of amorphous and less thermally stable amorphous cellulose, lignin and hemicellulose caused the onset temperature for the degradation of the SCB to be lower than that of the treated and more crystalline cellulose. The removal of all the non-cellulosic materials helped to make the cellulose structure more dense and compact and hence the rise in the onset temperature of degradation (Mandal and Chakrabarty 2011). The percent crystallinity as calculated using XRD data increased in going from the sugarcane bagasse to cellulose and subsequently to nanocellulose (Mandal and Chakrabarty 2011). DLS studies showed the minim particle size to be 18.17nm which accounted for 0.8% volume and 11.5% volume of the CNCs was due to particles size peaking at 32.84 nm. The rest of the volume fraction has particle sizes greater than 37.84 nm and extend

up to about 220 nm accounting for only 0.7% volume fraction (Mandal and Chakrabarty 2011). SEM micrographs of the treated and untreated SCB showed that alkali and chlorite breaching successfully removed surface waxes and oils from the fibers and reduced the diameter of individual fibers. AFM micrographs showed that the acid hydrolysis could cleave the amorphous region of microfibrils longitudinally producing nanorods with a high aspect ratio. The AFM micrographs showed nanocrystals with dimensions of 70-90 nm (Mandal and Chakrabarty 2011). TEM analysis showed individual and agglomerated nanocrystals of 170 nm \times 35 nm, typical dimensions of the crystals.

Liu *et al.* 2011 from the College of Chemistry, Nanjing University of Information Sciences and Technology, Nanjing, China performed a study on the structure and rheology of nanocrystalline cellulose wherein they used sulphate hydrolysis and high-pressure homogenization to reduce the size of microcrystalline cellulose to the nanoscale. They obtained needle-shaped nanocrystals showing a relatively uniform size with length of 90 ± 50 nm and width of 10 ± 4 nm (Liu *et al.* 2011). Structure and morphology of the ordered liquid crystalline phase were characterized by scanning electron microscope and polarized optical microscope. The particle distribution studies showed that most of nanocrystals presented a relative uniform size with length of 60–120 nm, which would give an aspect ratio varying from 10 to 15 (Liu *et al.* 2011). They showed that a combination of chemical and mechanical treatment could effectively reduce the size of the cellulose crystals, which could then be dispersed to give an aqueous suspension. High Resolution Transmission Electron Microscope (HRTEM) studies confirmed the presence of cellulose I by the presence of interplanar spacing between adjacent lattice fringes of 0.389 nm, typical of cellulose I allomorph. A sharp strong peak at $2\theta = 22.7^\circ$, characteristic of cellulose I was also observed with WAXRD studies (Liu *et al.* 2011).

Abraham *et al.* 2011 from the Department of Chemistry, Bishop Moore College, Mavelkkara, Kerala, India performed the extraction of nanocellulose fibrils from lignocellulosic fibres using raw banana, jute and pineapple leaf fibre. Alkali treatment, steam explosion, bleaching and acid hydrolysis was used to reduce the fibres to Nano range. FTIR analysis revealed that alkali treatment reduces hemicellulose and lignin content by reacting with sodium hydroxide. This resulted in the increase of the –OH concentration, evident from the increased intensity of the peak between 3300 and 3500 cm^{-1} bands compared to the untreated fibre (Abraham *et al.* 2011). From the FTIR analysis they concluded that there was a reduction in the number of binding components present in the fibres due to the process of steam and chemical treatment. The raw fibres had a characteristic peak in between 1730–1740 cm^{-1} and 1200–1300 cm^{-1} (Abraham *et al.* 2011) . These peaks were chiefly responsible for the hemicellulose and lignin components. These characteristic peaks were completely absent in the final bleached cellulose fibre. XRD analysis of the alkali treated fibres also revealed an increase in the crystallinity index of the banana, PALF and jute. Alkali treatment led to the removal of non-crystalline binding materials like lignin, hemicellulose and pectin which resulted in the increase of the percentage crystallinity of the fibres (Abraham *et al.* 2011). The removal of amorphous fractions of the lignocellulosic biomass resulted in the decrease of the diameter of the individual fibres. An increase in alkali concentration used for the treatment of cellulose fibres resulted in an increased crystallinity of the fibres, however when the acid concentration was increased to 50% a decrease in the concentration of the pure cellulose was found showing that at high alkali concentrations resulted in the pure cellulose being degraded (Abraham *et al.* 2011). The trend is the same in all fibres which were studied. Crystallinity indices increased for all fibre samples with chemical treatments indicating a removal of the cementing materials binding the fibres (Abraham *et al.* 2011). SEM micrographs showed clear depolymerisation by steam explosion wherein removal of the surface impurities along with defibrillation was

achieved. It was shown that during the chemical treatment (alkalization) most of the lignin and hemicellulose were removed. Mechanical treatment (steam explosion) further removed the amorphous materials (lignin, hemicellulose, etc.) from the inner part of the fibre via depolymerisation and defibrillation (Abraham *et al.* 2011). Acid hydrolysis further reduced fibre diameter to less than 100 nm. TGA and DTG curves of the untreated fibres of banana, PALF and jute shows multiple stages, indicating the presence of different components that decompose at different temperatures. The extracted nanocellulose showed a higher degree of thermal stability with an onset temperature of 346 °C compared to 317 °C of the raw banana fibres. The nanocellulose obtained from extracting natural fibres had higher thermal stability. In addition, it showed higher amounts of residual solids. This could be an indicator of the presence of small amounts of hemicellulose or lignin which withstood the extracting procedures (Abraham *et al.* 2011).

Teixeira *et al.* 2011 from the National Nanotechnology Laboratory of Agriculture (LNNA), Embrapa Agricultural Instrumentation, Brazil extracted and characterized nanocellulose whiskers from sugarcane bagasse. SCB fibres were extracted after alkaline peroxide pre-treatment followed by acid hydrolysis. The results showed that SCB could be used as a source to obtain cellulose whiskers and they had needle-like structures with an average length (L) of 255 ± 55 nm and diameter (D) of 4 ± 2 nm, giving an aspect ratio (L/D) around 64 (Teixeira *et al.* 2011). The samples were named SC and SCBW 75 due to the time used for acid hydrolysis. The produced whiskers were in the form of a stable suspension but the sample hydrolysed for 75min had a brown discolouration due to a certain level of cellulose degradation (Teixeira *et al.* 2011). The whiskers obtained had a length (L) of around 255 ± 55 nm and the diameters (D) of 4 ± 2 and 8 ± 3 nm for SCBW 30 and SCBW 75, respectively (Teixeira *et al.* 2011). The

sample SCBW75 presented a decrease in crystallinity and a little change in the diffractograms profile, with the disappearance of the peak at $2\theta = 15.3^\circ$.

Pereira *et al.* 2011 from the Department of Materials and Technology, Brazil investigated sugarcane bagasse pulping and bleaching. A three stage isolation process was utilized to obtain cellulose fibres. Crude, untreated SCB was treated with a 10% (w/v) H_2SO_4 solution then bleached in sodium chlorite to remove residual lignin. FTIR analysis revealed that bands at 1512 cm^{-1} and 1250 cm^{-1} were not present for bleached cellulose fibres which indicated a reduction in the lignin content of the cellulose fibres (Pereira *et al.* 2011). The removal of lignin was confirmed by X-ray diffraction where a major diffraction peak for 2θ ranging between 22° and 23° was present, which corresponds to cellulose (002) crystallographic planes. The spectrum corresponding to the unmodified sugarcane bagasse showed diffraction peaks at 2θ angles 15.9° and 22.4° . For crude cellulose fibres the same peaks could be observed at 15.9° and 23.2° but were of decreased intensity. Bleached cellulose fibres showed the same peaks observed at 16.2° and 22.9° but were of increased intensity (Pereira *et al.* 2011). The TGA and DGT profiles of the fibres presented degradation peaks between $260 - 340^\circ\text{C}$ from untreated to bleached cellulose fibres. The increase in degradation temperature for the treated fibres was attributed to the bleaching treatments. SEM micrographs showed that treatments were successful in the removal of wax, pectin, lignin, and hemicelluloses. Bleaching of the fibres reduced fibre length and fibre diameter. It was observed that the bleached cellulose fibres demonstrated higher thermal stability, crystallinity content increase, and flattened morphology when compared to crude cellulose fibres (Pereira *et al.* 2011).

Chen et al. 2012 from the MMRI/CAPPA-D Department of Chemical Engineering at the McMaster University in Hamilton, Ontario, Canada produced cellulose nanocrystals from potato peel waste and applied them as reinforcing additives to bio-composites. They used alkali treatment and subsequent acid hydrolysis to separate the nanocrystals from the biomass. TEM images showed nanocrystals of average length 410 ± 181 nm with an aspect ratio of 41 (Chen *et al.* 2012). FTIR analysis of the potato peel revealed bands characteristic to most lignocellulosic biomass. The region of $800\text{--}1500$ cm^{-1} is a unique fingerprint region for cellulose. Three vibrational bands were unique to only the untreated potato peel at 1739 cm^{-1} , 1514 cm^{-1} and 1456 cm^{-1} , with the former band attributed to the C=O stretching vibration of acetyl and uronic ester groups of hemicellulose as well as the ester linkage of the carboxyl group in lignin (Chen *et al.* 2012). Most of the cellulose peaks remained unaffected after alkali and acid treatment suggesting that the structure of cellulose remained unaffected throughout both treatments. XRD was utilized to calculate the crystallinity using the Segal equation. For potato peel derived CNC the crystallinity index was 85 % (Chen *et al.* 2012), with the diffractograms having strong peaks at $2\theta = 14.7^\circ$, 16.4° , and 22.6° , which were assigned to the cellulose I crystalline structure.

Kopania, Wietecha and Ciechańska 2012 from the Instytut Biopolimerów i Chemii Włókna in Łódź, Poland performed studies on isolation of cellulose fibres from waste plant biomass. Herein rape, hemp and flax straws were used to isolate cellulose nanocrystals. Cellulose was obtained from the selected materials by the removal of lignin, hemicellulose and pectin by thermal, chemical and mechanical means. The initial lignocellulosic material were steamed, subjected to hot water treatment before undergoing a series of chemical treatments. Sodium hydroxide/hydrogen peroxide digestion which involved cooking the samples in a liquor at

about 60 °C containing: 5% NaOH, 5.5% H₂O₂, 0.3% EDTA, 0.5% MgSO₄ and 5% liquid glass, per sample bone dry weight (Kopania, Wietecha and Ciechańska 2012). Sodium chlorite delignification included a 14 g/dm³ NaClO₂ and 3 g/dm³ H₂SO₄ was added, and the pulp was placed in a laboratory thermostat at a temperature of 70 °C for 120 min (Kopania, Wietecha and Ciechańska 2012). The peracetic acid delignification step used a 2% CH₃COOH based on active oxygen and 0.5% MgSO₄ was added and placed in a laboratory thermostat at a temperature of 80 °C for 120 min. Their study showed that the delignification of the selected biomass was feasible and hemp straw had the highest alpha-cellulose content of 60.09% and 51.56% for retted flax straw (Kopania, Wietecha and Ciechańska 2012).

Fazli *et al.* 2012 attended the 2012 2nd International Conference on Environment Science and Biotechnology in Singapore where they presented their work titled Nano Crystalline Cellulose Production and Its Application in Novel Food Packaging. Cotton linter was used as a substrate for the production of cellulose nanocrystals using chemical methods. Alkali treatment with subsequent acid hydrolysis using a solution of 65% w/w for 3 hours (Fazli *et al.* 2012) was used to isolate the nanocrystals. After ultrasonication for 15 minutes at the cellulose nanocrystals suspension was ready.

Sheltami *et al.* 2012 from the Polymer Research Centre (PORCE), School of Chemical Sciences and Technonology, University Kebengsaan, Malaysia extracted cellulose nanocrystals from mengkuang leaves (*Pandanus tectorius*). After pre-treatment of the leaves with water they were dried and chopped into smaller pieces. They were then ground in a mill and treated with 4% NaOH at 1255 °C for 2 h, after which bleaching treatment was carried out

using 1.7 w/v% NaClO₂ at pH 4.5 and 125 °C for 4 h. Each step was repeated several times, and the leaves were washed with distilled water after each treatment (Sheltami *et al.* 2012). Cellulose nanocrystals were prepared by acid hydrolysis from the cellulose obtained as described above using 60 % wt. H₂SO₄ solution at 45 °C. The time of hydrolysis in this study was fixed at 45 min, which was found to be the optimum time. The ratio of the obtained cellulose to liquor was 5:100 (% wt.). The hydrolysed cellulose sample was washed five times with deionized water and centrifuged. The suspension was then dialyzed against distilled water using a membrane until a constant pH was reached.. The colour of the leaves changed from green to light brown after alkali treatment and became white after bleaching (Sheltami *et al.* 2012). FESEM micrographs of the untreated ground leaves and the micrographs of the products at different stages of extraction showed diameters of the fibres in the raw leaves ranged from 100 µm to 300 µm. SEM micrographs showed that fibres in the original leaves were bonded together by cement components, which were partially diminished after the alkali treatment (Sheltami *et al.* 2012). The alkali treatment removed the extractives from the leaves as indicated by the surface morphology changes. After bleaching the fibre bundles were dispersed into individual fibres with diameters in the range 5–80 µm. FTIR spectra obtained for mengkuang leaves at different stages of treatment showed a band located at 1734 cm⁻¹. This band was no longer present in the FTIR spectra of leaves after alkali and subsequent bleach treatments. The disappearance of this band could have been caused by the removal of hemicellulose and lignin from mengkuang leave fibres during the chemical extraction (Sheltami *et al.* 2012). Hemicellulose and lignin were not completely removed after the alkali treatment, and that hemicellulose remained after the bleaching treatment. For this reason, the disappearance of the C-O stretching band from the spectrum could be caused by cleavage of all ester linked substances of the hemicellulose by alkali treatment. The bands at 1508 and 1247 cm⁻¹ disappeared after the bleaching treatment, which suggests the removal of lignin (Sheltami

et al. 2012). From XRD measurements the crystallinity indices of raw leaves, alkali-treated leaves, and bleached leaves were found to be 55.1%, 60.2%, and 69.5%, respectively. These results clearly demonstrate that the crystallinity of the material progressively increases during the chemical extraction. This was ascribed to the progressive removal of amorphous hemicellulose and lignin (Sheltami *et al.* 2012). DTG measurements showed a shoulder in the DTG curve at around 300 °C, but was no longer present after the alkali treatment, which likely reflects the removal of a portion of the hemicellulose (Sheltami *et al.* 2012). The curve obtained for raw leaves shows an earlier weight loss starting at around 200 °C. These findings likely reflect the decomposition temperature of hemicelluloses and lignin. The degradation onset temperature after alkali and bleaching treatments began around 250 °C, which was significantly higher than that of raw leaves. This lower degradation onset temperature for the untreated leaves was caused by the hemicellulose component, which remained after the chemical treatments (Sheltami *et al.* 2012). Mengkuang cellulose nanocrystals ranged in length from 50 to 400 nm, with an average value around 200 nm. The diameter was in the range 5 – 25 nm. These results demonstrated the efficiency of the conditions used for the acid hydrolysis treatment of mengkuang fibres and confirmed that the aqueous suspension contained individual nanocrystals.

Lu and Hsieh 2012 from the Fibre and Polymer Science Department, University of California, Davis, USA prepared and characterized cellulose nanocrystals from rice straw. Rice straw was thoroughly washed 3–4 times with warm tap water to remove dirt and aqueous soluble substances, followed by prolonged (about one week) air drying. Rice straw powder (30 g) was first extracted with 2:1, v/v toluene/ethanol(450 mL) mixture for 20 h to remove wax, pigments and oils, followed by oven-drying at 55 °C for 24 h. The dewaxed powder was then immersed in 1.4% acidified NaClO₂ (1000 mL), with pH adjusted to 3.0–4.0 by CH₃COOH, at 70 °C for 5 h to dissolve lignin (Lu and Hsieh 2012b). Hemicellulose and silica in the delignified powder

were leached with 600 mL 5% KOH at room temperature for 24 h and then at 90 °C. The white cellulose powder was centrifuged and washed with excess deionized water until the filtrate reached a neutral pH. The cellulose isolated from rice straw was hydrolysed using 64–65 % wt. sulphuric acid at an 8.75 mL/g acid-to-cellulose ratio at a temperature of 45°C for 30 or 45 min. Acid hydrolysis was stopped by diluting with 10-fold ice water. The resulting cellulose nanocrystal gel was washed once, centrifuged and then dialyzed with regenerated cellulose dialysis membranes against ultra-pure water until reaching neutral pH (Lu and Hsieh 2012b). The CNC-30 ranged from 10 to 65 nm in width and 50 to 700 nm in length, averaged 30.7 nm in width and 270 nm in length. In contrast, CNC-45 had a much smaller mean width of 11.2 nm and mean length of 117 nm. The aspect (length to width) ratios of CNC-30 and CNC-45 were calculated to be 8.8 and 10.5, respectively. The aspect ratios of CNC-30 and CNC-45 are not as much different from each other as their actual dimensions (Lu and Hsieh 2012b). The crystallinity index (CrI) calculated from XRD diffractograms for cellulose fibres was 61.8% whereas those for the self-assembled CNCs were significantly higher at 86.0% and 91.2% for CNC-30 and CNC-45, respectively. The significantly higher crystallinity of the self-assembled CNC-30 and CNC45 than the original cellulose fibres is attributed mainly to the removal of amorphous cellulose (Lu and Hsieh 2012b).

Lu and Hsieh 2012 from the Fibre and Polymer Science Department, University of California, Davis, USA isolated cellulose and core–shell nanostructures of cellulose nanocrystals from chardonnay grape skins. The as-received grape skins was milled to pass through a 60-mesh screen, followed by oven-drying at 70 °C for 2 days. The dry grape skin powders were first extracted with a 2:1 v/v toluene/ethanol mixture for 20 h to remove wax, phenolics, pigments and oils, followed by oven-drying at 70 for 24 h. The extracted powders were then heated in

2% H₂SO₄ aqueous solution under constant stirring at 90 °C for 5 h to hydrolyse acid soluble polysaccharides and polyphenolics, filtered and washed with water until neutral pH was obtained. The acid treated powders were further leached with 5% NaOH at the ambient temperature for 24 h and then at 90 °C for 5 h to dissolve hemicellulose and other base soluble polysaccharides, filtered and thoroughly washed to neutral pH (Lu and Hsieh 2012a). The base treated sample was bleached by 5% H₂O₂ with pH adjusted to 11.5 by NaOH at 45 °C for 8 h (more H₂O₂ as well as higher temperature, e.g., 70 °C. Cellulose isolated from grape skins was hydrolysed using 64–65 %wt. sulphuric acid at an 8.75 mL/g acid-to-cellulose ratio and at a temperature of 45°C for 30 min. Acid hydrolysis was stopped by diluting with 10-fold ice water. The resulting cellulose gel was washed once, centrifuged for 25 °C for 10 min and then dialyzed using regenerated cellulose dialysis membranes against ultra-pure water until reaching a neutral pH (Lu and Hsieh 2012a). The most distinct FTIR spectral change in the white product is the absence of two peaks at 1741 and 1530 cm⁻¹. The crystallinity index (CrI) was calculated using x-ray diffractograms to be 54.9% using the empirical Segal equation. The XRD crystalline structural data, together with FTIR chemical structural compositions and DSC and TGA thermal behaviours, confirmed the isolated white product to be pure cellulose. These structural analyses demonstrated the step-wise process of organic/acid/base/oxidation to be highly effective in isolating cellulose from grape skins (Lu and Hsieh 2012a).

Yu *et al.* 2012 from the State Key Laboratory of Pulp and Paper Engineering, South China University of Technology, Guangzhou, China prepared and characterized bamboo nanocrystalline Cellulose. Bamboo pulp was treated with 4 % wt. NaOH at 50 °C for 2 hours to remove the fatty acids, the residual lignin, and some other impurities. The amorphous cellulose can be swelled up sufficiently so that the sulphuric acid can subsequently easily

penetrate into the fibre interior during the process of hydrolysis. A 46% wt. sulphuric acid solution was used with continuous stirring to hydrolyse the bamboo pulp. After several minutes, when the colour of the suspension became dark yellow, the cellulose suspension was diluted with deionized (DI) H₂O to stop the hydrolysis reaction and allowed to settle for several hours until the suspensions were layered, and the clear top layer was decanted off. The washing with DI H₂O was repeated until there was only one phase and the suspension was not layered. The suspensions were then washed with deionized water using repeated centrifuge cycles of 10 min at 5,000 rpm. The supernatant liquor was removed from the sediment and replaced with new deionized water and mixed. The centrifuge step was stopped when the supernatant became turbid. The final wash was done using dialysis with DI H₂O for several days until the water pH remained constant. Afterwards, the ultrasonication was conducted for 20 min resulting in a stabilized aqueous CNC suspension. The nanocrystalline cellulose suspension samples were subjected to freeze-drying (Yu *et al.* 2012). . TEM images of NCC revealed that the rod-like structure of the crystallite had a length ranging from 200 nm to 500 nm, and the crystals had diameters less than 20 nm (Yu *et al.* 2012). The FTIR spectrum of CNC showed broadening of the OH absorption band shifted from 3342 cm⁻¹ to 3409 cm⁻¹ was due to the sulphuric acid hydrolysis, but also because of water adsorption. The broadening of the absorption band at 3342 cm⁻¹ was also attributed to the presence of the amorphous fraction of the cellulose (Yu *et al.* 2012). The XRD results suggested that the crystalline structure of bamboo nanocrystalline cellulose is like that of cotton nanocrystalline cellulose, and the diffractograms are both characteristic of cellulose-I (Yu *et al.* 2012). The crystallinity was 71.98%, the crystallinity of bamboo nanocrystalline cellulose was higher than that of flax and rutabaga nanofibrils to be 59% and 64% respectively (Yu *et al.* 2012).

Rosli, Ahmad and Abdula 2013 from the Polymer Research Centre (PORCE), School of Chemical Sciences and Food Technology, Universiti Kebangsaan Malaysia, Malaysia studied the isolation and characterization of cellulose nanocrystals from *Agave angustifolia* fibre using alkali and bleaching treatments followed by acid hydrolysis. The dried leaves were retted, separation of the fibre from the stem, and long fibres cut into shorter 3 – 5 cm strips. The fibres were then treated with 4% NaOH at 70 to 80 °C for 2 hours and then bleached with 1.7 w/v% NaClO₂ at 70 to 80 °C for 4 hours. Each fibre treatment was done twice, and the fibres were washed with distilled water after each treatment. The hydrolysis was carried out using a 60 %wt. H₂SO₄ solution at 45 °C for 45 min. The resulting suspension was neutralized, centrifuged, washed and dialyzed against deionized water. FESEM studies showed a ‘composite’-like structure in which the fibre bundles are held together by non-cellulosic substances (Rosli, Ahmad and Abdula 2013). FESEM studies showed that chemical treatments altered the surface of the fibres and drastically reduced the diameters of the fibres. TEM micrographs showed the CNCs' needle-like structure consisted mostly of individual fibrils and some aggregates (Rosli, Ahmad and Abdula 2013). The CNCs ranged from 8 to 15 nm in diameter and 170 to 500 nm in length, with an average of 10 nm in diameter and 310 nm in length. The calculated aspect ratios of the CNCs were in the range of 10 to 45 with 70% in the range of long CNC; this indicates great potential for them to be used as a reinforcing agent in nanocomposites (Rosli, Ahmad and Abdula 2013). FTIR analysis showed cellulose and CNCs showed similar peaks with the only difference concerning a slight intensity change in the peaks. All of the spectra exhibited a broad band in the region of 3400 to 3300 cm⁻¹, which indicates the free O-H stretching vibration of the OH group in cellulose molecules (Rosli, Ahmad and Abdula 2013). XRD analysis showed a difference concerning slight intensity changes in the peaks, representing some changes in the fibres crystallinity. For fibres with high cellulose content, the raw Agave fibres, only one broad peak was observed due to the presence

of amorphous material which covered the two peaks (Rosli, Ahmad and Abdula 2013). The crystallinity index for the raw, alkali-treated, bleached, and acid-hydrolysed fibres was found to be 59%, 69%, 74%, and 82%, respectively and the increase in the degree of crystallinity was noted after the chemical treatments. TGA and DTG results showed that the degradation temperature increased by chemical treatment, which could be attributed to the removal of hemicelluloses and lignin, as well as a higher degree of crystallinity in the treated fibre samples. The higher crystallinity led to a higher heat resistance, and improved the thermal degradation (Rosli, Ahmad and Abdula 2013).

Maiti *et al.* 2013 from the Department of Chemistry, Nanjung University of Information Sciences and Technology, China prepared and characterized nanocellulose with a new shape from three different precursors. China cotton, South African cotton and waste tissue papers were used to produce nanocellulose by acid hydrolysis route. No chemical pre-treatment were done for the production of nanocellulose from these precursors (Maiti *et al.* 2013). All were subjected to a 47% sulphuric acid solution which was vigorously stirred at 60 °C for 2 hours. The resulted suspension was centrifuged and washed with deionized water several times to reduce acid concentration. The suspension was finally neutralized with 0.5 N NaOH solutions and again washed with distilled water. The prepared nanocellulose suspension was freeze-dried to get nanocellulose powder (Maiti *et al.* 2013). The approximate ranges of diameter of CNC, cotton nanocellulose, and TNC, tissue nanocellulose were from 30 to 60 nm and 10 and 90 nm respectively. However, TEM image of SANC, South African cotton nanocellulose, showed smaller and finer particles of completely different shape from other samples (Maiti *et al.* 2013). The diameter range of SANC, South African Cotton nanocellulose, aggregates was from 2 and 10 nm, was smaller than those from CNC and TNC, ranging from 30 to 60 nm and 10 to 90

nm, respectively (Maiti *et al.* 2013). DLS measurements showed the particle size was larger for CNC and TNC in comparison to that observed in particle size analysis study due to the high agglomeration affinity of CNC and TNC. Two samples showed an increase in % crystallinity when converted to CNC. China Cotton showed a 10% increase from 82.4 -92.4 %, South African cotton 7.6 % from 90.2 – 97.8 % .Only Waste Tissue paper experienced a decrease in % crystallinity from 90.7 – 89.9%. Waste tissue paper is generally made from paper pulp. This paper pulp was used to undertake several chemical processes to remove the amorphous portion. Due to removal of this amorphous portion of that paper pulp by means of different chemical processes high crystallinity was observed in case of waste tissue paper. But when waste tissue paper was subjected to acid hydrolysis for the generation of TNC, the highly ordered crystalline structure was affected and that resulted in a little lower crystallinity (Maiti *et al.* 2013). The nanocellulose (CNC, SANC, and TNC) exhibited distinct endothermic changes within the range of temperature when studied. TGA and DTG revealed that major degradation temperature shifted to higher range of temperature in case of nanocellulose than corresponding precursor. The higher thermal stability of the nanocellulose can be ascribed to their higher flexibility, hence higher possibility of entanglements of the nanofibrils (Maiti *et al.* 2013). The major degradation peak temperatures were observed at 360 °C, 358 °C and 367 °C for CNC, SANC and TNC respectively which appeared as higher than the values of their respective raw materials i.e. 338 °C, 290 °C and 353 °C respectively (Maiti *et al.* 2013).

Santos *et al.* 2013 from the Instituto de Quimica, Universidade Federal de Uberlândia, Campus Santa Monica, Minas Gerais, Brazil isolated cellulose nanocrystals from pineapple leaf. Dried pineapple leaves were milled and treated with a 2% (w/w) for 4 h at 100 °C under mechanical stirring. After sufficient rinsing, the solids were dried and bleached with a 1.7 %wt. NaClO₂

and buffered with 2.7 %wt. glacial acetic acid. The bleach treatment was performed at 80 °C for 4 h. Acid hydrolysis was performed at 45 °C for 5 min, 30 min or 60 min under vigorous and constant stirring. The resulting suspension was diluted 10 fold with deionized water and centrifuged to remove the supernatant liquid. The precipitate was then washed and dialyzed using a cellulose membrane. The cellulose nanocrystals from pineapple leaf were labelled CNPL5 or CNPL30 or CNPL60, depending on the time of extraction. From FTIR studies it could be noted that the lack of peaks at 1742 cm^{-1} , 1514 cm^{-1} and 1254 cm^{-1} in the spectrum of TPL (treated pineapple leaves) is due to the significant removal of hemicelluloses, and mainly lignin, by the purification process (alkali and bleaching treatments). A peak at 1061 cm^{-1} is assigned to the C-O stretching and the C-H rock vibrations of the cellulose. The small increase in this peak for treated pineapple leaf, TPL, in relation to pineapple leaf, PL indicates that the TPL have higher cellulose content. Similar behaviour was observed when comparing the spectra of TPL with CNPL5, CNPL30 and CNPL60. This peak appeared in all of the spectra and the differences presented suggest that the CNPL5, CNPL30 and CNPL60 samples has a very high content of cellulose (Santos *et al.* 2013). The CrI was found to be about 49, 64, 69, 73 and 68% for the PL, TPL, CNPL5, CNPL30 and CNPL60, respectively. The higher CrI value of TPL compared to PL can be well understood by the reduction and removal of amorphous non-cellulosic compounds induced by the alkali and bleaching treatments performed in the purification process (Santos *et al.* 2013). AFM images of sample CNPL5 showed micro-sized fibres and some needle-like nanoparticles. Therefore, it is clear that the hydrolysis conditions employed for this sample (CNPL5) were not sufficient to completely isolate CNCs from TPL fibres (Santos *et al.* 2013). DLS measurements showed highest percentage of CNPL30 particles having a length of 210 -240nm and diameter of 2 -5 nm. CNPL60 particles had length mostly in the 150 – 210 nm and diameter range of 3 – 5 nm.

Silvério *et al.* 2013 from the Instituto de Química, Universidade Federal de Uberlândia, Campus Santa Monica, Minas Gerais, Brazil extracted and characterized cellulose nanocrystals from corncob, CC, for application as reinforcing agent in nanocomposites. Dried corn cob was milled and screened to pass through a 35-mesh screen. The milled CC was treated with 2% NaOH (w/w) for 4 h at 100 °C. After which it was bleached with a solution made up of equal parts (v:v) of acetate buffer (27 g NaOH and 75 mL glacial acetic acid, diluted to 1 L of distilled water) and aqueous chlorite (1.7 % wt. NaClO₂ in water). This bleaching treatment was performed at 80 °C for 6 h (Silvério *et al.* 2013). The treated corn cob (TCC) was subjected to sulphuric acid hydrolysis at 45 °C for 30 min or 60 min or 90 min under vigorous and constant stirring. After the hydrolysis the solution was quenched with 10 fold deionized water to stop the hydrolysis reaction and centrifuged to remove excess acid. The precipitate, the CNCs, was then washed, ultra-sonicated and dialyzed. The CNCs were labelled CNC30, CNC60 and CNC90 as based on the hydrolysis time. FTIR analysis of corn cob (CC) showed a band at 1736 cm⁻¹ corresponding to lignin and hemicellulose. This band disappeared and was not visible in the spectra of TCC and CNC30. This can also be explained by the elimination of hemicelluloses and mainly the lignin by chemical treatment (Silvério *et al.* 2013). XRD studied performed found the CrI to be about 61.0, 73.3, 79.8, 83.7 and 78.0% for the CC, TCC, CNC30, CNC60 and CNC90, respectively (Silvério *et al.* 2013). The higher CrI value of TCC compared to CC can be well understood by the reduction and removal of amorphous non-cellulosic compounds induced by the alkali and bleaching treatments performed in the purification process (Silvério *et al.* 2013). The sample CNC90 presented a decrease in crystallinity with respect to CNC60, suggesting that the extraction time of 90 min was severe enough to remove not only the amorphous phase, but also to destroy part of the cellulose crystalline regions (Silvério *et al.* 2013). AFM images of CNC30, CNC60 and CNC90. AFM micrographs presented needle-like nanoparticles, confirming that the extraction of CN from corncob was

successful. CNC30 had particles of length 287.3 ± 75.5 nm. The length of these particles were within the range 163.1 – 509.5 nm. The diameter of these particles was 4.90 ± 1.34 nm. The diameter was within the range 2.58 – 9.58 nm. The aspect ratio of the particles was 63.0 ± 24.4 with range 24.1 – 151.1. CNC60 had particles of length 210.8 ± 44.2 nm. The length of these particles fell in the range 116.1 – 334.8 nm. The diameter of these particles was 4.15 ± 1.08 nm. The diameter was within the range 2.46– 7.31 nm. The aspect ratio of the particles was 53.0 ± 15.8 with range 23.8 – 116.2. CNC90 had particles of length 195.9 ± 45.9 nm. The length of these particles fell in the range 103.9 – 330.2 nm. The diameter of these particles was 4.03 ± 1.07 nm. The diameter was within the range 1.66 – 7.03 nm. The aspect ratio of the particles was $52.4.0 \pm 19.7$ with range 21.3 – 122.1 (Silvério *et al.* 2013).

Kumar *et al.* 2013 from the Department of Polymer and Process Engineering, Inida Institute of Technology, Roorkee, India characterized cellulose nanoparticles prepared from agro waste sugarcane bagasse. SCB was dried and ground to a 30 screen mesh. The SCB was dewaxed in a soxhlet extractor for 6 hours with 2:1 of benzene: methanol mixture as solvent. Delignification using an acidified sodium chlorite solution at 75 °C for one hour. This was repeated 4 – 5 times till the products became white. The resulting solids were then treated with 2% KOH for 2 hours at 90 °C, then again with 4 % KOH for 2 hours at 90 °C. The solids were then filtered and rinsed till neutral. This was then referred to as chemically purified cellulose (CPC). The CPC was then used to extract CNCs by acid hydrolysis, with H₂SO₄ solution (64% (w/w), 1:10 g/ml (cellulose: dilute H₂SO₄)) at 45°C for 60 min under vigorous and constant mechanical stirring (Kumar *et al.* 2013). The hydrolysis reaction was quenched by adding excess (10 fold) chilled distilled water followed by successive centrifugation at 10,000-12,000 rpm for 15 min to remove the acidic solution. The sediment was collected, re-suspended in

distilled water and dialyzed using distilled water until the filtrate was neutral (pH 6-7). After this dialysis process, the sample was again centrifuged followed by sonication for 10 min in an ice bath to avoid overheating (Kumar *et al.* 2013). FE-SEM micrographs showed the SCB as having a high percentage of surface extractives (waxes, pectin and oil) (Kumar *et al.* 2013). Chemical treatments removed the surface extractives and reduced the fibre diameter by greatly removing the amorphous regions of semi-crystalline cellulose. TEM and AFM micrographs of very dilute suspensions of CNCs showed agglomerated “rod-like” nanocrystals. Most of these crystals had a size in the range 250 – 480 nm in length and 20 – 60 nm in diameter. Energy dispersive x-ray diffraction (EDX) attached with FE-SEM was used for elemental analysis of CNCs. The CNCs obtained contained 0.72 wt. elemental impurity. The bands at 1620 – 1649, 1512 and 1595 cm^{-1} are associated with the aromatic rings present in lignin, which are associated with the SCB before the chemical treatments. After chemical treatment with acidified sodium chlorite and alkali treatment, these bands are not observed in the FTIR spectrum of chemically purified cellulose, CPC. The band at 1512 cm^{-1} is absent and the band at 1250 cm^{-1} is reduced drastically in the FTIR spectrum of CPC indicating that the binding components of the biomass were removed by the chemical treatment (Kumar *et al.* 2013).

Normand, Mariana and Eke 2014 from the Division of Wood Chemistry and Pulp Technology, School of Chemical Science and Engineering, KTH Royal Institute of Technology, Teknikringen, Stockholm, Sweden isolated and characterized cellulose nanocrystals prepared from spruce bark. After extraction with acetone, the ground fibres were bleached using a 1% sodium chlorite, acetate buffer pH 4.8 and water in the proportions 1:1:1 (Normand, Moriana and Ek 2014). The pre-treated bark fibres were subjected to a 60% sulphuric acid hydrolysis for 60 minutes at 50 °C. The resulting suspension underwent successive centrifugation and dialysis. SEM images showed that pre-treatment was essential in swelling up the fibres so as to allow the bleaching agents access to the cementing matrix. The bleaching agents were

responsible for breaking down and partially removing the fibres from the matrix. AFM images showed rod like crystalline structure with high aspect ratios. These nanocrystals had a tendency to agglomerate due to their high specific area and the strong hydrogen bonds established between crystallites (Normand, Moriana and Ek 2014). Particle size determinations showed that the crystals had a length ranging from 60 to 340 nm and a diameter between 1.5 and 4.5 nm (Normand, Moriana and Ek 2014). FTIR was used to assess the efficacy of the chemical treatments on the fibres. A significant reduction in intensity of the main bands associated with lignin and non-cellulosic polysaccharides, at 1515 and 1735 cm^{-1} , was noticed during the isolation of the CNCs. The band at 1515 cm^{-1} , assigned to the aromatic C=C vibration in lignin, disappeared after the residue was bleached (Normand, Moriana and Ek 2014). WAXS revealed that the peak intensity corresponding to the 0 0 2 lattice planes increased and became sharper as a result of the chemical treatment, which was related to an increase in crystallinity of the material (Normand, Moriana and Ek 2014). The crystallinity index increased from bark fibres to cellulose nanocrystals. Thermogravimetric analysis confirmed that the partial removal of hemicelluloses in the residue and bleached fibres could be observed by the diminution of the shoulder at 275°C on the DTG curve. The bleached fibres degraded within a narrower temperature range and showed better thermal stability than the bark itself. This improvement in thermal stability could be due to an increase in crystallinity (Normand, Moriana and Ek 2014).

Li *et al.* 2014 from the College of Engineering, National Energy R&D Centre for Nano-food Biomass, China Agricultural University, Beijing, China prepared and characterized cellulose nanofibers from de-pectinated sugar beet pulp, SBP. They prepared cellulose nanofibers with diameter of 10–70 nm using alkali treatment and bleaching chemical treatments and high

pressure homogenization. Chemical treatments yielded significant changes on the chemical composition of the sugar beet pulp. FTIR analysis results indicate that the hemicellulose and lignin contents were removed from the untreated SBP during chemical treatments (Li *et al.* 2014). X-Ray diffraction studies showed an increase in crystallinity from sugar beet pulp to cellulose nanocrystals. Thermogravimetric data presented showed that the thermal degradation temperature of bleached fibres was higher than that of the alkali treated fibres. This indicates that the further removal of non-cellulosic impurities by the bleaching process is conducive in improving the thermal stability of DSBP cellulose fibres (Li *et al.* 2014).

Haafiz *et al.* 2014 from the Department of Polymer Engineering, Faculty of Chemical Engineering, Universiti Teknologi Malaysia, Skudai, Johor, Malaysia isolated and characterized cellulose nanowhiskers from oil palm biomass. Biomass fibres were swelled using N,N-dimethylacetamide and lithium chloride. The slightly swelled particles were then sonicated for 3 h over a period of 5 days, with long intervals between each sonication treatment to separate the cellulose nanowhiskers. The resultant cellulose nanowhiskers were repeatedly washed with distilled water then freeze-dried. FTIR results revealed that the band at 1163–1167 cm^{-1} corresponds to C-C and the C-O-C glycosidic ether band was at 1105 cm^{-1} , the latter peak is gradually lost in CNW due to hydrolysis treatment and concomitant reduction in molecular weight (Haafiz *et al.* 2014). SEM studies showed that swelling of the fibres altered their morphology. Aggregation of fibres was broken down after chemical swelling and acid hydrolysis. The tendency of fibre separation can clearly be observed after both treatments gave rise to intermittent fibrillary structure and further reduction in intra fibrillar diameter (Haafiz *et al.* 2014). From TEM analysis, it was observed that MCC was agglomerated to form large MCC particles. However, by treatment, individual whiskers (crystals) were obtained showing

a rod-like structure. The average size distribution of the whiskers from both treatments were analysed and found to be in the nanometre range (Haafiz *et al.* 2014).

Reddy and Rhim 2014 from the Department of Food Engineering and Bionanocomposite Research Institute, Mokpo National University in Muangun, Republic of Korea did work on the isolation and characterized cellulose nanocrystals from garlic skin. The skin was dried and ground into a fine powder and subjected to alkaline treatment before undergoing a 45 % sulphuric acid reflux at 60 °C for 2 hours. The resulting suspension was repeatedly centrifuged and then dialyzed before being freeze-dried. Chemical analysis results revealed that the crude fibre of garlic skin contained 41.77 % of cellulose, 20.87 % of hemicelluloses, 34.57 % of lignin, and 3.07 % of extractives. Cellulose was the predominant polysaccharide in the garlic skin fibre (Reddy and Rhim 2014). FTIR analysis showed that peaks corresponding to hemicellulose and lignin were not shown in the spectra of the CMF and CNC, which was due to the removal of lignin and hemicellulose by chemical treatments (Reddy and Rhim 2014). XRD analysis showed crystallinity index values of the fibres to be 35%, 45%, and 63% for the crude fibre, CMF, and CNC, respectively. The increase in crystallinity of the CMF was due to the removal of hemicellulose and lignin, which existed mainly in the amorphous regions of the fibre (Reddy and Rhim 2014). Thermogravimetry showed lower thermal stability of the CNC than CMF and the native fibre. This was probably due to the introduction of sulphate groups into the cellulose crystals through hydrolysis by sulphuric acid. The sulphate groups introduced to the outer surfaces of cellulose during the acid hydrolysis caused dehydration of cellulose fibre to reduce the thermal stability.

Reddy and Rhim 2014 from the University Grenoble Alpes, in Grenoble, France isolated and characterized cellulose nanocrystals from industrial by-products of *Agave tequilana* and barley using acid hydrolysis. Both samples were dried and ground to uniform size and subjected to 65% wt. sulphuric acid hydrolysis at 50°C with for 1h with strong agitation. Successive centrifugation and washing with deionized water was used to remove excess sulphuric acid. The resulting suspension was then dialyzed and preserved. For *Agave tequilana*, CNC of length 323 nm \pm 113 in length were viewed with AFM and DLS measurements corroborated the results with a particle size distribution curve peaking just after 300 nm. For barley, CNC of length 329 nm \pm 123 were viewed with AFM and DLS measurements showed a distribution peaking after 200 nm. Crystallinity was investigated using XRD. *Agave tequilana* CNC had higher crystallinity of 71% as compared to barley CNC with 66%. Two important peaks of cellulose degradation can be observed in DTG principally for CNC from MCC and barley. Since sulphate groups bound to the glucose units decrease the thermal stability of the CNC (Espino *et al.* 2014).

Ponce-Reyes *et al.* 2014 from the Departamento de Ingenieria Bioquimica, Prolongacion de Carpio y Plan de Ayala prepared cellulose nanoparticles from agave waste and studied their morphology and structural characterization. Dried agave fibres were milled to size less than 2.36 μ m. These were subjected to a 3 hour 5.00M NaOH treatment at 80 °C with constant agitation. After successive rinsing with deionized water, the resulting solids were treated with DMSO at 80 °C for 3 hours. An HCl: H₂SO₄: H₂O with ratio 1:3:6 was used to hydrolyse the cellulose at 80°C for 3 hours. The resulting milky white suspension was then neutralized with 2N NaOH solution and dialyzed. SEM images showed cellulose nanoparticles of

heterogeneous sizes. DLS showed the average particle size obtained to be 97 ± 30 nm within a range of 31-198 nm. XRD studies showed the crystallinity indices for MCC and CNP to be 77 % and 39.4% respectively (Ponce-Reyes *et al.* 2014).

Table below is Table 3.1 which shows a summary of literature references of CNCs produced.

Reference	Year	Biomass	Dimensions of CNCs	Characterization Technique
Sun <i>et al.</i>	2004	Sugarcane Bagasse (SCB)		FTIR ¹³ C-NMR TGA, DSC
Zhang <i>et al.</i>	2007	Cellulose fibres	(l) 470 ± 100 nm (d) 570–60 nm	AFM Capillary Electrophoresis SEM TEM ¹³ C CP/MAS NMR XRD
Troedec <i>et al.</i>	2008	Hemp fibres		FTIR
Zhao <i>et al.</i>	2010	Sugarcane Bagasse (SCB)		FTIR XRD TGA & DTG
Mandal and Chakrabarty	2011	Sugarcane Bagasse (SCB)	(l) 18.17 - 220 nm	FTIR TGA & DTG DSC AFM SEM TEM XRD DLS
Liu <i>et al.</i>	2011	Microcrystalline Powder	(l) 90 ± 50 nm (d) 10 ± 4 nm	WAXD HRTEM SEM ODR
Abraham <i>et al.</i>	2011	Raw banana jute Pineapple leaf fibre	(d) < 100 nm	FTIR XRD SEM TGA & DTG
Teixeira <i>et al.</i>	2011	Sugarcane Bagasse (SCB)	(l) 255 ± 55 nm (d) 4 ± 2 nm	STEM XRD TGA & DTG
Pereira <i>et al.</i>	2011	Sugarcane Bagasse (SCB)		FTIR XRD TGA & DTG

				SEM
Chen et al.	2012	Potato peel waste	(l) 410 ± 181 nm	FTIR TEM XRD
Kopania, Wietecha and Ciechańska	2012	Herein rape, hemp and flax straws		
Fazli <i>et al.</i>	2012	Cotton linter		
Sheltami <i>et al.</i>	2012	mengkuang leaves (<i>Pandanus tectorius</i>)	(l) 50 to 400 nm (d) 5 – 25 nm	FESEM FTIR XRD TGA & DTG
Lu and Hsieh	2012	Rice straw	(l) 50 to 700 nm (d) 10 to 65 nm	XRD O-PLM SEM EDS TEM XRD AFM FTIR
		chardonnay grape skins	(d) 10-100 nm,	FTIR XRD DSC TGA & DTG SEM TEM AFM
Yu <i>et al.</i>	2012	Bamboo	(l) 200-500 nm (d) < 20 nm	FTIR XRD TEM
Rosli, Ahmad and Abdula	2013	<i>Agave angustifolia</i>	(l) 170-500 nm (d) 8-15 nm	FESEM TEM FTIR XRD TGA & DTG
Maiti <i>et al.</i>	2013	China cotton,	(d) 30 - 60 nm	TEM DLS XRD FTIR SEM TGA & DTG
		South African Cotton	(d) 2 - 10 nm	
		Waste tissue papers	(d) 10 - 90 nm	
Santos <i>et al.</i>	2013	Pineapple leaf	(l) 210 -240nm (d) 2 -5 nm	FTIR XRD AFM DLS
Silvério <i>et al.</i>	2013	Corn cob	(l) 287.3 ± 75.5 nm	FTIR XRD

			(d) 4.90 ± 1.34 nm	AFM SEM TGA & DTG
Kumar <i>et al.</i>	2013	Agro waste Sugarcane Bagasse (SCB)	(l) 250 – 480 nm (d) 20 – 60 nm	FESEM TEM AFM EDX FTIR
Normand, Moriana and Ek	2014	spruce bark	(l) 175.3 ± 61.8 nm (d) 2.8 ± 0.8 nm and	AFM DLS FTIR WAXS TGA & DTG
Li <i>et al.</i> 2014	2014	Sugar beet pulp (SBP)	(d) 10–70 nm	FTIR SEM TEM XRD TGA & DTG
Haafiz <i>et al.</i>	2014	Oil palm	(d) 10 -100 nm	FTIR XRD SEM TEM
Reddy and Rhim	2014	Garlic skin	(d) 58–96 nm.	FTIR XRD SEM TEM TGA & DTG
		<i>Agave tequilana</i> barley	(l) 323 ± 113 (l) 329 ± 123	FTIR XRD DLS AFM
Ponce-Reyes <i>et al.</i>	2014	agave waste	97 ± 30 nm	DLS XRD SEM

Table 3.1 Summary of the references used in the literature review

MATERIALS AND EXPERIMENTAL METHODOLOGY

4.1 Materials and Methods

Soda pulped sugarcane bagasse was provided a local sugarcane mill in KwaZulu-Natal. Excess water was removed from the pulp by means of a mechanical press which produced bagasse pulp “cakes” of 12cm diameter and 5 cm height. These cakes were allowed to dry completely at room temperature over a period of 6 – 8 days. When dried, the cakes were stored in plastic Ziploc bags.



Figure 4.1 Photograph of dried soda pulped bagasse

4.2 Experimental Procedure

The experimental procedure for the isolation of cellulose nanocrystals is depicted in the Figure 4.2 below. Detailed description of the process is given in the text that follows.

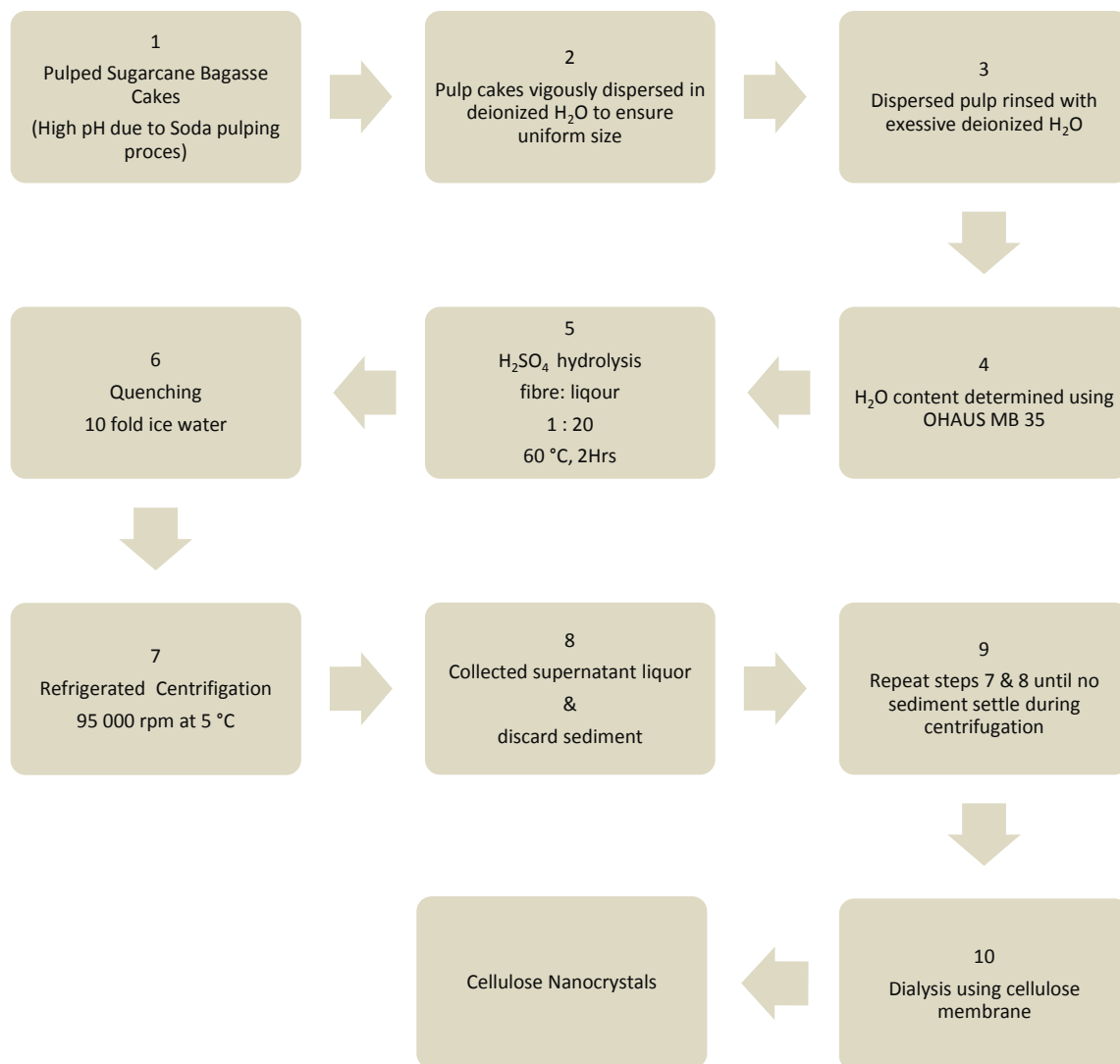


Figure 4.2 The experimental procedure for the isolation of cellulose nanocrystals from pulped sugarcane bagasse.

4.2.1. Neutralization of Pulped Bagasse

Before use the dried pulped cakes were dispersed in deionized water with vigorous mechanical agitation until uniform fibre size. The fibres were separated from solution using a nylon mesh. The fibres were then washed with excessive amounts of water until the pH of the pulp was between 7 and 8. Excess water was removed from the neutralized fibres and moisture content determined using an OHAUS MB 35 moisture analyser.



Figure 4.3 Photograph of OHAUS MB 35 Moisture Analyser

4.2.2 Preparation of Cellulose Nanocrystals

The neutralized pulped bagasse was subjected to sulphuric acid hydrolysis. A fibre to liquor ratio (grams : ml) of 1: 20 was used for the hydrolysis. The water content of the pulp was compensated by preparing an acid solution that would incorporate the water content of the pulp. The acid hydrolysis was carried out at using a 45 % m/v sulphuric acid solution at 60 °C for about 2 hours with constant vigorous mechanical agitation. At 30 minute intervals, progress was monitored by viewing a very dilute solution of the hydrolysis liquor in a vial against sunlight. When no fibres were visible, the reaction was quenched with 10-fold ice water.



Figure 4.4 Photograph of the experimental setup for the preparation of CNC

4.2.3. Isolation of the Cellulose Nanocrystals

The quenched hydrolysis liquor was centrifuged at 95 000 rpm at 5 °C using a Perkin Elmer refrigerated centrifuge. The supernatant liquid was collected and centrifuged repeatedly until no sediment collected at the bottom of the centrifuge vial. The sediment collected was labelled hydrolysis residue and the supernatant liquor diluted with deionized water and dialyzed against deionized water for 4 days using a cellulose membrane. After dialysis the solution was centrifuges and the supernatant liquor discarded. The sediment was dispersed in deionized water and labelled as the cellulose nanocrystal solution.

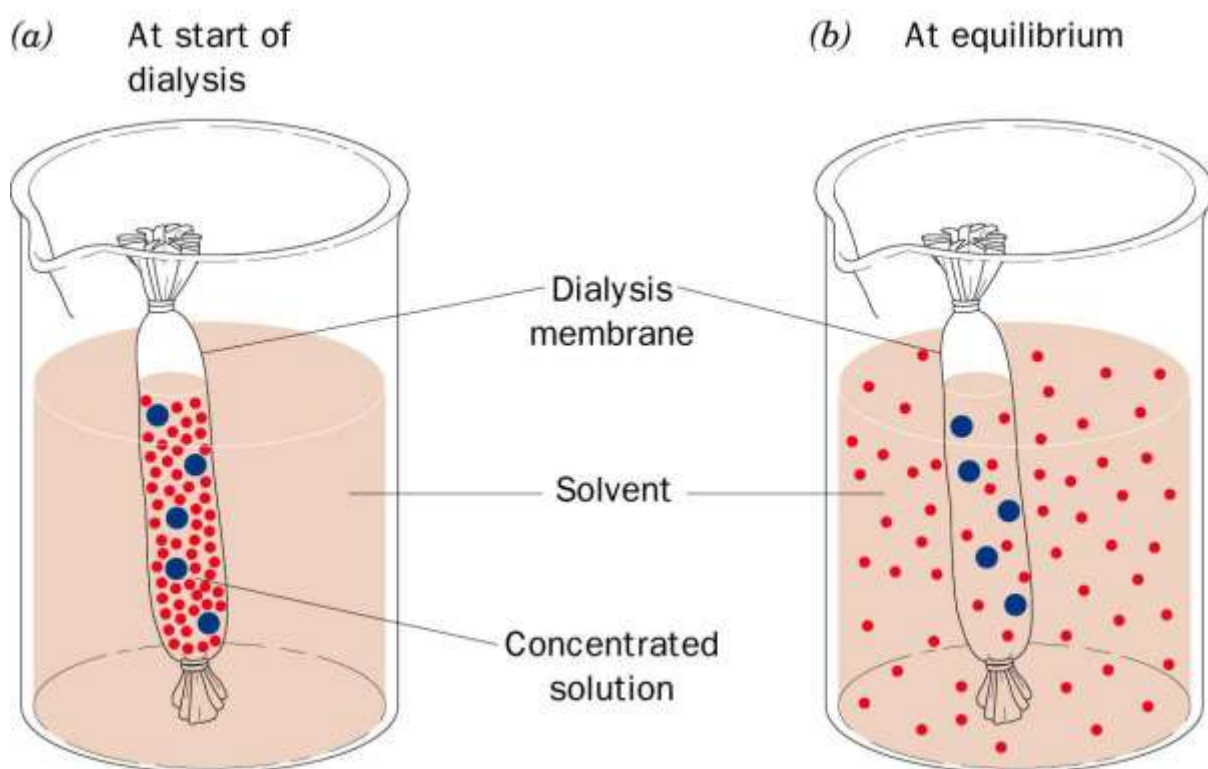


Figure 4.5 The experimental procedure for the isolation of cellulose nanocrystals from pulped sugarcane bagasse. Adapted from (*Selective Permeability of Dialysis Tubing Lab: Explained* 2016)

4.3 Characterization

4.3.1 Particle Size Determination

Particle size measurements have been widely employed in the characterization of cellulose nanocrystals. The measurements are used to determine the range of the particle size of the nanocrystals which is indication of the extent of the hydrolysis reaction. Particle size distribution was determined using a HORIBA LB 550 (Dynamic Light Scattering) instrument. 5mL of the turbid aqueous suspension was placed in a quartz cuvette after shaking and the determination was performed.

4.3.2 Thermogravimetric Analysis

Thermogravimetric analysis is a technique wherein the loss of mass of a substance is monitored as a function of temperature or time while the sample specimen is subjected to a controlled temperature program in a controlled atmosphere. Thermogravimetric analysis can provide information pertaining to the sample like quantify loss of water, loss of solvent, loss of plasticizer, decarboxylation, pyrolysis, oxidation, decomposition, weight percent filler, weight percent amorphous or crystalline component in polymer. Thermogravimetric studies were performed on a TA Q500 TGA. The heating rate was set at 5°C/min from room temperature to 650 °C and the Nitrogen purge rate was 10ml/min. All analyses were performed on platinum crucibles which were washed in nitric acid and dried before use.

4.3.3 Attenuated Total Reflectance – Fourier Transform Infra-red Spectroscopy

FTIR spectroscopy is the analytical technique of choice for monitoring functional group changes in biomass samples. A Perkin Elmer Spectrum 100 FTIR spectrometer equipped with a Attenuated Total Reflection Accessory was used. Dried pulped bagasse and pre-treated samples were used in the FTIR analysis. A 12 hour freeze dried sample of the cellulose nanocrystals suspension was used in the FTIR analysis. An average of 50 scans were performed in the region $4\ 000 - 600\ \text{cm}^{-1}$.

4.3.4 Wide Angle X-Ray Diffraction Studies (WAXRD)

A PAN Analytical X'Pert PRO X-Ray Diffractometer fitted with a Cu K α radiation source was used to investigate the XRD spectra of the cellulosic sample was used. Scattered radiation was detected in the range $2\theta = 5 - 50^\circ$, at a speed of $3^\circ/\text{min}$ operating V&I = 45kV, 40mA.

4.3.5 Atomic Force Microscopy - Morphological Analysis

AFM utilises a cantilever with a sharp probe which scans the surface of the specimen. Atomic force microscopy will measures a number of different forces depending on the situation and the sample that you want to measure and produces quantitative, 3-D images and less intrusive surface measurements with resolution of a few microns to below 10 Angstroms with the added benefits of small sample size and ease of sample preparation. A few drops of a highly diluted solution of the cellulose nanocrystals were placed on a silica substrate and allowed to air dry. The analysis was performed on a Digital Instruments Nanoscope, Veeco, MMAFMLN-AM Atomic Force Microscope.

4.3.6 Scanning Electron Microscopy Studies

Scanning electron micrographs of untreated pulped bagasse, microcrystalline cellulose and cellulose nanocrystals were captured using a JEOL- JSM 7500F Field Emission - Scanning Electron Microscope. Prior to imaging, the samples were coated using the gold sputtering method.

4.3.7 Transmission Electron Microscopy Studies

Transmission electron micrographs were captured using a JEOL-Jem 2100 with a Leica EMFC6 (LN2 attachment). A dilute aqueous suspension of the nanocrystals was sonicated and deposited on holy carbon on a copper grid where it was allowed to dry at room temperature and subsequently viewed.

RESULTS

5.1 Dynamic light scattering particle size determination

The following figures, Figure 5.1 – 5.6 show the experimental results obtained during

The particle size determination of the CNC and MCC obtained after acid hydrolysis.

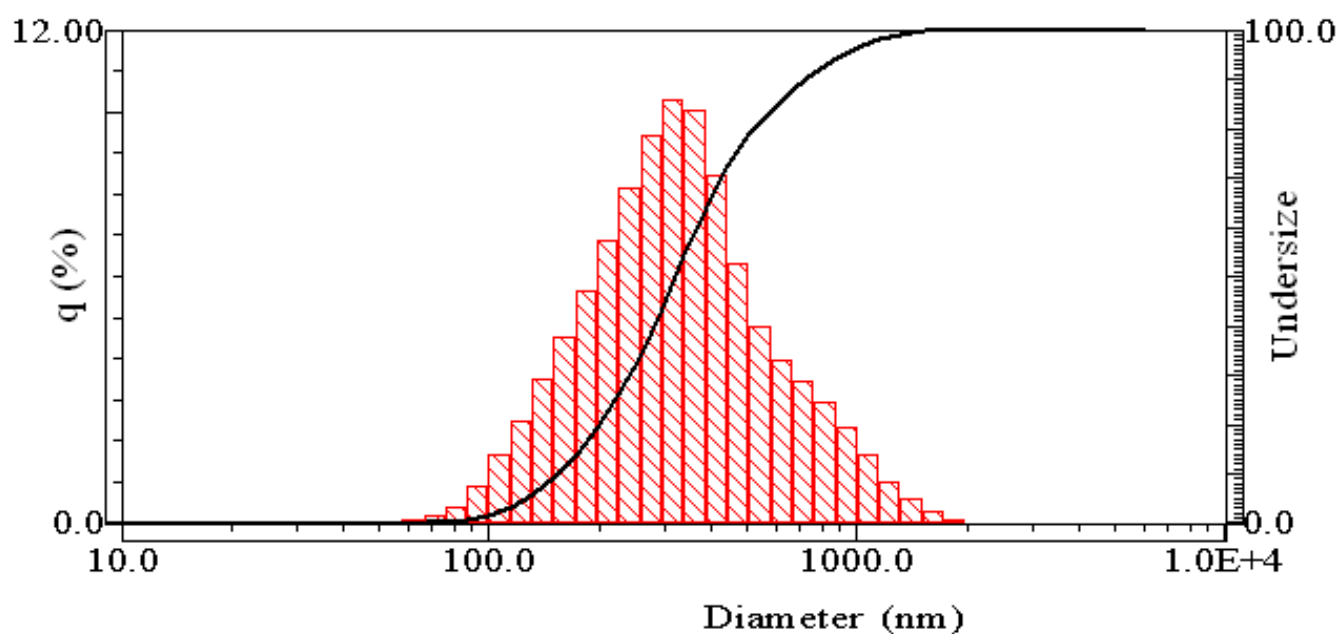


Figure 5.1 CNC Volume Data

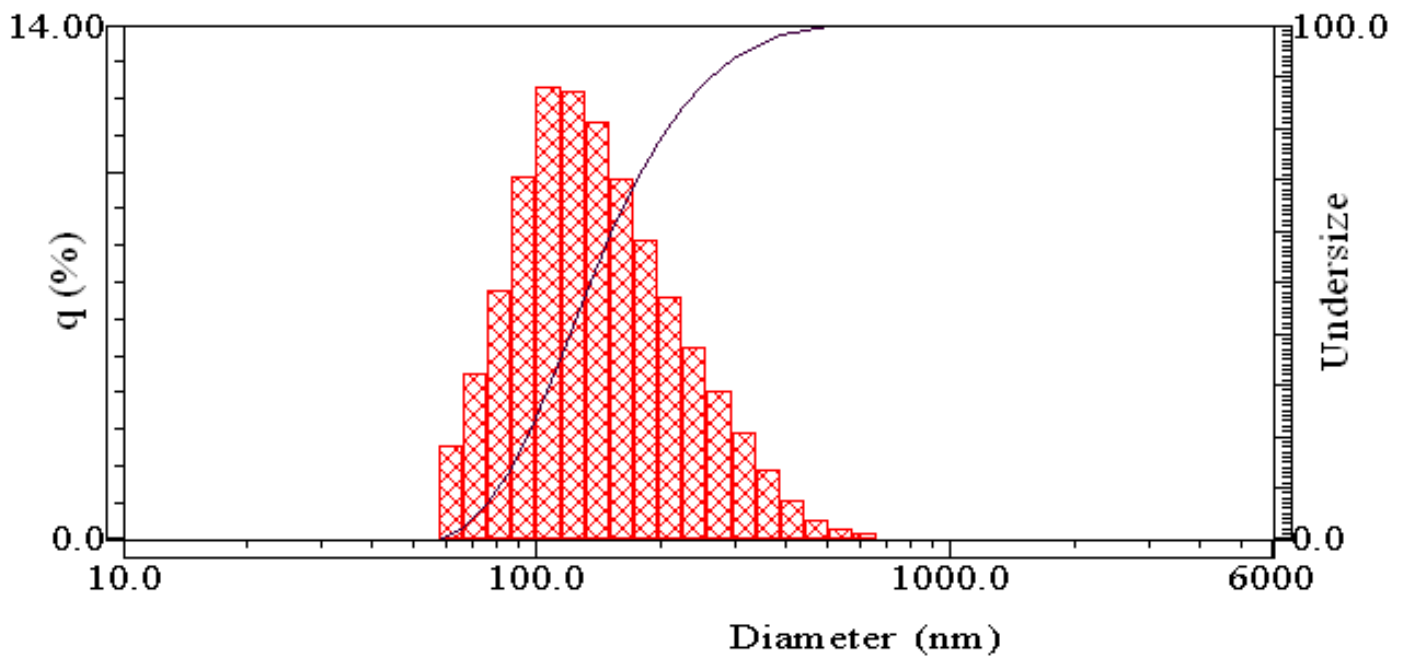


Figure 5.2 CNC Number Data

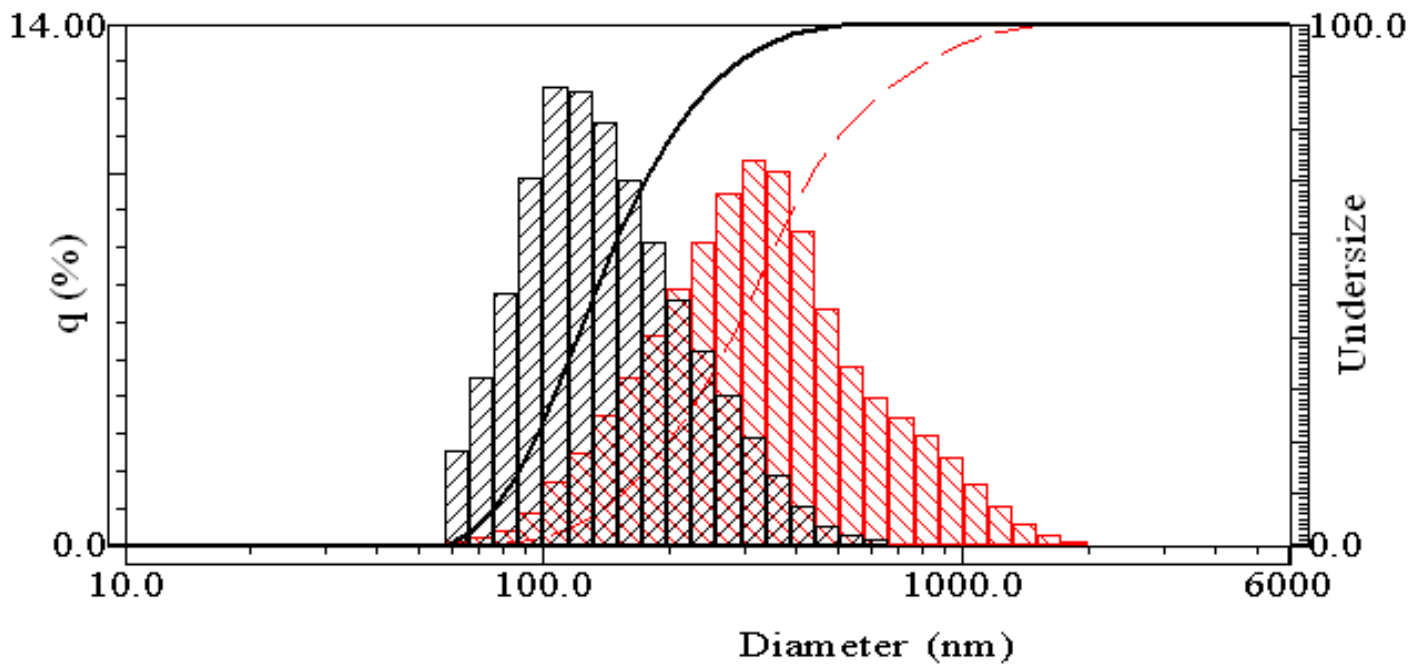


Figure 5.3 CNC Number (Black) vs CNC Volume (RED)

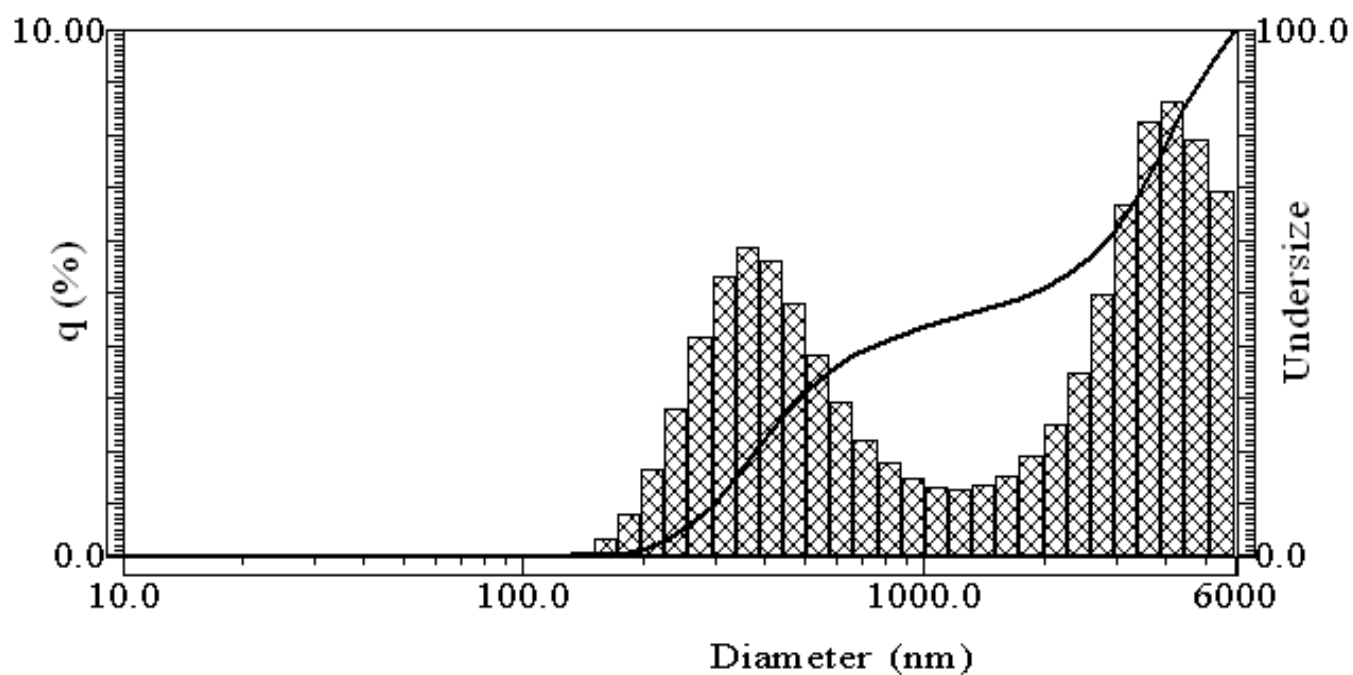


Figure 5.4 MCC Volume Data

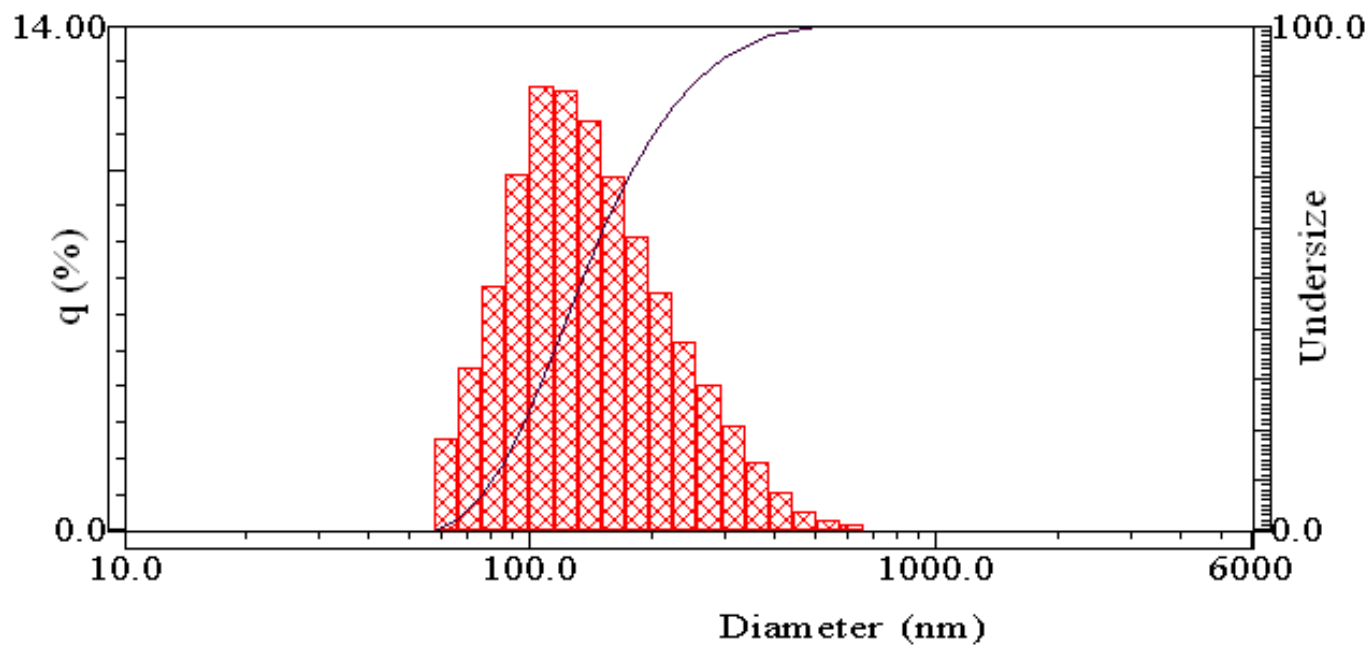


Figure 5.5 MCC Number Data

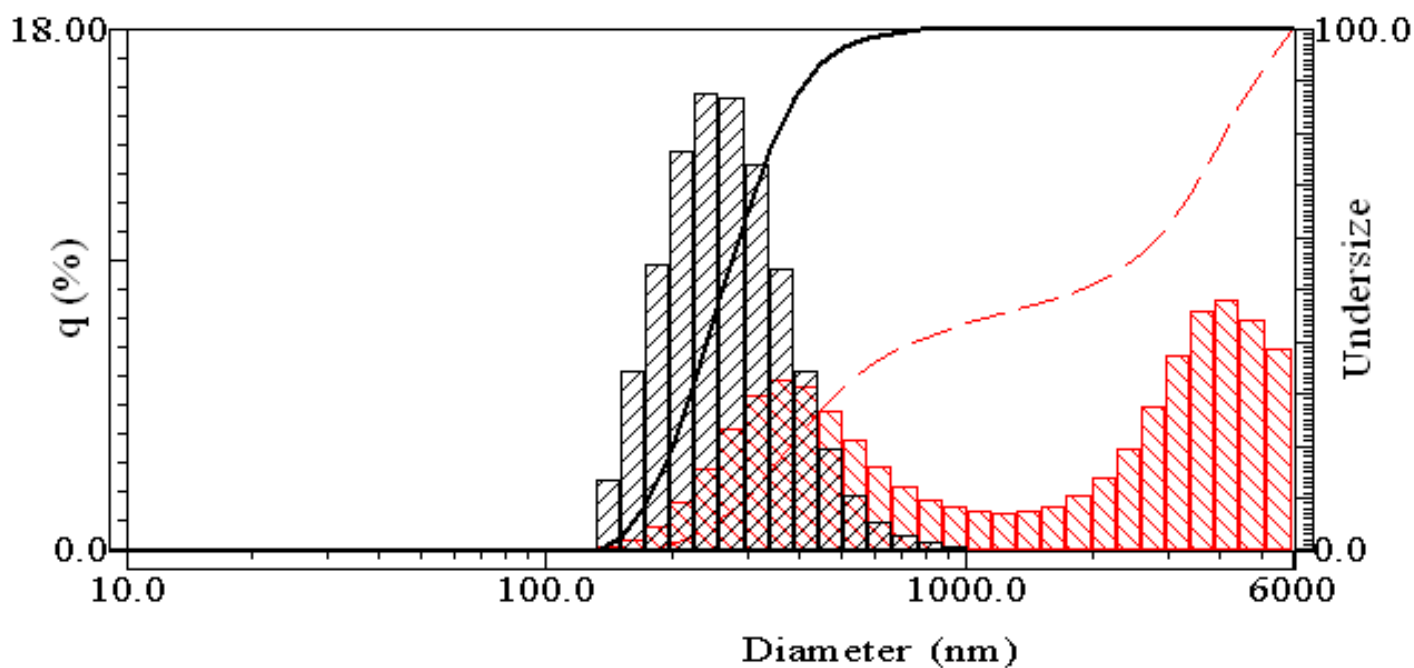


Figure 5.6 MCC Number (Black vs MCC Volume (Red))

5.2 Thermogravimetric Analysis

5.2.1 TGA Experimental Data

The following figures, Figure 5.7 – 5.13 show the experimental results obtained during the thermogravimetric and differential thermogravimetric analysis of the initial dried pulp sample, the MCC and the CNCs produced by the acid hydrolysis.

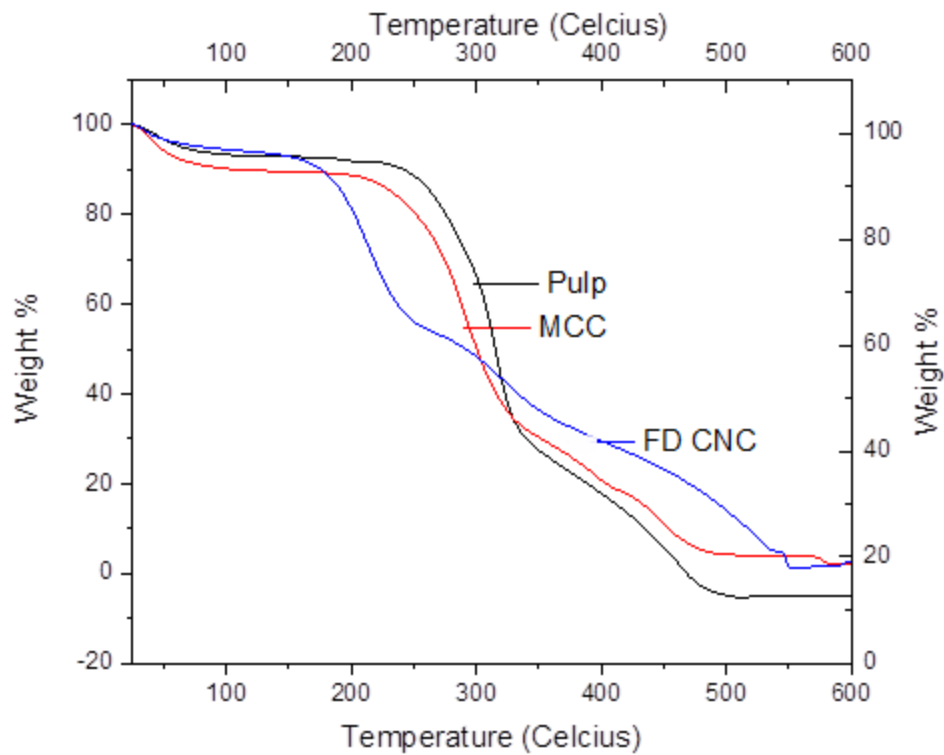


Figure 5.7 The combined TGA profiles of pulped bagasse, FD CNC and MCC

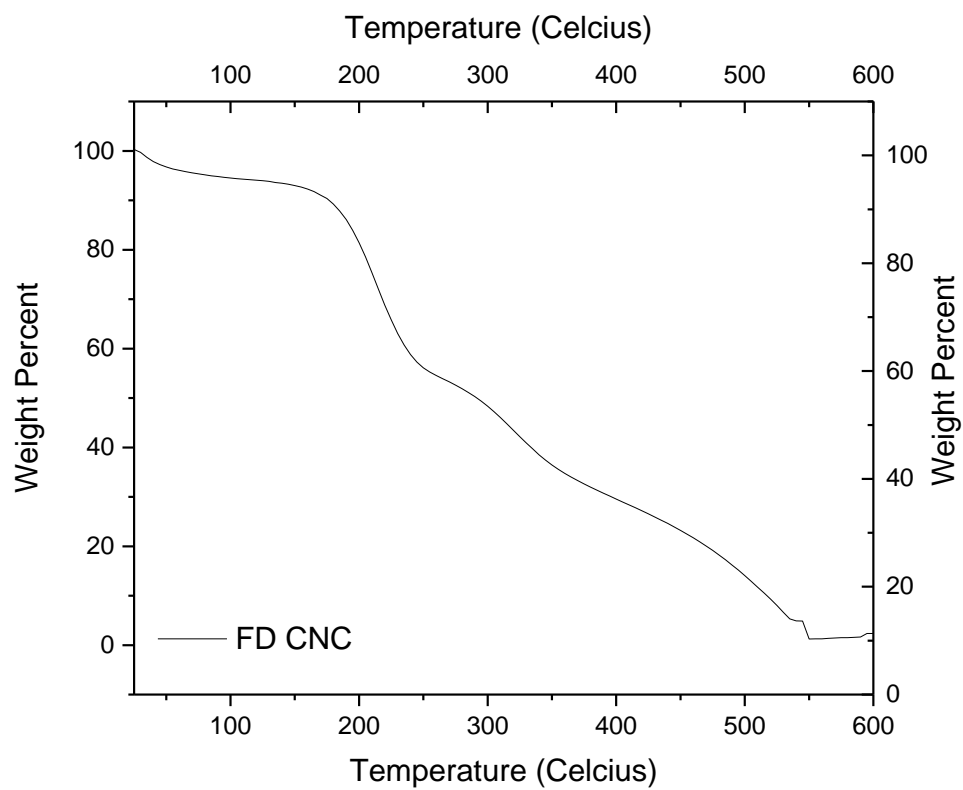


Figure 5.8 The TGA profile of FD CNC

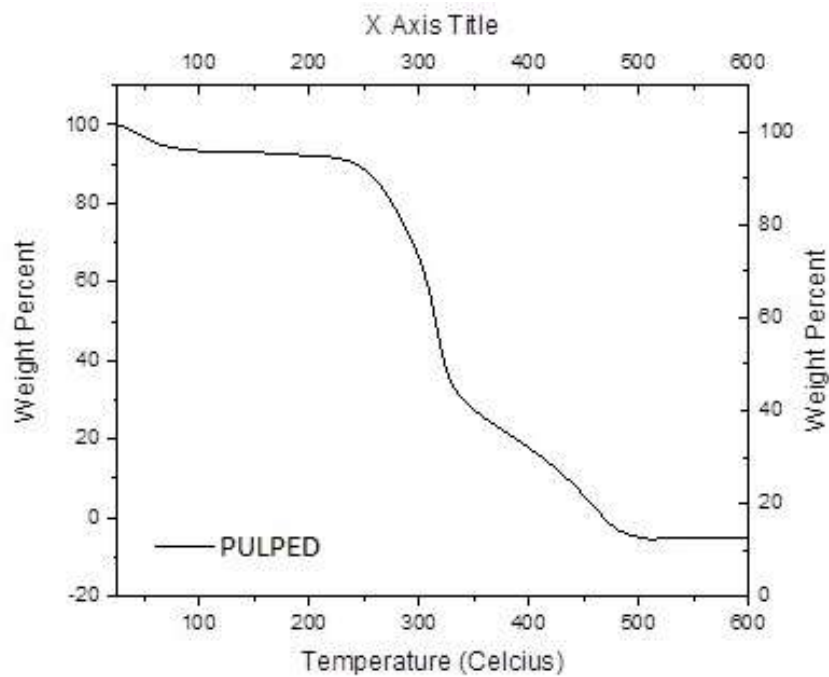


Figure 5.9 The TGA profile of pulped bagasse

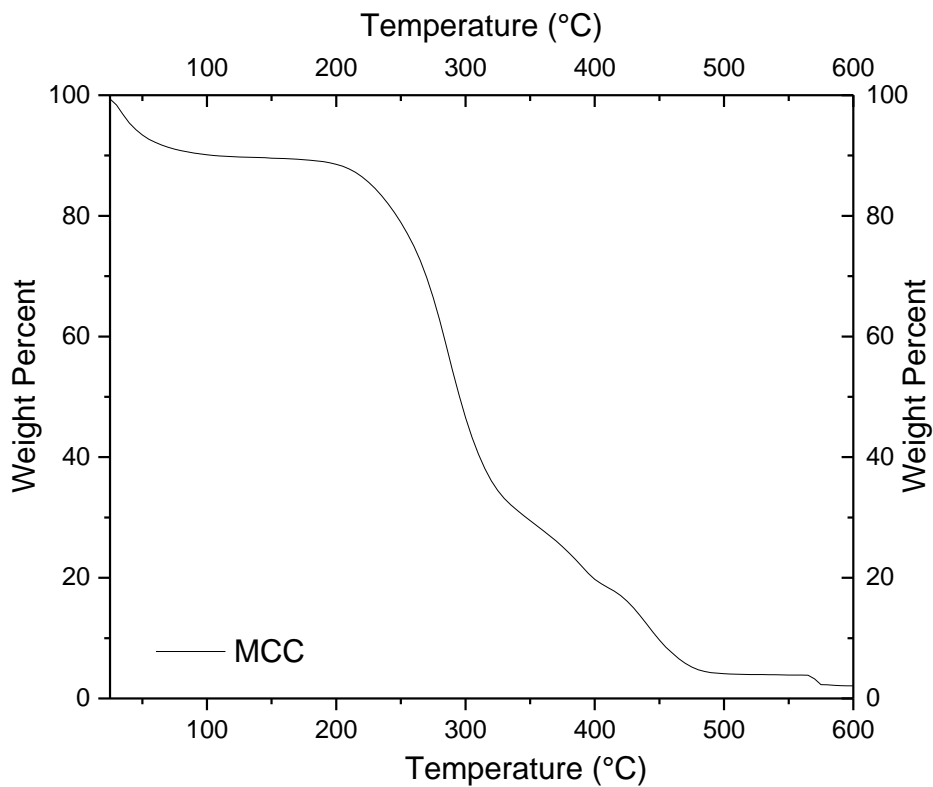


Figure 5.10 The TGA profile of MCC

5.2.2 DTG Experimental Data

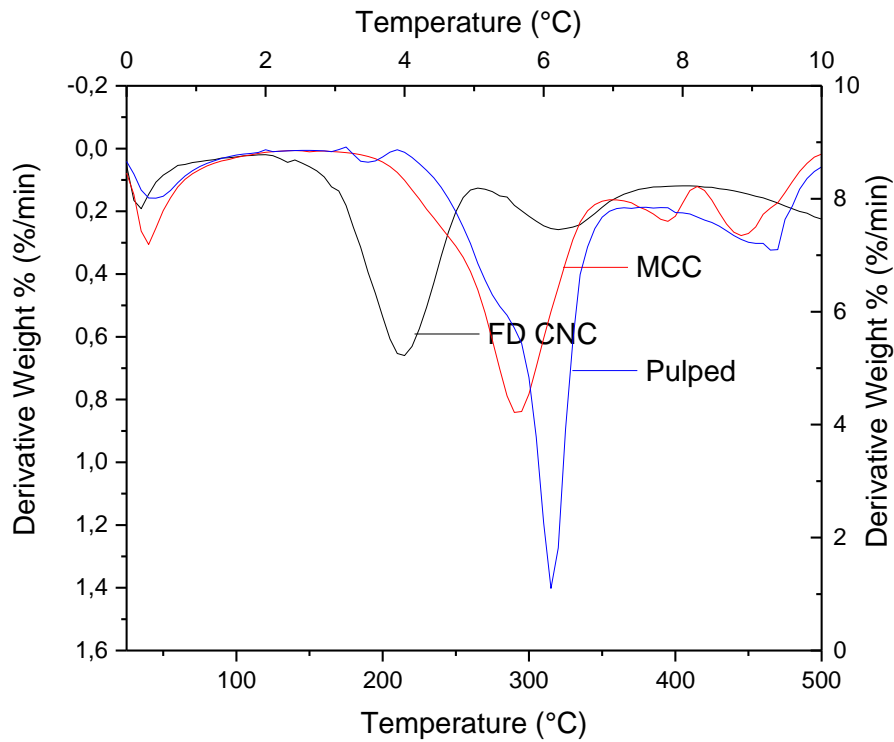


Figure 5.11 The combined DTG profiles of pulped bagasse, FD CNC and MCC

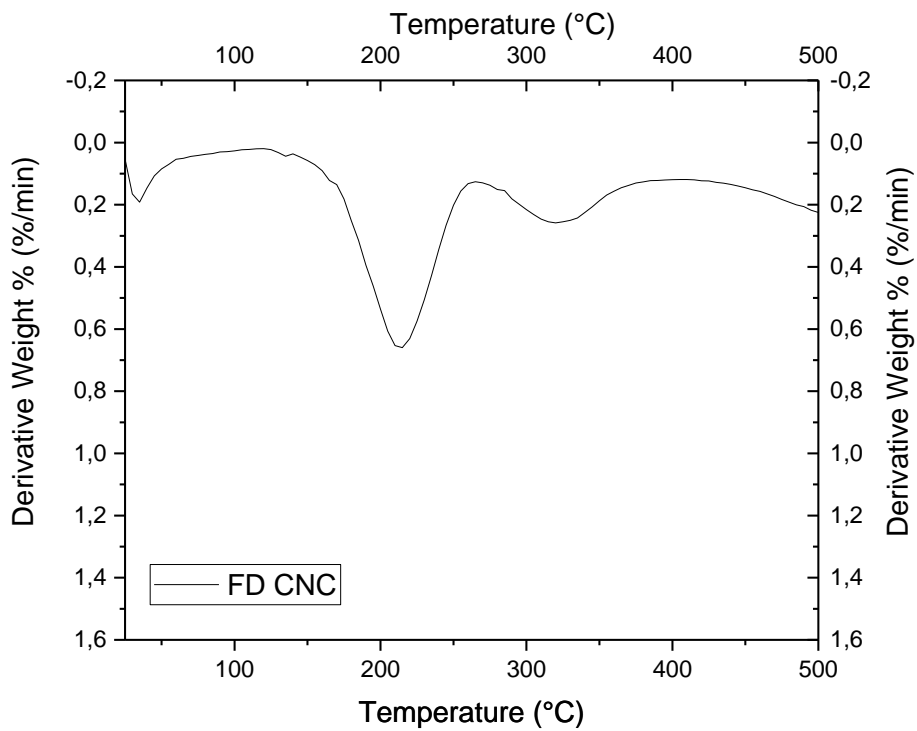


Figure 5.12 The DTG profile of FD CNC

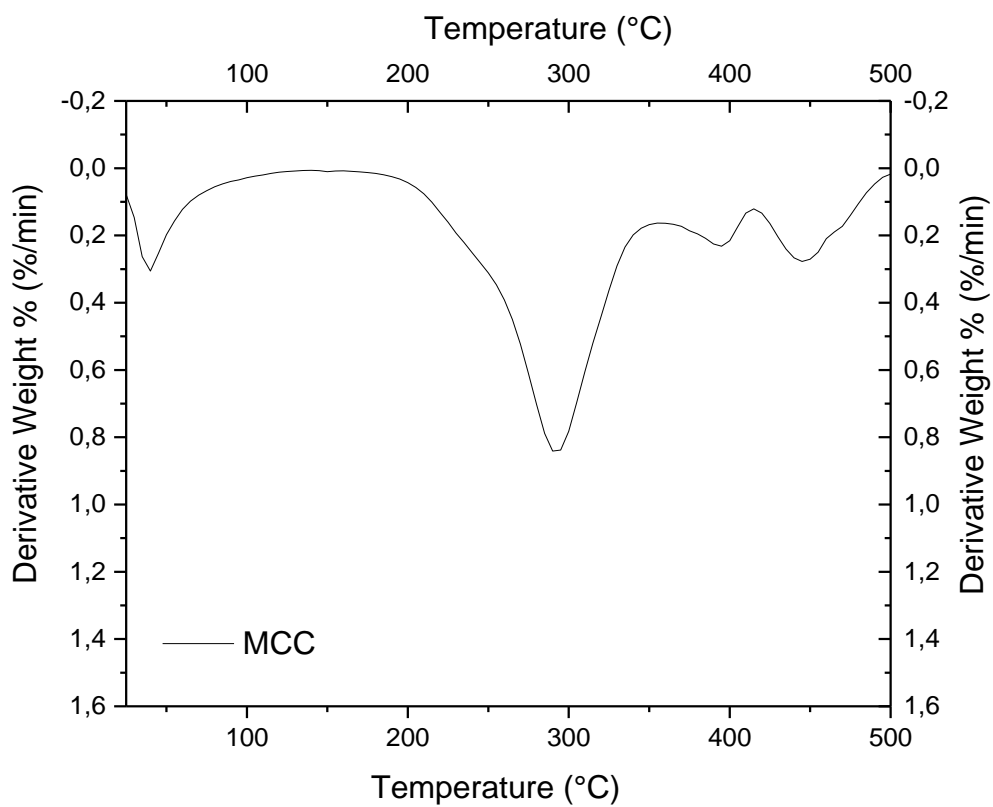


Figure 5.13 The DTG profile of MCC

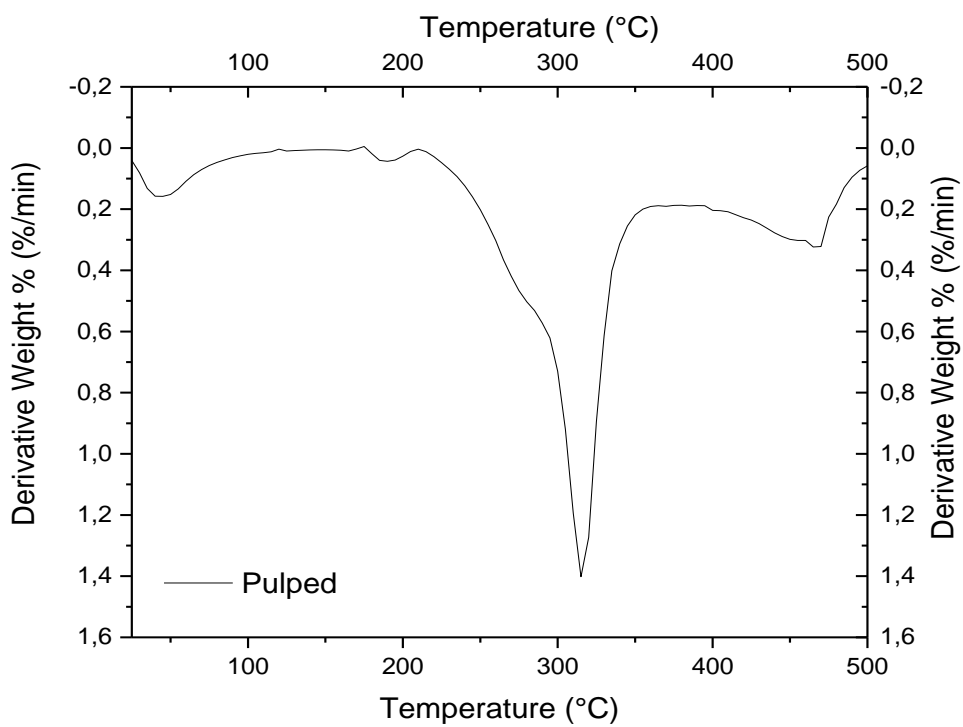


Figure 5.14 The DTG Profile of pulped bagasse

5.3 Attenuated Total Reflectance Fourier Transform Infra-red Analysis

The following figures, Figure 5.14 – 5.17 show the experimental results obtained during the attenuated total reflectance fourier transform infra-red analysis of the initial dried pulp sample, the MCC and the CNCs produces by the acid hydrolysis.

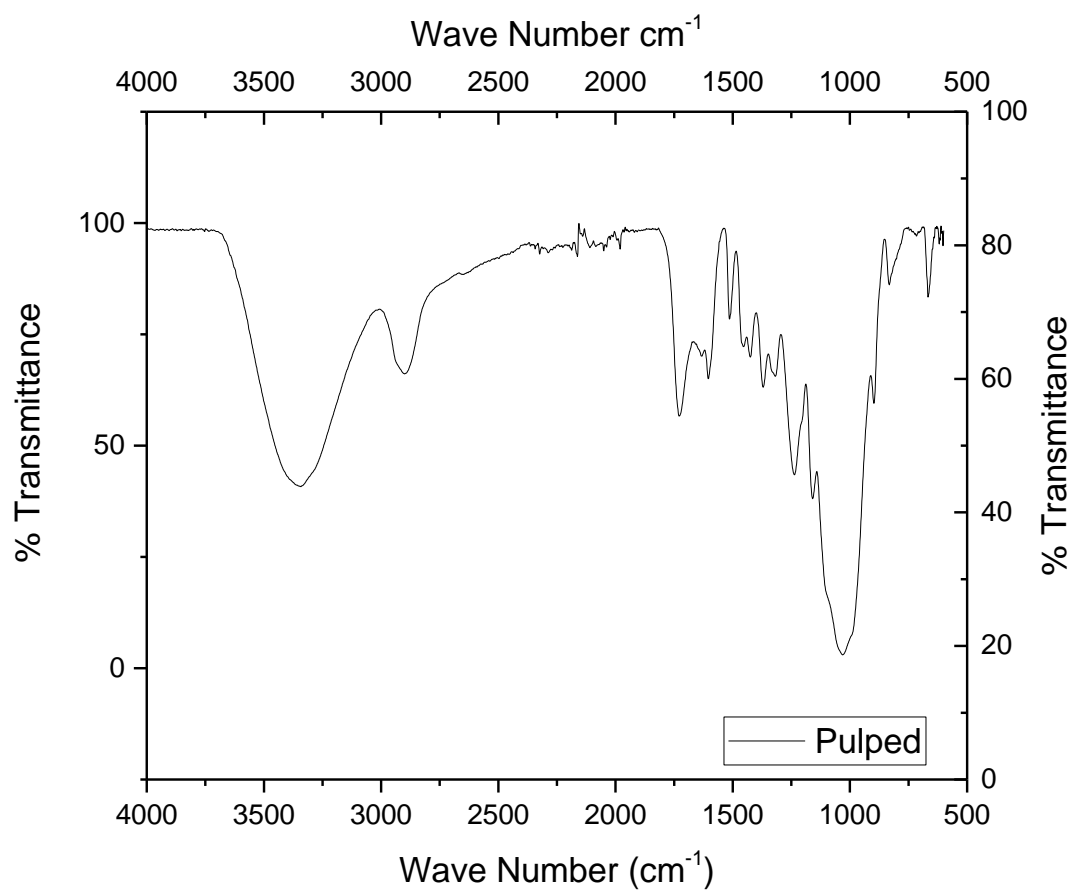


Figure 5.15 The ATR-FTIR spectra of pulped bagasse

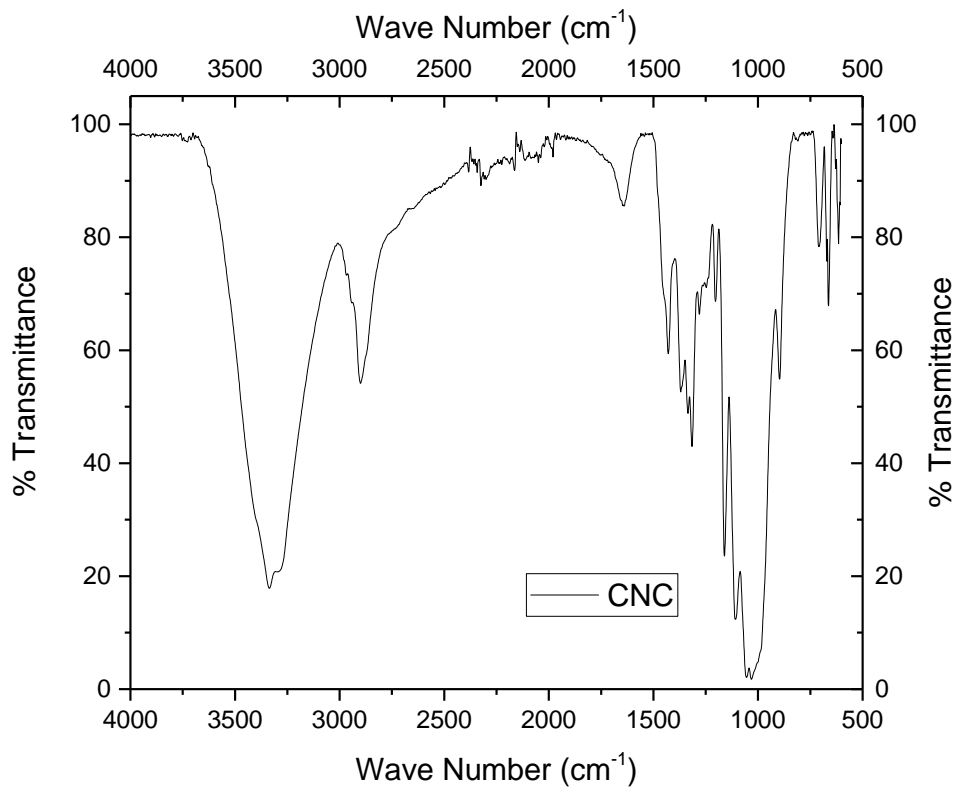


Figure 5.16 The ATR-FTIR profile of FD CNC

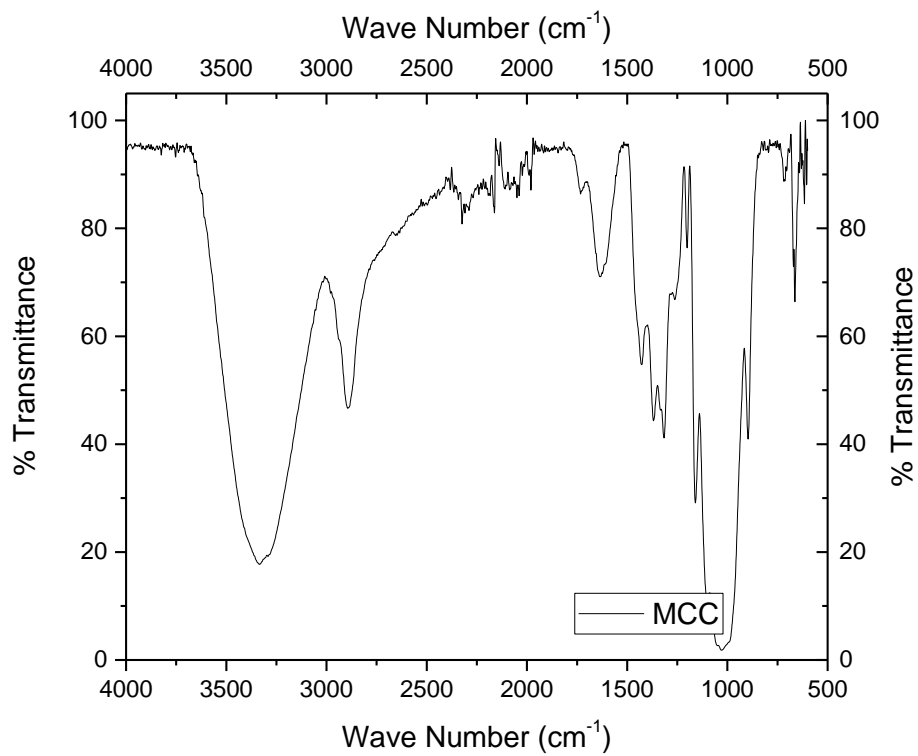


Figure 5.17 The ATR-FTIR spectrum of MCC

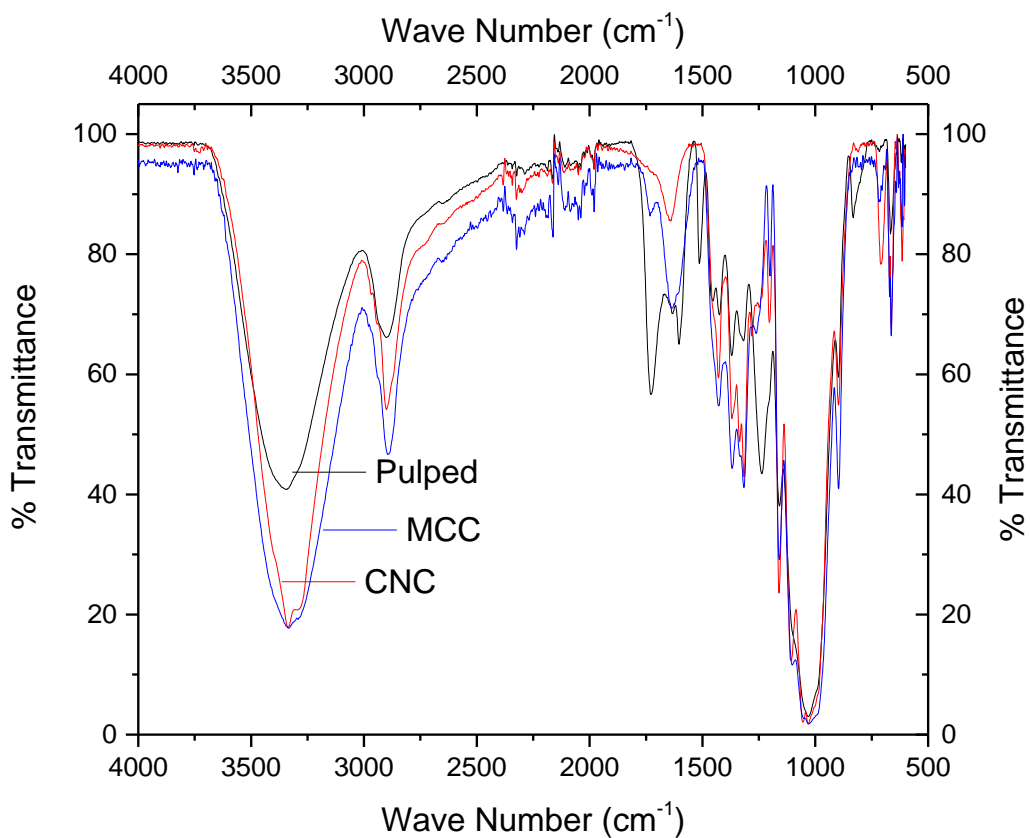


Figure 5.18 The combined ATR-FTIR spectra of pulped bagasse, MCC and FD CNC

5.4 Wide Angle X-Ray Diffraction Studies

The following figures, Figure 5.18 – 5.21 show the experimental results obtained during X-ray diffraction studies of the initial dried pulp sample, the MCC and the CNCs produces by the acid hydrolysis.

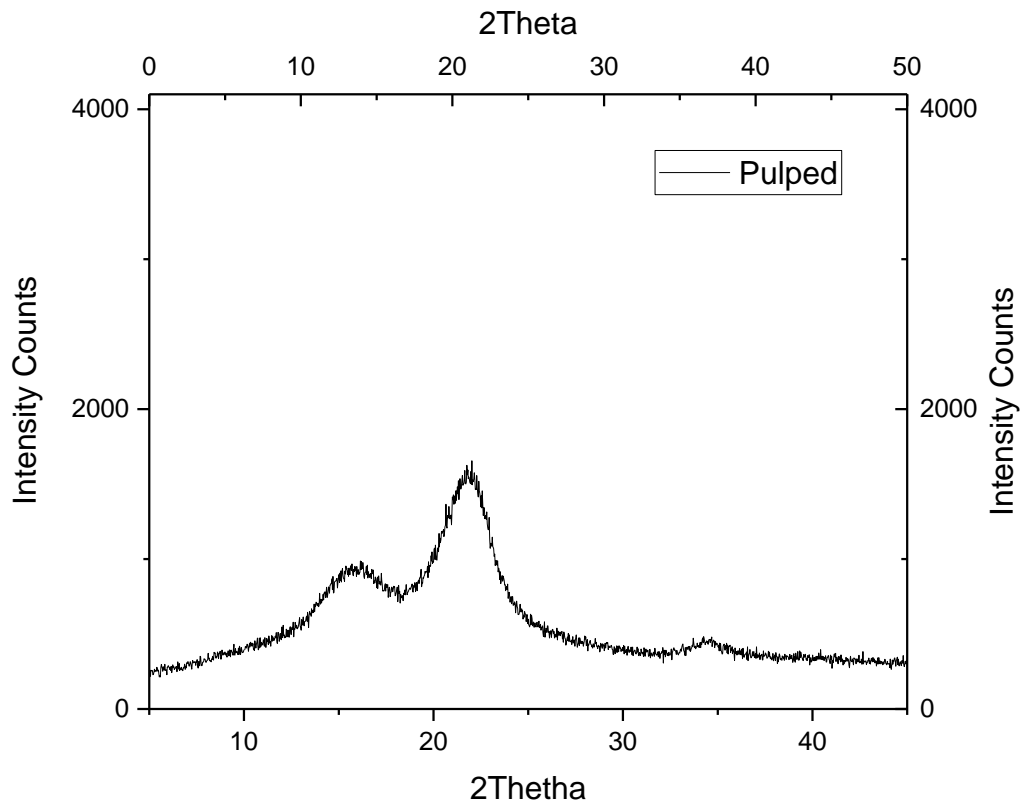


Figure 5.19 XRD diffractogram of pulped bagasse

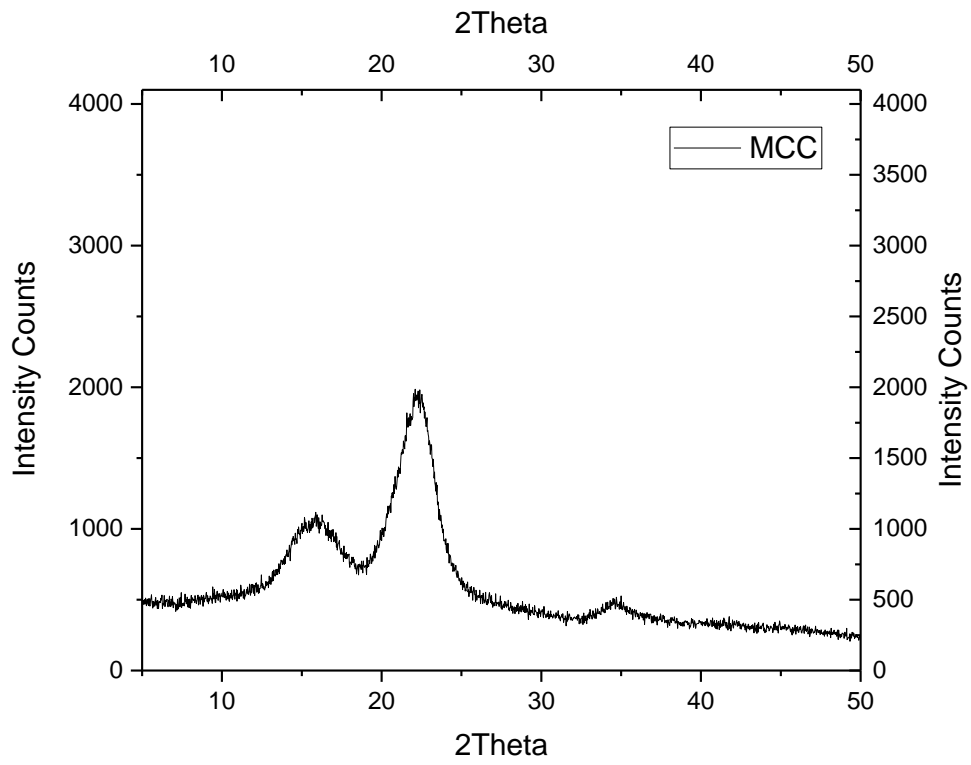


Figure 5.20 XRD diffractogram of MCC

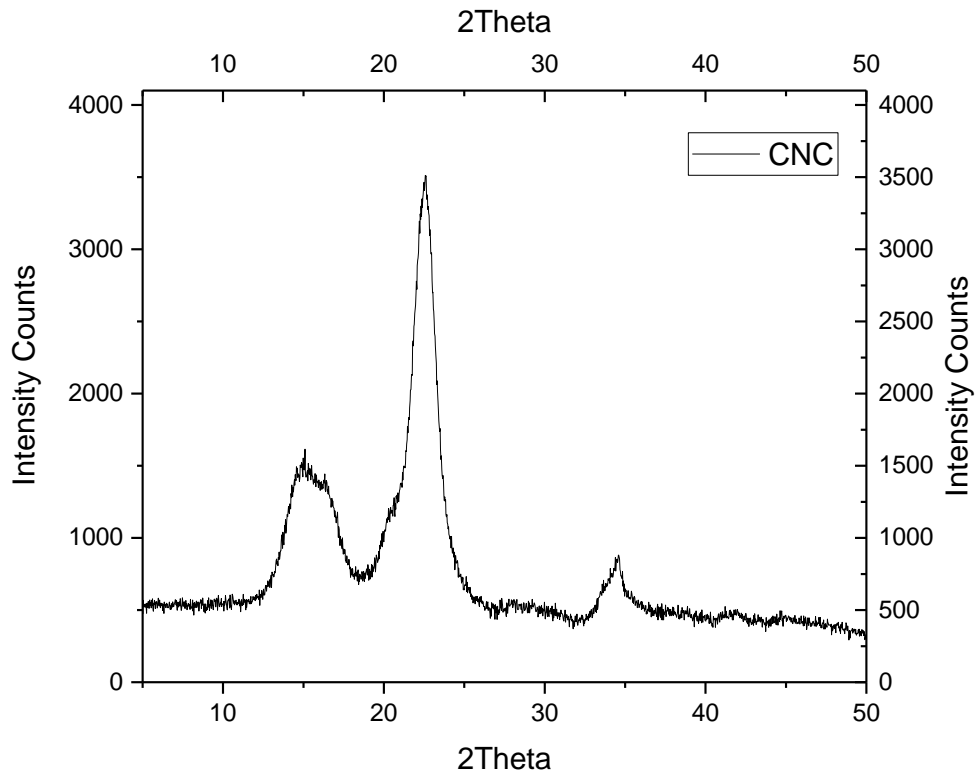


Figure 5.21 XRD diffractogram of FD CNC

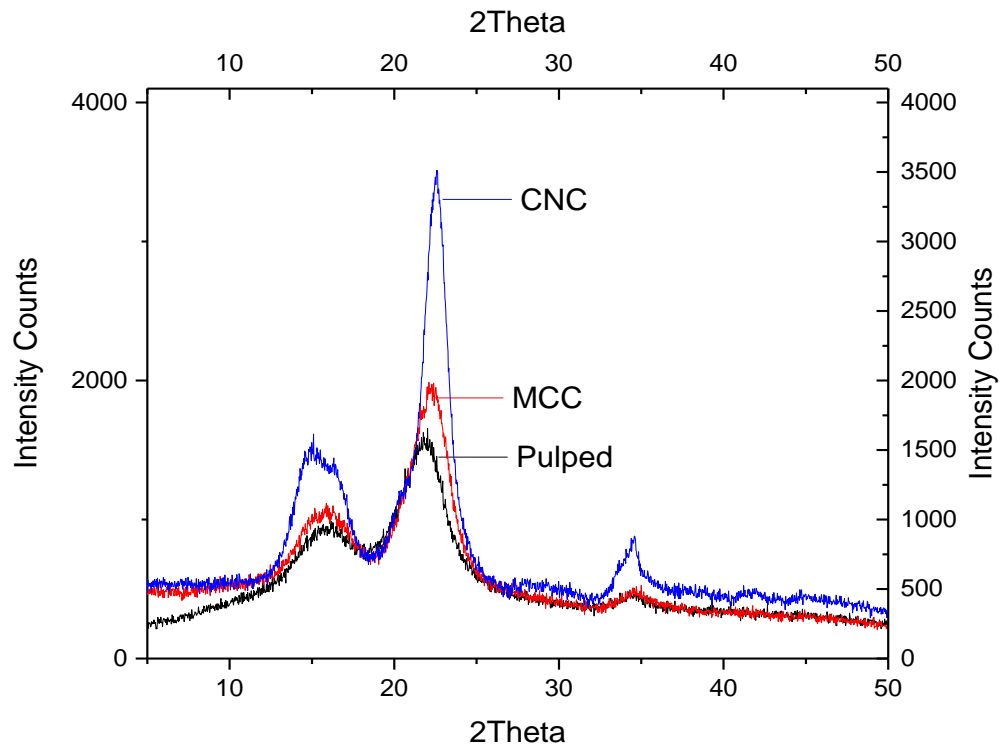


Figure 5.22 The combined XRD diffractograms of CNC, MCC and pulped bagasse

5.5 Atomic Force Microscopy

The following figures, Figure 5.22 – 5.25 show the micrographs obtained during the atomic force microscopy analysis of the CNCs produces by the acid hydrolysis.

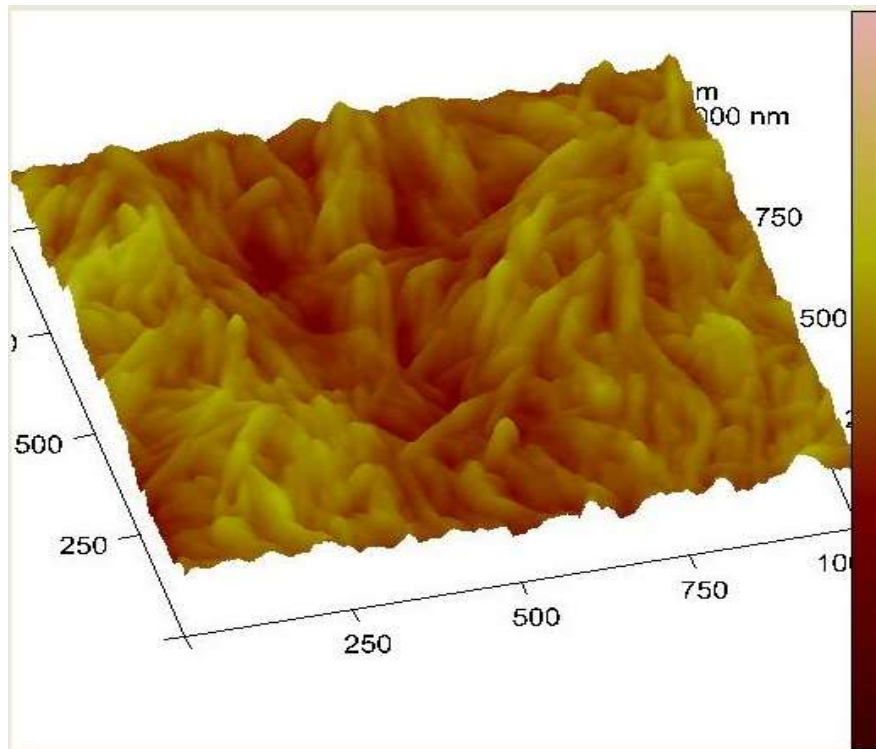


Figure 5.23 CNC 3D AFM micrograph

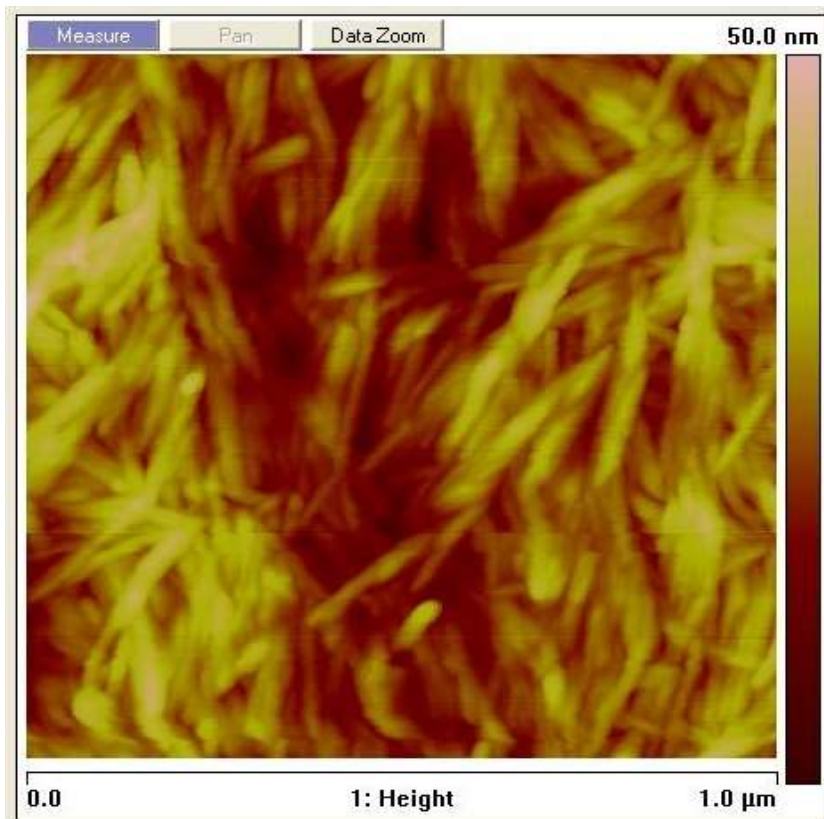


Figure 5.24 CNC height micrograph

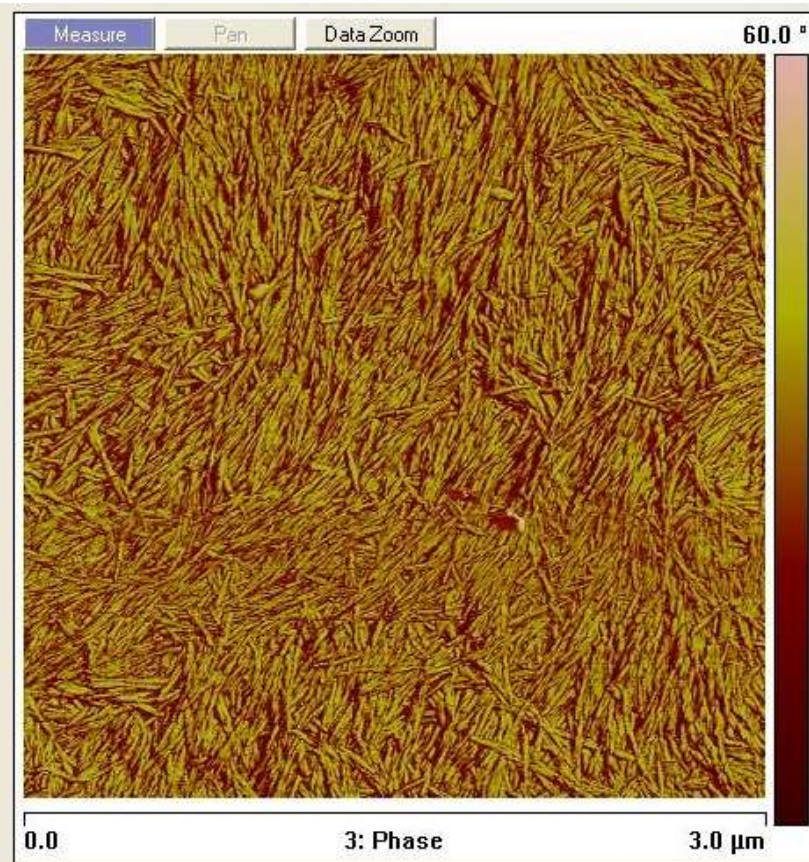


Figure 5.25 CNC phase micrograph

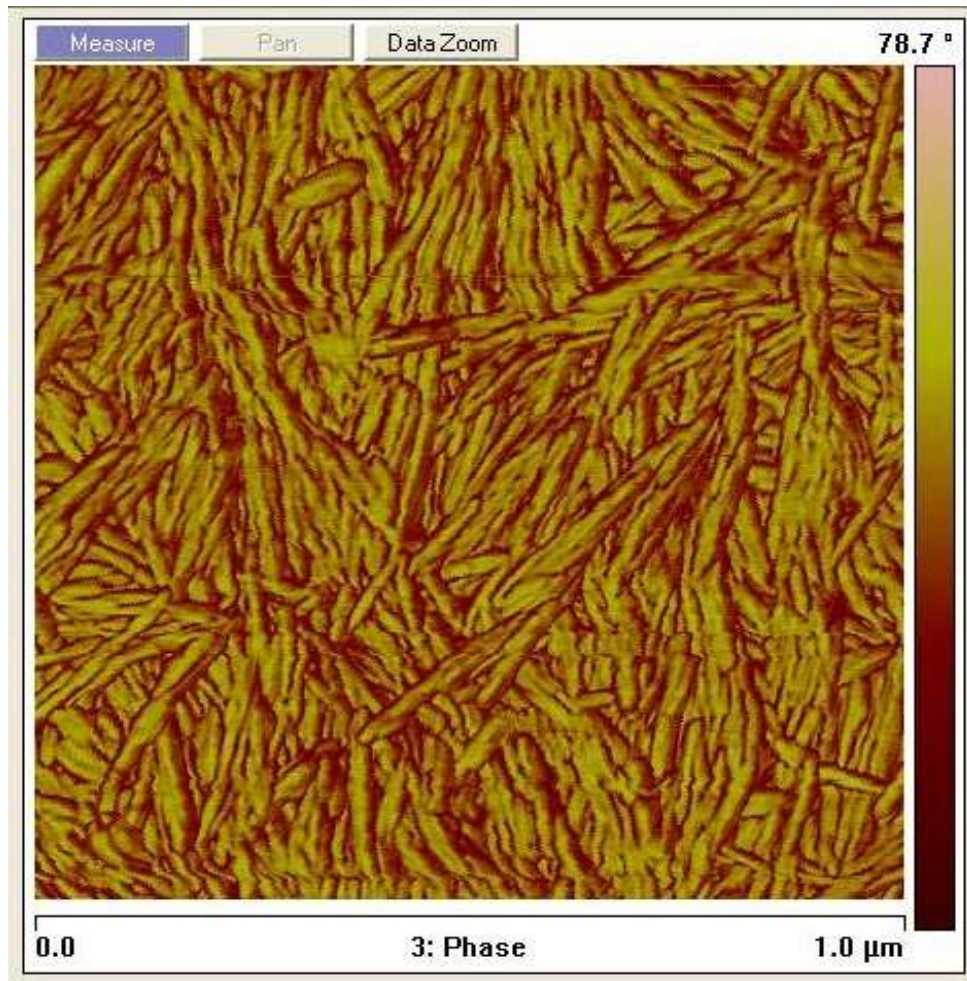


Figure 5.26 CNC phase micrograph

5.6 Scanning Electron Microscopy

The following figures, Figure 5.26 – 5.31 show the experimental results obtained during the scanning electron microscopy analysis of the initial dried pulp sample, the MCC and the CNCs produced by the acid hydrolysis.

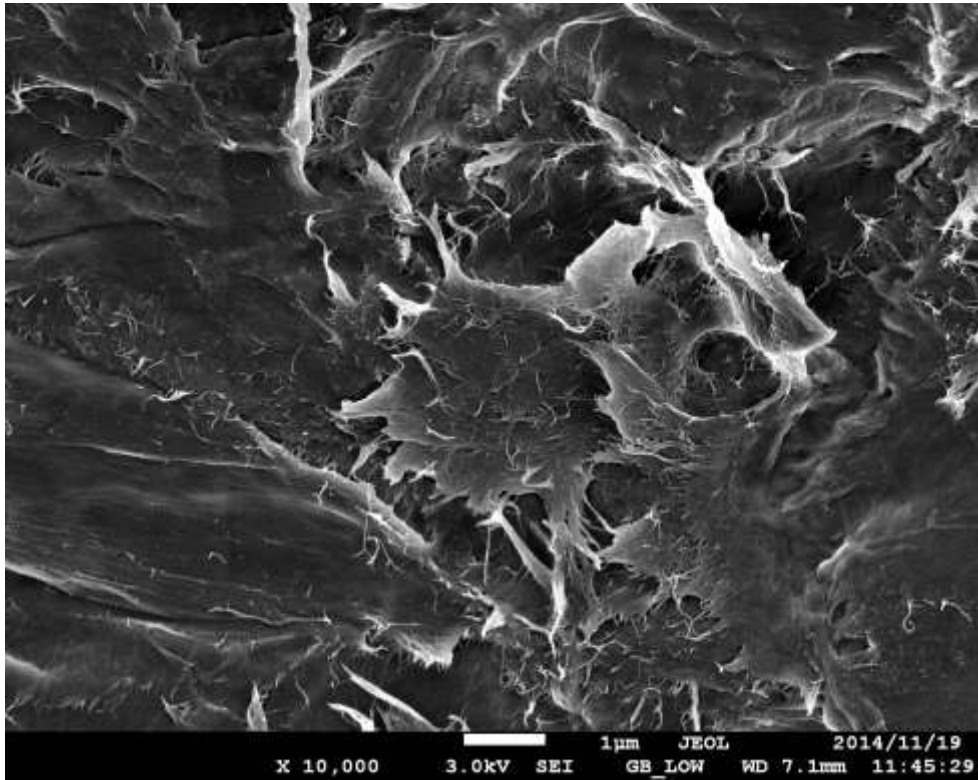


Figure 5.27 Pulped bagasse SEM micrograph at x10 k magnification

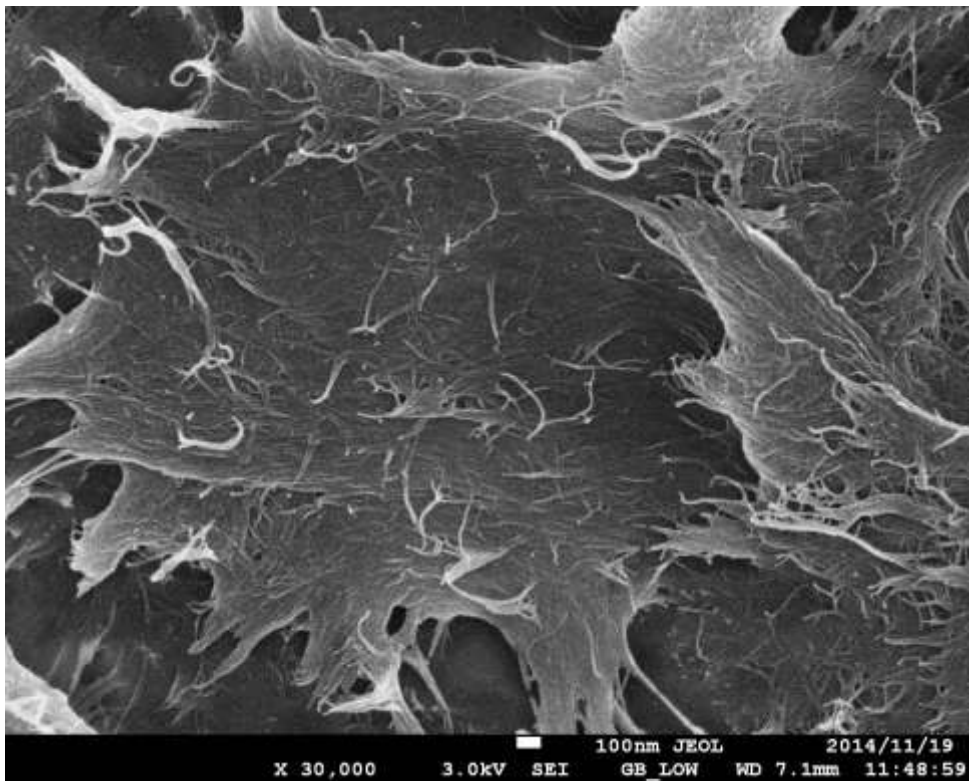


Figure 5.28 Pulped bagasse SEM micrograph at x30k magnification

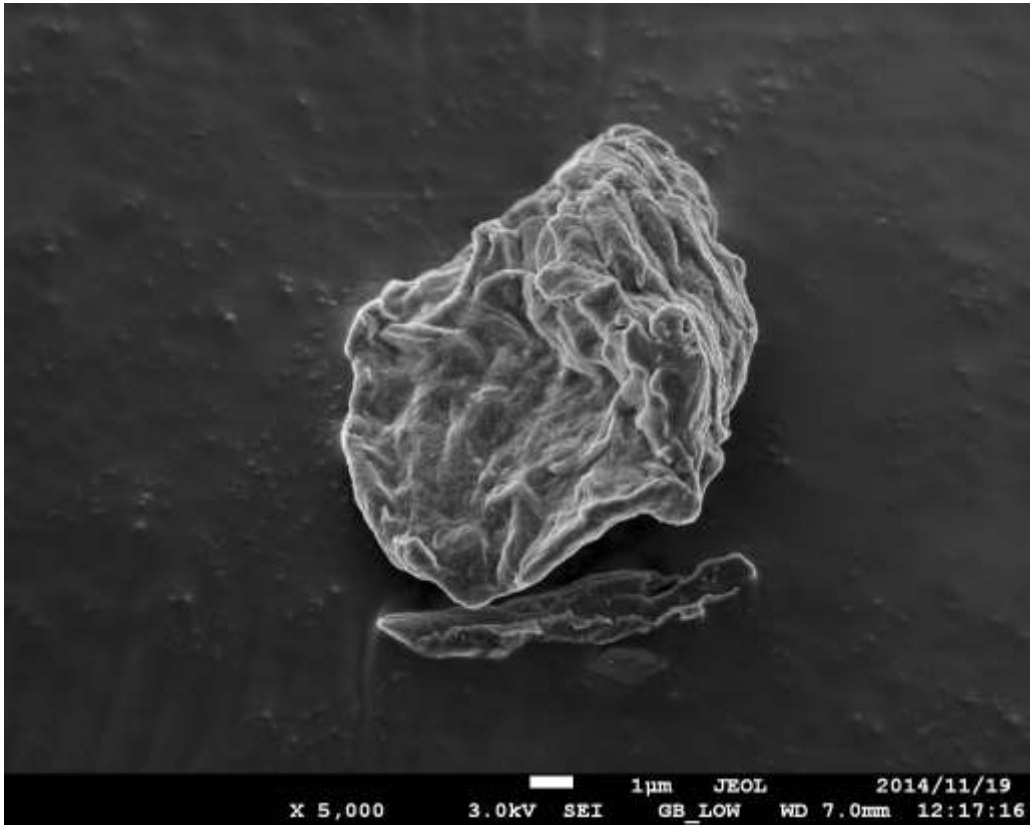


Figure 5.29 MCC SEM micrograph at x 5k magnification

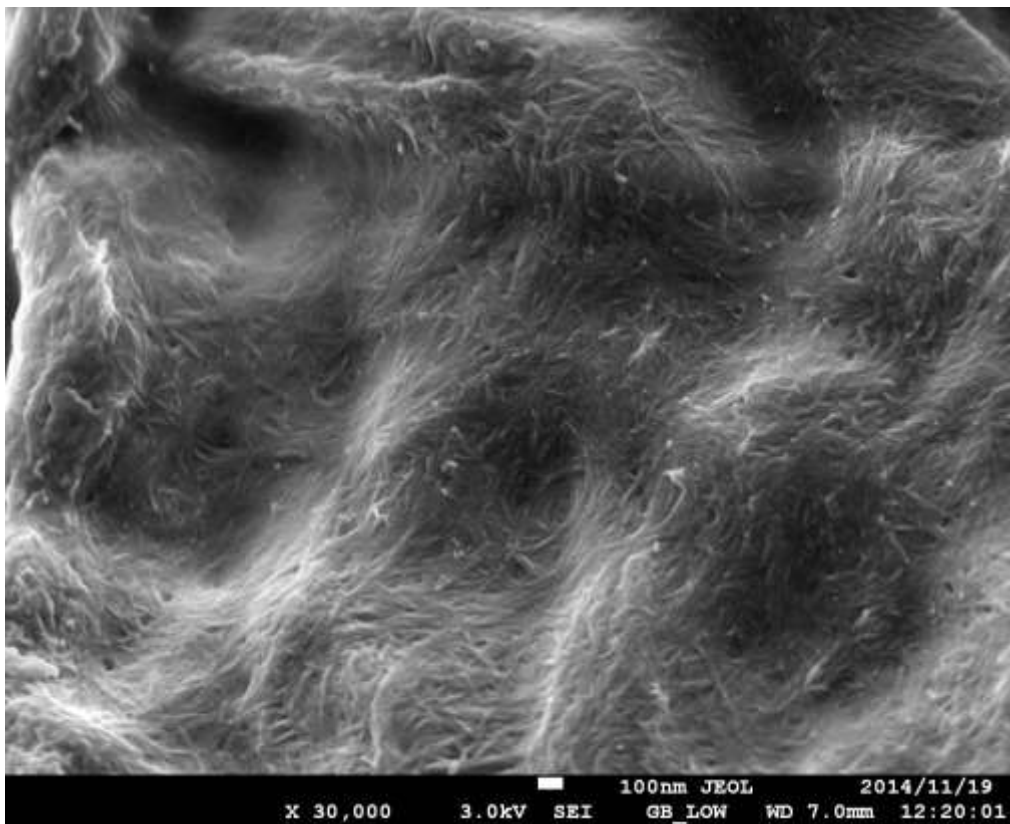


Figure 5.30 MCC SEM micrograph at x30k magnification

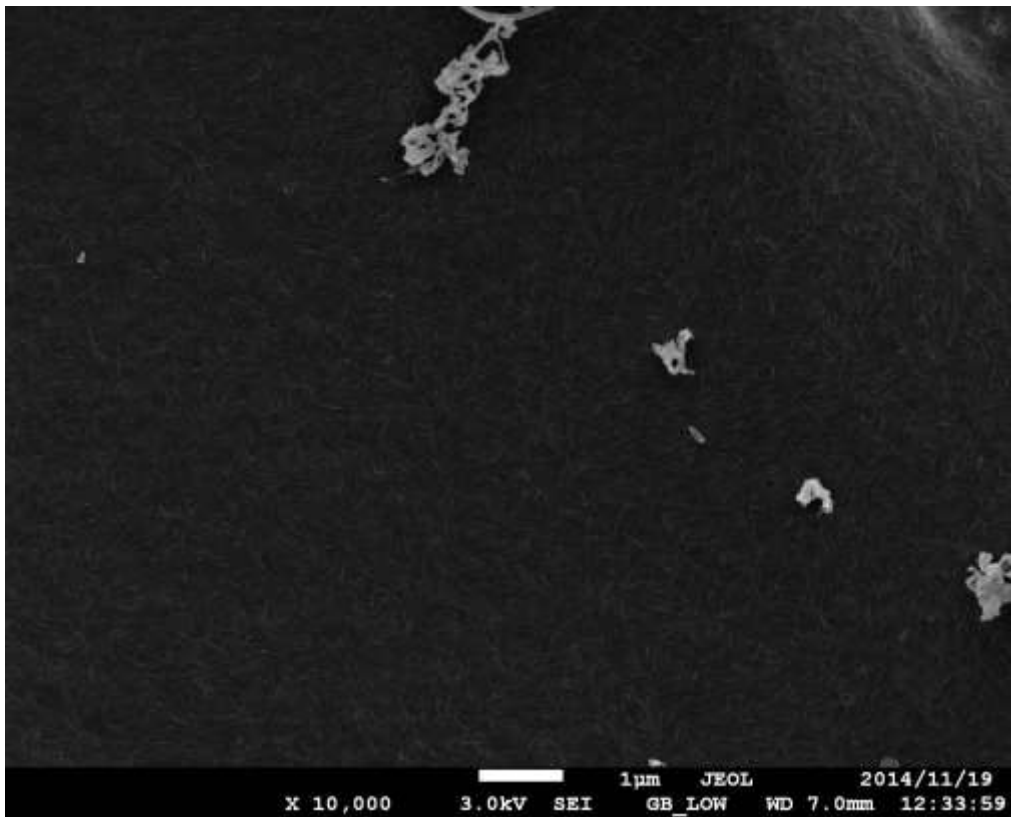


Figure 5.31 CNC SEM micrograph at x 10k magnification

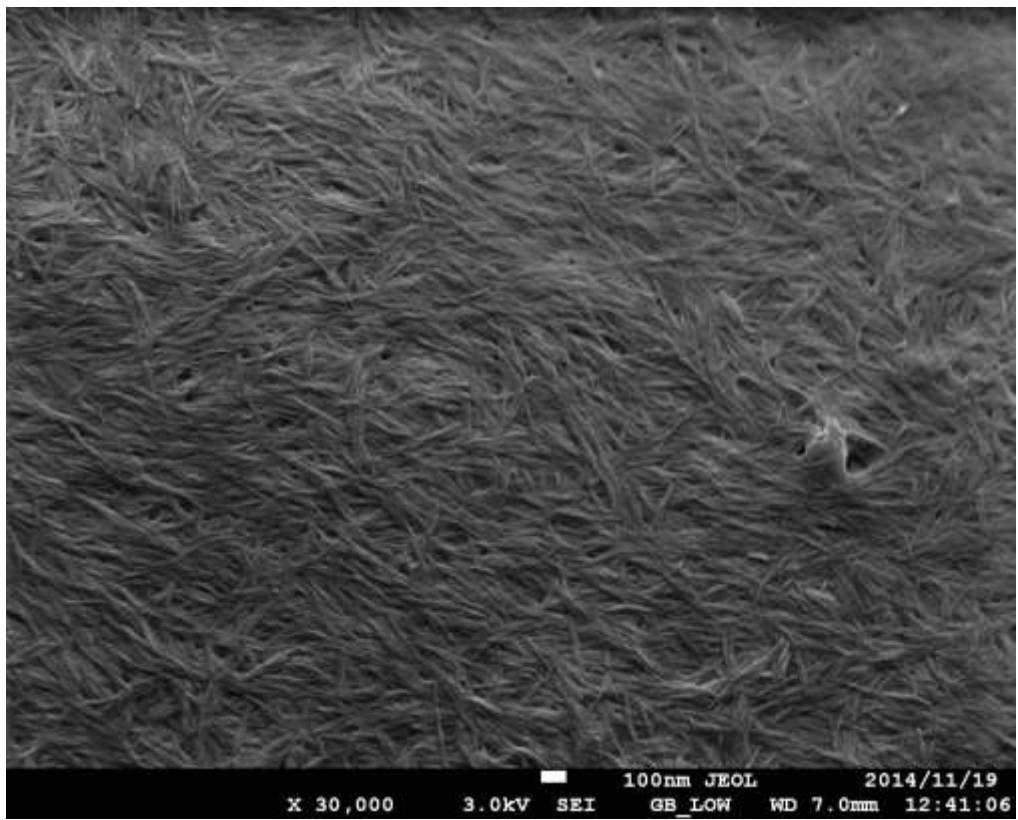


Figure 5.32 CNC SEM micrograph at x 30k magnification

5.7 Transmission Electron Microscopy

The following figures, Figure 5.32 – 5.34 show the experimental results obtained during the transmission electron microscopy analysis of CNCs produced by the acid hydrolysis.

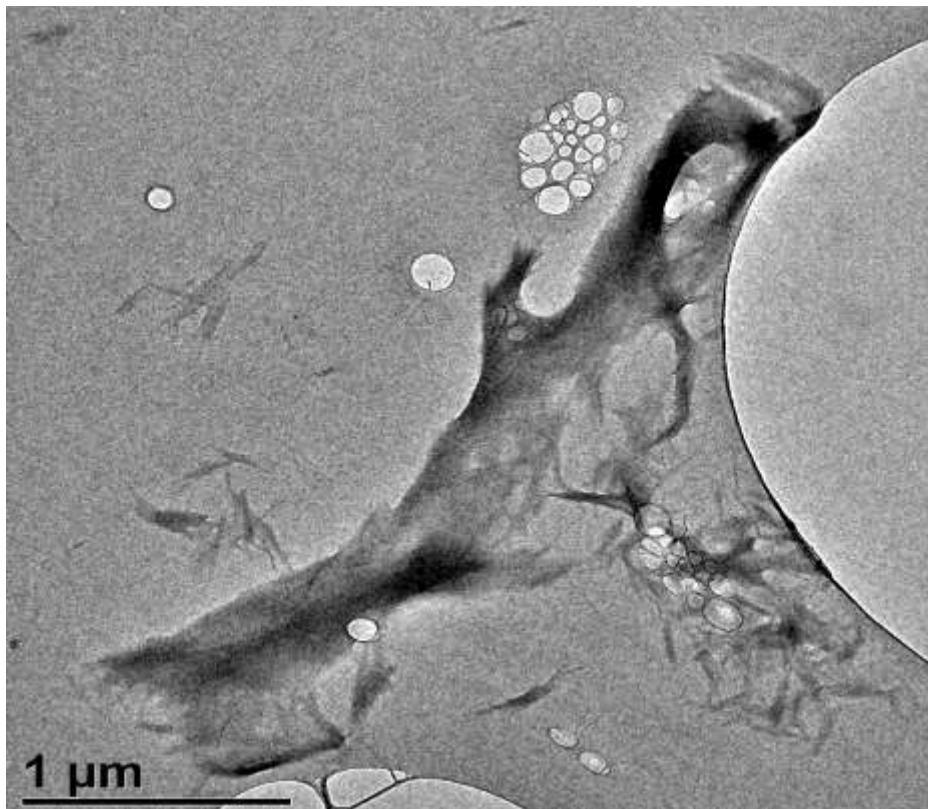


Figure 5.33 CNC TEM micrograph showing agglomerated crystals deposited on carbon substrate

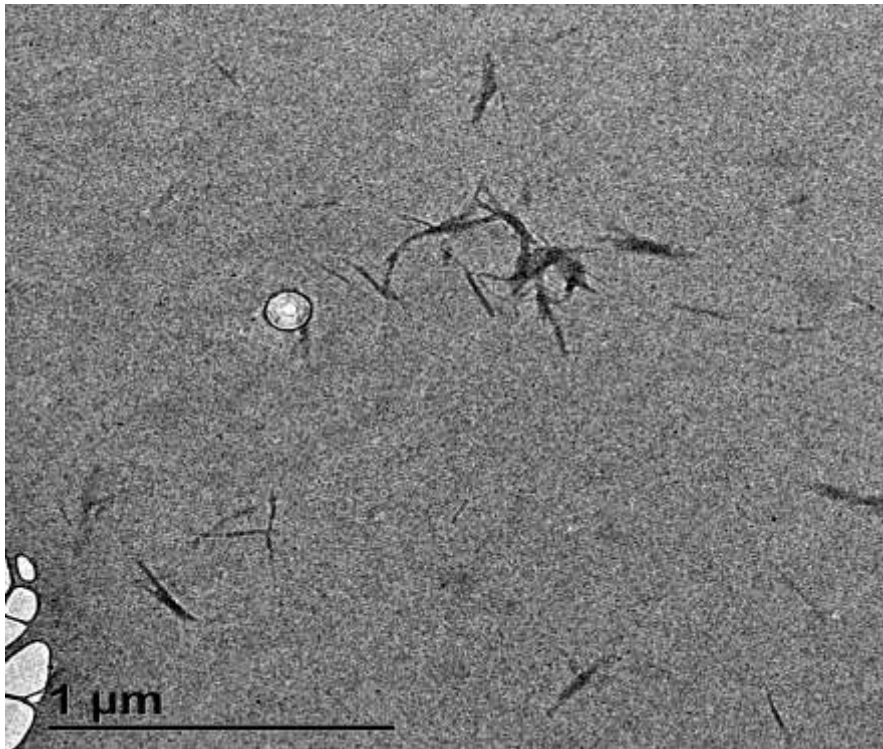


Figure 5.34 CNC TEM micrograph showing sonicated individual crystals

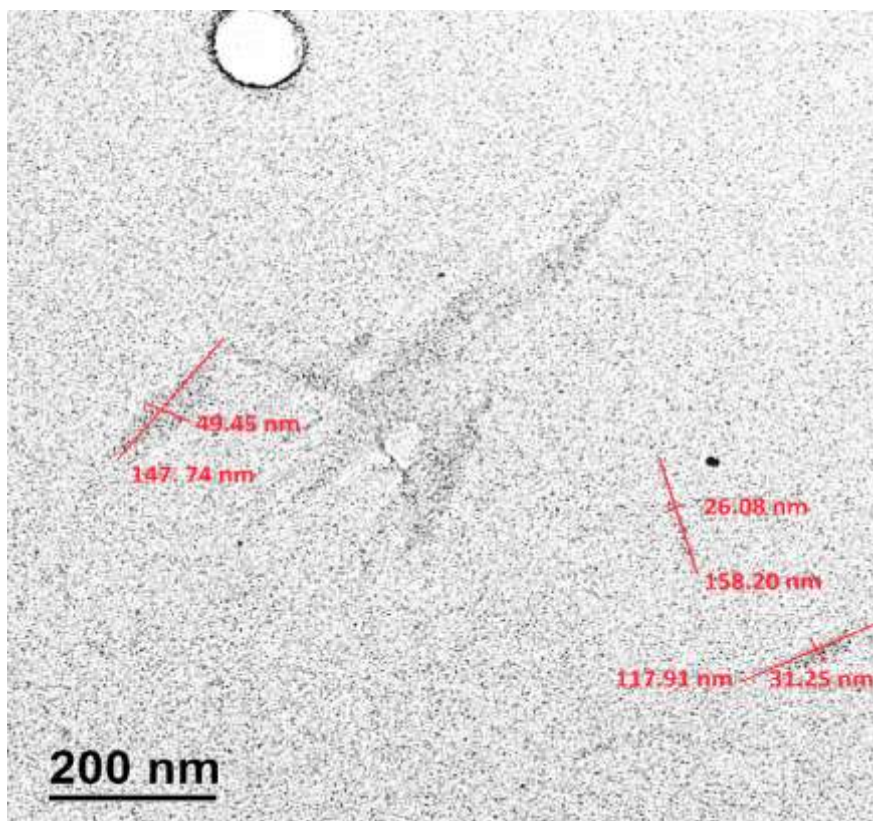


Figure 5.35 CNC TEM micrograph showing individual crystal dimensions

DISCUSSION

6.1 Dynamic Light Scattering

Figures 5.1 and 5.2 show the particle size (volume) percent and particle number results respectively for the prepared CNC solution.

Both figures 5.1 and 5.2 show a homogenous distribution of the particle volume and number over the illustrated ranges. The CNC distribution presented “bell” shaped unimodal distribution. The shape of the distribution suggested that both the CNC particle size (volume) and the CNC particle number were from one group of the isolated nanocrystals. The distribution range of the diameter of the CNC particles with reference to the volume data acquired was between 66 nm and 1.98 μm . The CNC volume data shows that diameter of the smallest particle of the prepared nanocrystals is 66nm which is accountable for 0.07 % of the volume fraction. The CNC volume data also shows that 72.63 % of the nanoparticles prepared had a diameter equal to or less than 445.1 nm. The median and mode for the volume data is 321.3 and 318.3 nm respectively. The distribution peaked at 318.3 nm which had 39% of the volume fraction. This was the most common particle size determined. The CNC volume median meant that half of the population of the prepared nanocrystals were above 321.3 nm and half were below this point.

The distribution curve for the CNC volume number in Figure 5.1 showed that all the nanocrystals produced were in the nanometre range. The particle number distribution mode or peak was at 108.4 nm and then decreased with increasing size of the prepared

cellulose nanoparticles. The largest particle size group was found to be 669nm in diameter which accounted for less than 0.15 % of the particles. 12, 3 % of the particles number distribution belonged to particles 115 nm in diameter. The median of the CNC number data was 157.3 nm.

A direct comparison of the CNC volume and CNC data is given in Figure 5.3. The figure clearly shows the CNC volume distribution in red and the CNC number distribution in black. The CNC number data illustrates the population of particles which have a certain size. For example, 72.63 % of the nanoparticles prepared had a diameter equal to or less than 445.1 nm. The CNC volume data illustrates the population of particles with a certain volume. For example, the largest particle size group was found to be 669nm in diameter which accounted for less than 0.15 % of the particles. When viewing the comparison, it is evident that the larger particles are responsible for the majority of the particle mass or volume.

The MCC volume data is represented by Figure 5.4, the MCC number data by Figure 5.5 and a comparison of the MCC volume and number data by Figure 5.6. The MCC volume data gave a bimodal curve implying that the size of the particles separated as MCC belonged to 2 major size groups. The size groups were in the nanorange and also in the microrange. The smallest particles as measured during the MCC volume measurements had a diameter not greater than 150.3 nm and represented 0.085 % of the volume population. The first mode or most common particle size group in the nanorange was 388.6 nm. These particles were responsible for 5.8 % of the volume population. The nanoparticles had diameter less than 877.3 nm and were responsible for 41.96 % of the volume population.

The second mode in the MCC volume data was in the microrange. These were particles with a diameter not greater than 4.472 μm and were as a group responsible for 8.61 % of the volume population. The particles which were in the microrange had diameters ranging from 1.005 – 6.000 μm . These particles collectively had a volume population equal to 58.04 %.

The MCC number average data gave a unimodal distribution as can be seen in Figure 5.5. This number distribution showed that the particles in the MCC residue had a mode in the nanorange, equal to 243.6 nm. The median for the MCC number data was 236.0 nm. This unimodal “bell“ shaped curve suggested a uniform or homogenous distribution of the particles over the illustrated range.

Comparing the MCC volume data and MCC number data, Figure 5.6, it can be seen that most of the particles were in the nanorange. This shows that the hydrolysis of pulped bagasse to CNC was effective.

6.2 Attenuated Total Reflectance Fourier Transform Infrared Spectroscopy

Figures 5.15 – 5.18 show the ATR FTIR spectra of pulped bagasse, FD CNC, MCC and the combined spectra respectively. The combined spectra is a comparison of the first three spectra. The spectra were scanned from 4000 cm^{-1} to 500 cm^{-1} . The broad transmission band between 3500-3200 cm^{-1} for all spectra corresponds to the O-H stretching vibration of the hydroxyl groups in cellulose, hemicellulose and lignin. (M. Sain 2006; Yang *et al.* 2007; Mandal and Chakrabarty 2011; Li *et al.* 2012; Lu and Hsieh 2012a; Kumar *et al.* 2013; Maiti *et al.* 2013; Rosli, Ahmad and Abdula 2013; R.

Maryana 2014). The presence of this band is also a result of the absorbed moisture in the pulped bagasse and MCC samples. The characteristic band at 2891 cm^{-1} in all spectra corresponds to the C-H stretching vibration of alkyl groups in aliphatic bonds of cellulose, lignin and hemicellulose.(De-Rosa *et al.* 2010; Lu and Hsieh 2012a; Rosli, Ahmad and Abdula 2013; Li *et al.* 2014; R. Maryana 2014). A decrease and change in the intensity and shape of this band respectively was observed in the combined spectra of pulped bagasse, CNC and MCC. A similar trend depicting the change in intensity and shape of this band was observed in literature references (Santos *et al.* 2013; Silvério *et al.* 2013). The band between $1700 - 1650\text{ cm}^{-1}$ corresponds to the C=O stretching vibration of the acetyl and uronic ester groups, from pectin, hemicellulose or the ester linkage of carboxylic group of ferulic and p-coumaric acids of lignin and/or hemicellulose (Garside and Wyeth 2003; M. Sain 2006; Zhao *et al.* 2010; Abraham *et al.* 2011; Rosli, Ahmad and Abdula 2013). Acid hydrolysis which is essential in the isolation of CNC from pulped bagasse removes the hemicelluloses and lignin from pulped bagasse, thus this peak is reduced in intensity in the spectrum of CNC.

A band positioned around 1640 cm^{-1} corresponds to the O-H bending of water absorbed into cellulose fibre structure and is present in all samples (Zhao *et al.* 2010; Lu and Hsieh 2012a; Yu *et al.* 2012). The bands located at 1500 cm^{-1} and around 1400 cm^{-1} are associated with the aromatic C=C in plane symmetrical stretching vibration of aromatic ring present in lignin (Zhao *et al.* 2010; Mandal and Chakrabarty 2011). The peak at 1245 cm^{-1} as present only in spectra of pulped bagasse corresponds to the C-O out of plane stretching vibration of the aryl group in lignin (Pandey *et al.* 2000; Sun *et al.* 2004; Rosli, Ahmad and Abdula 2013). FTIR spectra of FD CNCs have sharp bands but similar to that observed in the spectra of pulped bagasse and MCC. The bands at

1430-1420 cm^{-1} are due to CH_2 scissoring vibrating motion in cellulose (Sun *et al.* 2004; Spiridon, Teaca and Bodirlau 2011), 1382-1375 cm^{-1} (C-H bending), 1336 cm^{-1} (O-H in plane bending), 1317 cm^{-1} (CH_2 wagging), 1054 cm^{-1} (C–O–C pyranose ring stretching vibration), 902-893 cm^{-1} (associated with the cellulosic β -glycosidic linkages), around 1150 cm^{-1} (C–C ring stretching band), and at 1105 cm^{-1} (the C–O–C glycosidic ether band) (Wyman 1999; Pandey *et al.* 2000). The band at 895 cm^{-1} corresponds to cellulose (Dinand *et al.* 2002; Spiridon, Teaca and Bodirlau 2011) and an increase in the absorbance of this band corresponds with removal of amorphous cellulose and the increased availability of the crystallite portion of the crystalline cellulose polymer (Hubbe *et al.* 2008).

The table below lists all FTIR bands observed in the ATR-FTIR spectra of pulped bagasse, MCC and FD CNC.

Sr. No.	Frequency (cm^{-1})	Corresponding to
1	895	cellulose
2	1045	C–O–C pyranose ring stretching vibration
3	1105	C–O–C glycosidic ether band
4	1150	C–C ring stretching band
5	1245	C–O out of plane stretching vibration of the aryl group in lignin
6	1317	CH_2 wagging
7	1336	O-H in plane bending
8	1640	the O-H bending of water
9	2891	C-H stretching vibration of alkyl groups in aliphatic bonds
10	1382-1375	C-H bending
	1430-1420	CH_2 scissoring vibrating motion in cellulose
12	1500 and 1400	aromatic C=C in plane symmetrical stretching vibration of aromatic ring

13	1700 – 1650	C=O stretching vibration of the acetyl and uronic ester groups, from pectin, hemicellulose or the ester linkage of carboxylic group of ferulic and p-coumaric acids of lignin and/or hemicellulose
14	3500-3200	O-H stretching vibration of the hydroxyl groups in cellulose, hemicellulose and lignin
15	902-893	cellulosic β -glycosidic linkages

Table 6.1 FTIR bands observed during the ATR-FTIR analysis

The crystallinity of the samples can be calculated from the IR bands located between 1500 – 850 cm^{-1} (Dinand *et al.* 2002; N. Lin 2012). This only applies to samples containing crystalline cellulose, the amorphous cellulose or a mixture of amorphous and crystalline cellulose (Hurtubise and Krasig 1960). The above mentioned IR region is sensitive to crystal structure of the cellulosic material. Spectral bands at 1420-1430 cm^{-1} and 893-897 cm^{-1} are very important to explain the crystal structure of cellulosic material (Sun *et al.* 2005). The following ratios show how the Lateral Orientation index (LOI) and the Total Crystallinity Index (TCI) are calculated using IR ratios. The ratio for each sample was calculated using the corresponding FTIR spectrum.

$$\text{Lateral Orientation Index (LOI)} = \frac{1430\text{cm}^{-1}}{890\text{cm}^{-1}} \quad \text{Equation 1}$$

(Hurtubise and Krasig 1960)

Equation 1 Lateral Orientation Index calculated using IR ratios.

$$\text{Total Crystallinity Index (TCI)} = \frac{1375\text{cm}^{-1}}{2900\text{cm}^{-1}} \quad \text{Equation 2}$$

(O'Connor 1960)

Equation 2 Total Crystallinity Index calculated using IR ratios.

An increase in both LOI and TCI ratios was observed from pulped bagasse to MCC to CNC as can be seen in in Table 3. An increase in these ratios corresponds to the formation of ordered crystallites within the samples. Higher value of the given index (LOI, TCI) reveals that the given material contains a highly crystalline and ordered structure. This can be attributed to the removal of amorphous cellulose during the pulping of the sugarcane bagasse and also during the acid hydrolysis. This separates the amorphous cellulose from the cellulose crystallites to form the nanocrystals. The table below shows the values of TCI and LOI as calculated using equations 1 and 2.

	TCI	LOI
Pulped Bagasse	0.99	0.962
MCC	1.10	1.231
FD CNC	1.06	1.245

Table 6.2 The TCI and LOI indices calculated using FTIR transmission bands

6.3 Wide Angle X-Ray Diffraction

The peaks observed during the WAXRD are given in the table below

Sr. No.	(2 θ Angle)	d-spacing (Å)
1	15	1 1 0
2	22.5	2 0 0
3	35	0 0 4

Table 6.3 The XRD peaks and their corresponding 2 θ angles.

Wide angle X-Ray Diffraction analysis was performed on pulped bagasse, FD CNC and MCC. The corresponding XRD diffractograms are given in Figures 5.19 – 5.22. Figure 5.22 shows the combined XRD diffractograms for all three samples. Figure 5.19 shows the XRD diffractogram for pulped bagasse. The figure shows characteristic cellulose peaks around $2\theta = 15$ and 22.5° . The XRD profiles are similar suggesting that all three samples contain cellulose. Along with the small shift in the peak positions seen for FD CNC and MCC. There was also a change in the relative intensity with respect to the amorphous peaks and the width of peaks, which indicates a deviation in the crystallinity.

6.3.1 Crystallinity Index

The determination of cellulose crystallinity has always been difficult. Various methods have been devised for the calculation of the crystallinity index (CrI) (Segal *et al.* 1959), however, due to its simplicity the following method to determine the crystallinity index has been widely used.

$$CrI = \frac{I_{200} - I_{am}}{I_{200}} \times 100 \quad \text{Equation 3}$$

(Segal *et al.* 1959)

Equation 3 Percent Crystallinity calculated using XRD intensities.

The intensity of the fitted peak, obtained as after removing background and determination of peaks from crystalline and non-crystalline regions, corresponding to the 200 plane and 1 1 0 plane for the amorphous region were used to calculate the crystallinity index.

An increase in crystallinity index was observed from pulped bagasse to MCC to CNC. It can be seen from diffractograms that the fibres show increasing crystalline orientation along a certain axis after subsequent treatment as the non-cellulosic amorphous polysaccharides are removed and the highly crystalline cellulose is left. All three diffractograms display two well-defined peaks around $2\theta = 15.5^\circ$ (for 1 1 0 plane) and $2\theta = 22.5^\circ$ (for 2 0 0 plane). These two planes are characteristic of cellulose (Segal *et al.* 1959; Zhao *et al.* 2010; Liu *et al.* 2011; Sheltami *et al.* 2012).

The final increase in percent crystallinity was due to the acid hydrolysis. Literature references (Lu and Hsieh 2012a; Ponce-Reyes *et al.* 2014; Reddy and Rhim 2014) show CrI values of 39,%, 54,9 % and 63,0 % when calculating for the percent crystallinity index. The CrI obtained in this study was found to be 46, 3%. The results of the XRD analysis corroborated with those from the FTIR studies which also show an increase in the crystallinity indices. Literature references (Mandal and Chakrabarty 2011; Kumar *et al.* 2013) who used sugarcane bagasse as their source of cellulose fibres show a trend of increasing CrI values as the CNC are isolated from the bagasse. The value for the CrI for CNCs as obtained from the study performed by A. Kumar (Kumar *et al.* 2013) was 72.5 %. Table 4 shows the CrI values of CNC isolated from various lignocellulosic sources in recent years.

The table below shows the different values from literature for the CrI of CNCs isolated from different sources.

Source	Hydrolysis Time	Year	% CrI	Length (nm)	Width (nm)	Literature Reference
Sugarcane Bagasse	300 min	2011	*	170	35	(Mandal and Chakrabarty 2011)
Microcrystalline Powder	180 min	2011	*	60 - 120	6 - 8	(Liu <i>et al.</i> 2011)
Banana Leaves	**	2011	83.3	5- 50	*	(Abraham <i>et al.</i> 2011)
Jute leaves	**		88.6	15 - 25	*	
Pineapple leaves	**		89.3	5 - 50	*	
Sugarcane Bagasse	30 min	2011	87.5	255 ± 55	4 ± 2	(Teixeira <i>et al.</i> 2011)
	75 min		70.5		8 ± 3	
Bamboo	30 min	2012	72.0	200 - 500	>20	(Yu <i>et al.</i> 2012)
Chardonnay grape skins	300 min	2012	54.9	10 - 100	30 - 65	(Lu and Hsieh 2012a)
Rice straw	30 min	2012	86.0	50 - 700	10 - 65	(Lu and Hsieh 2012b)
	45 min		91.2	117	11.2	
Mengkuang leaves (Pandanus tectorius)	45 min	2012	54.5	<200	<30	(Sheltami <i>et al.</i> 2012)
Sugarcane Bagasse	60 min	2014	35.6	250 - 480	20 - 60	(Kumar <i>et al.</i> 2013)
Corn Cob	30 min	2013	79.8	287.3 ± 75.5	4.90 ± 1.34	(Silvério <i>et al.</i> 2013)
	60 min		83.7	210.8 ± 44.2	4.15 ± 1.08	
	90 min		78.0	195.9 ± 45.9	4.03 ± 1.07	
Agave angustifolia Fibre	45 min	2013	82.0	170 - 500	8 - 15	(Rosli, Ahmad and Abdula 2013)
Agave atrovirens parenchymatous	180 min	2014	39.4	198 – 310	97 ± 30	(Ponce-Reyes <i>et al.</i> 2014)
spruce bark	60 min	2014	84.0	175.3 ± 61.8	2.8 ± 0.8	(Normand, Moriana and Ek 2014)
oil palm empty fruit bunch (OPEFB)	60 min	2014	84.0	>100	<10	(Haafiz <i>et al.</i> 2014)
Sugar beet pulp (SBP)	**	2014	77.98	*	<10 - 70	(Li <i>et al.</i> 2014)

* Not reported

** Mechanical isolation

Table 6.4 The CrI indices of CNC prepared and isolated in recent years.

6.4 Thermogravimetric Analysis and Differential Thermogravimetry

Figures 5.11 shows the combined TGA profiles of pulped bagasse, MCC and FD CNC.

Figures 5.12 – 5.14 show the individual TGA profiles of pulped bagasse, MCC and FD CNC respectively. All the TGA profiles were collected between 25 °C - 600 °C with a heating ramp of 10 °C under nitrogen purge.

The TGA curves in Figure 19 showed three degradation steps related to moisture evaporation, hemicellulose, cellulose and lignin degradation. From the TGA curves above it is clear to see that from 25 -120 °C there is a slight decrease in the mass of all samples. This is due to the removal of surface bound moisture on the samples being removed. The degradation onset temperature of pulped bagasse (Figure 5.12) was the lowest at 190 °C due to a higher content of lignin and hemicellulose. After the initial mass loss of about 10% due to moisture content, the degradation of pulped bagasse was a multi stage degradation starting at 190 - 270 °C. This degradation was responsible for about 30% of the total mass loss of the sample. The DTG curve of pulped bagasse (Figure 5.14) exhibited two prominent peaks at 210 °C and at 320 °C. The two peaks are for the amorphous and crystalline cellulose respectively. The second step in the thermal degradation of pulped bagasse (Figure 5.12) was between 250 -325 °C. This accounted for 25 % of the total weight loss. The final step was accountable for 32% of the mass loss of sample. FD CNC (Figure 5.14) exhibited a degradation profile wherein the onset temperature was higher than that of pulped bagasse. The onset degradation temperature of FD CNC as per the (Figure 5.14) was about 250 °C. This was corroborated by Figure 5.13 which shows a shoulder on the peak of the CNC. This shoulder, observed in the DTG curve, at around 300 °C likely reflects the presence of a portion of the hemicellulose (Sheltami *et al.* 2012). Crystalline cellulose has a much ordered structure making it more thermally stable. The FD CNC (Figure 5.14) were of higher purity and hence exhibited a smoother curve when subjected to similar degradation conditions. After the initial mass loss between 25 -120 °C due to the loss of surface bonded moisture, FD CNC started degrading at around 260 °C peaking at 310 °C. The lower degradation onset temperature of pulped bagasse compared to that

of FD CNC is due to the presence of lignin, hemicelluloses and other non-cellulosic segment which decompose at low temperature (Kumar *et al.* 2013).

6.5 Atomic Force Microscopy

Atomic force microscopy (AFM) is a relatively inexpensive technique that does not require more elaborate sample preparation and it produces a three-dimensional image (Edgar 2002). AFM gives clear indication of the size of nanoparticles being measured along the x-y planes. It also gives a clear distinction of the height of particles being measured along the z-axis. A problem that arises from AFM analysis is related to tip-sample convolution. The physical probe used in AFM imaging is not ideally sharp. As a consequence, an AFM image does not reflect the true sample topography, but rather represents the interaction of the probe with the sample surface (R. Wilson 2006). This is called tip convolution. Figure below shows how tip convolution occurs during AFM measurements.

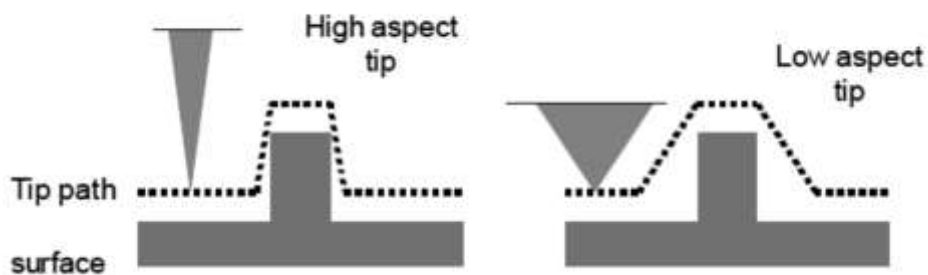


Figure 6.1 How tips with different aspect ratios are used to overcome tip convolution in AFM measurements

Adapted from literature reference (R. Wilson 2006)

Figures Figure 5.22 – 5.25 show the AFM micrographs of CNC. Figure 5.23 shows the 3D AFM micrograph of CNC. From this 3D image, it is clear to see that the CNCs were

evenly distributed during the AFM measurement. From the 3D micrograph the length of the CNCs ranges between 300 – 400 nm. The width of the crystals as measure from the 3D micrograph ranges between 10 – 30 nm. The exact dimensions of a single crystals is very difficult to discern due to the agglomeration of the nanoparticles. The agglomeration occurs during drying of the sample during sample preparation.

Figure 5.24 shows the height micrograph of a dilute aqueous CNC. The maximum height of all the measured CNC from the micrograph is between 25 – 35 nm. This measured height of the CNCs is in agreement with the diameters measured from the 3D micrograph in Figure 5.23. Literature reference (Boluka *et al.* 2011) used AFM to characterize CNCs and found dimensions of 100 – 300 nm in length and 4 – 8 nm in diameter.

Figures 5.25 and 5.26 show the phase micrograph of the dilute solution of CNC. The micrographs show an even distribution of the CNC. Agglomeration due to drying during sample preparation their high specific area and the strong hydrogen bonds established between the crystallites(Normand, Moriana and Ek 2014) causes the CNC to attract and hence the difficulty to measure single crystal dimensions. Table 1 lists CNC prepared from different sources and crystal dimensions measured using AFM and other techniques.

6.6 Scanning Electron Microscopy

Figures 5.27 – 5.32 show the SEM micrographs of pulped bagasse, MCC and FD CNC at different magnifications. Figure 5.27 shows the SEM micrograph of pulped bagasse at x10 k magnification and Figure 5.28 the pulped bagasse at x30 k magnification. SEM is a good tool to investigate the morphological changes the pulped bagasse. From compositional analysis (Rainey 2009) the pulp contains cellulose fibres still bound by

lignin and hemicellulose. The fibres are not orientated in a specific fibre axis direction. The soda pulping method used to pulp the bagasse loosens the fibres to a certain extent allowing for easier acid hydrolysis. At this stage the fibres are bound by acid soluble lignin and hemicellulose. This is visible in Figure 5.30 which shows MCC, the hydrolysis residue, with cellulose fibres clearly visible and in a more ordered orientation than in Figures 5.27 and 5.28. Partial acid hydrolysis yields the microcrystalline fibres which have a reduced diameter. Figure 5.29 shows the reduced fibres still bound by acid soluble components of biomass. Size reduction to the nanometre range Figure 5.31 – 5.32 is achieved by the prolonged hydrolysis which completely removes the amorphous cellulose and yields the nanocrystals with no apparent defect. The CNC are seen as an agglomeration of rod-like crystals with heterogeneous sizes. From the pulped bagasse to the microcrystalline bagasse to the nanocrystals, it is evident that the acid hydrolysis was effective in removing the amorphous celluloses and reducing the fibre dimension. The nanocrystals have a high aspect ratio with lengths in the 250-350nm range.

6.7 Transmission Electron Microscopy

Figures 5.33 – 5.35 show the TEM micrographs of agglomerated CNC on carbon substrate, sonicated individual CNCs and individual crystal dimensions respectively. Figure 44 shows the agglomeration of the CNC due to drying as a result of sample preparation. The attraction is due to the interactions of the abundant hydroxyl groups on the surface area of the crystals. The “air bubble” visible in Figure 5.33 is as a result of the holey carbon used as a substrate. Non conducting crystalline nanostructured are viewed best if placed on a carbon substrate supported by a copper grid. The

agglomerated crystals in Figure 5.33 as shown below form crystal clusters but individual crystals are obtainable through ultrasonication. The circles in the enlarged Figure 5.33 below show individual crystals which were separated and did not agglomerate after sonication. These individual crystals were used to determine the dimensions of the prepared crystals. The circled CNC are less than 300 nm in length and less than 20 nm in length.

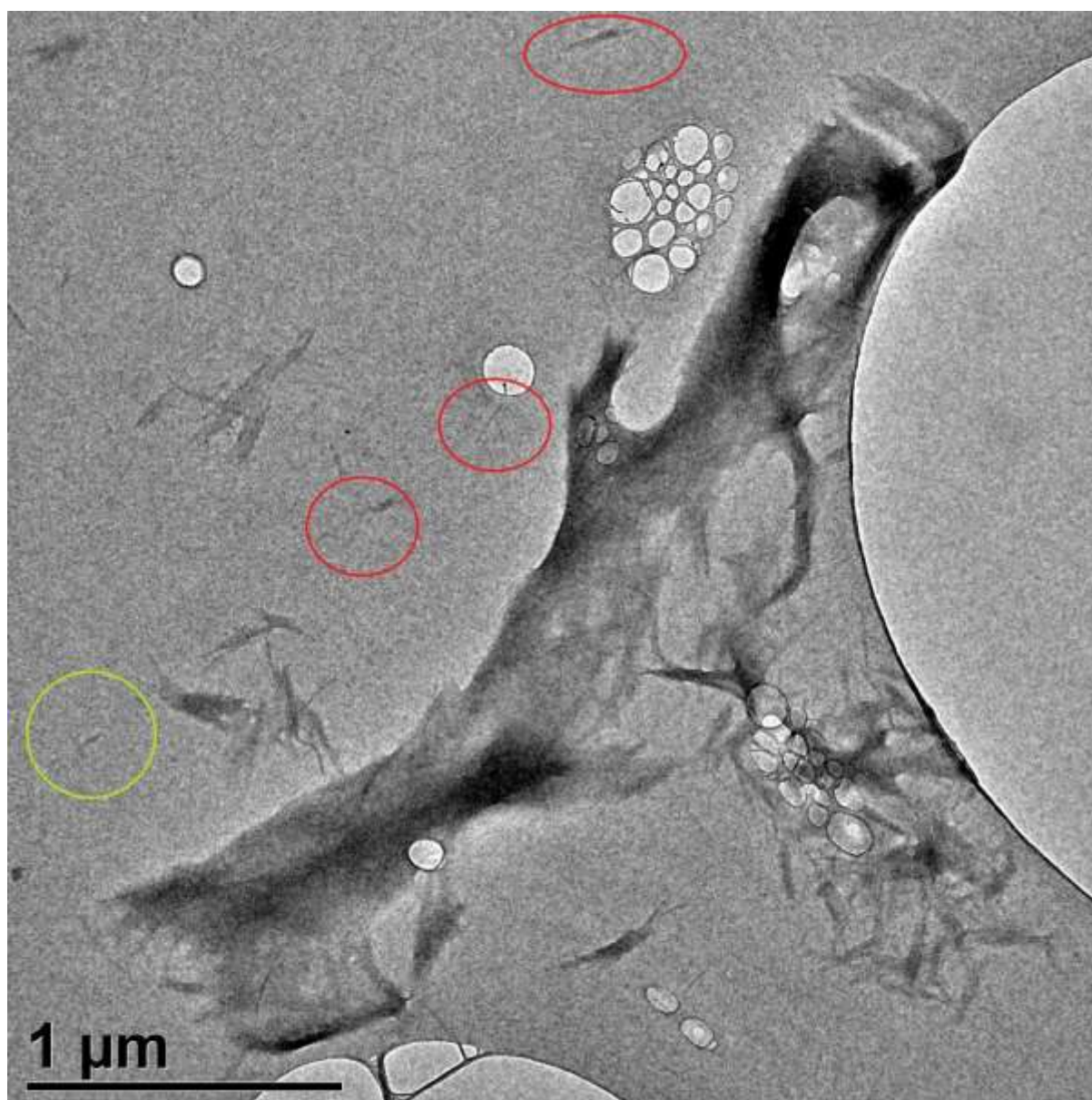


Figure 6.2 Magnified image of TEM micrograph (Figure 5.33)

Figure 6.2 shows the TEM micrograph of dispersed and individual CNCs. The dispersion was as a result of extended ultrasonication which assists in preventing agglomeration. The micrograph shows individual CNCs all below 300 nm in length and less than 30nm in diameter. These dimensions were measured more accurately using software in the instruments and the values reported in Figure 5.35. Figure 5.35 shows the TEM micrograph of CNCs with measured dimensions. The dimensions of the measured crystals are in nm (length x width) 147.74 x 49.45, 158.20 x 49.45 and 117.91 x 3125. All these measurements agree with the particle size determination which stated that the majority 72.63 % of the CNC were below 445.1 nm. Figure 44 clearly showed that the CNCs prepared were in the shape of needle like rods.

CONCLUSION & RECOMMENDATIONS

The aim of this study was to demonstrate the viability of the preparation of CNCs from soda pulped bagasse and to characterize the prepared CNCs using a wide range of analytical and imaging techniques. It is hoped that this study will drive further interest in the preparation of CNCs from renewable biomass sources and agro waste products.

The CNCs were prepared using the acid hydrolysis technique. Acid hydrolysis is the most popular and efficient method of isolating CNCs from biomass. The CNC solution was a milky white stable suspension of needle shaped nanocrystalline cellulose. The stability of the suspension was as a result of the surface anionic repulsive charges of the crystals. The TEM, SEM & AFM studies gave supporting evidence for the formation of nanocellulose. This observation was further been corroborated by given the DLS studies which indicate that majority of the acid hydrolysed particles lie in the nanorange. The crystallinity of the CNC depends is greatly affected by hydrolysis times. Extended hydrolysis times lead to partial degradation of the cellulose crystallites in the polymer. Extended hydrolysis times result in carbonation of the cellulose and the formation a brown discolouration of the solution. Different sources of cellulose require different hydrolysis times to reduce the size of the cellulose particles to the nanorange. These hydrolysis times can be can be greatly reduced by appropriate pre-treatment of the lignocellulosic biomass being used as starting material. Table 4 gives different hydrolysis times used during the isolation of CNC from different sources of biomass.

It is recommended that prior to acid hydrolysis extensive pre-treatment of biomass be performed in the aim of removing as much of the non-crystalline and non-cellulosic components of biomass as possible. This aids in reducing hydrolysis times and producing CNCs of uniform dimensions. Bleaching and alkaline pre-treatment is also recommended so as to aid in the removal of surface waxes and extractives.

Thorough rinses after each pre-treatment is strongly advised as traces of alkaline and bleaches interfere and neutralise the acid used during the hydrolysis procedure. Vigorous and constant agitation is also an important aspect to be noted during all treatments. This aids in ensuring homogeneity in the reaction vessels.

A well balanced and calibrated temperature monitoring device is needed to constantly monitor temperature changes. Unregulated temperatures result in temperature spikes and carbonation of the cellulose.

Research into grafting of CNCs is proposed as future work. This will entail functionalization of the surface hydroxyl groups of the CNCs with specific groups so as to induce functionality and then used as bio-composites in plastics and as reinforcing agents in other materials of interest.

REFERENCES

Abraham, E., Deepa, B., Pothan, L., Jacob, M., Thomas, S., Cvelbar, U. and Anandjiwala, R. 2011. Extraction of nanocellulose fibrils from lignocellulosic fibres: A novel approach. *Carbohydrate Polymers*, 86 (1468– 1475)

Ahola, S., Österberg, M. and Laine, J. 2008. Cellulose nanofibrils—adsorption with poly(amideamine) epichlorohydrin studied by QCM-D and application as a paper strength additive. *Cellulose*, 15 (2): 303-314.

Andrade, M. and Colodette, J. 2014. Dissolving Pulp Production from Sugarcane Bagasse. *Industrial Crops and Products*, 52: 58– 64.

Anglès, M. and Dufresne, A. 2000. Plasticized Starch/Tunicin Whiskers Nanocomposites. 1. Structural Analysis. *Macromolecules*, 33 (22): 8344–8353.

Araki, J. and Kuga, S. 2001. Effect of Trace Electrolyte on Liquid Crystal Type of Cellulose Microcrystals. *Langmuir*, 17 (15): 4493–4496.

Araki, J., Wada, M. and Kuga, S. 2001. Steric Stabilization of a Cellulose Microcrystal Suspension by Poly(ethylene glycol) Grafting. *Langmuir*, 17 (1): 21 - 27.

Araki, J., Wada, M., Kuga, S. and Okano, T. 1998. Flow properties of microcrystalline cellulose suspension prepared by acid treatment of native cellulose. *Colloids and Surfaces A: Physicochemical and Engineering Aspects*, 142 (1): 75–82.

Araki, J., Wada, M., Kuga, S. and Okano, T. 1999. Influence of surface charge on viscosity behavior of cellulose microcrystal suspension. *Journal of Wood Science*, 45 (3): 258-261.

Aulin, C., Gällstedt, M. and Lindström, T. 2010. Oxygen and oil barrier properties of microfibrillated cellulose films and coatings. *Cellulose*, 17 (3): 559-574.

Boluka, Y., Lahiji, R., Zhao, L. and McDermott, M. T. 2011. Suspension viscosities and shape parameter of cellulose nanocrystals (CNC). *Colloids and Surfaces A: Physicochemical and Engineering Aspects*, 377: 297–303.

Brinchi, L., Cotana, F., Fortunati, E. and Kenny, J. M. 2013. Production of nanocrystalline cellulose from lignocellulosic biomass: Technology and applications. *Carbohydrate Polymers*, 94: 154– 169.

Capadona, J., Shanmuganathan, K., Trittschuh, S., Seidel, S., Rowan, S. and Weder, C. 2009. Polymer Nanocomposites with Nanowhiskers Isolated from Microcrystalline Cellulose. *Biomacromolecules*, 10 (4): 712–716.

Chen, D., Lawton, D., Thompson, M. and Liu, Q. 2012. Biocomposites reinforced with cellulose nanocrystals derived from potato peel waste. *Carbohydrate Polymers*, 90: 709– 716.

College, C. 2015. *Geochemical Instrumentation and Analysis*. Available:

http://serc.carleton.edu/research_education/geochemsheets/techniques/XRD.html (Accessed

De-Rosa, I., Kenny, J., Puglia, D., Santulli, C. and Sarasini, F. 2010. Morphological, thermal and mechanical characterization of okra (*Abelmoschus esculentus*) fibres as potential reinforcement in polymer composites. *Composites Science and Technology*, 70: 116–122.

Dinand, E., Vignon, M., Chanzy, H. and Heux, L. 2002. Mercerization of primary wall cellulose and its implication for the conversion of cellulose I→cellulose II. *Cellulose*, 9 (1): 7-18.

Dong, H., Strawhecker, K., Snyder, J., Orlicki, J., Reiner, R. and Rudie, A. 2012. Cellulose nanocrystals as a reinforcing material for electrospun poly(methylmethacrylate) fibers: Formation, properties and nanomechanical characterization. *Carbohydrate Polymers*, 87: 2488– 2495.

Dong, X. M., Kimura, T., Revol, J. F. and Gray, D. G. 1996. Effects of Ionic Strength on the Isotropic–Chiral Nematic Phase Transition of Suspensions of Cellulose Crystallites. *Langmuir*, 12 (8): 2076–2082.

Edgar, C. D. 2002. Characterization of suspensions and films of cellulose nanocrystals. Doctor of Philosophy, McGill University.

Elazzouzi-Hafraoui, S., Nishiyama, Y., Putaux, J. L., Heux, L., Dubreuil, F. and Rochas, C. 2008. The Shape and Size Distribution of Crystalline Nanoparticles Prepared by Acid Hydrolysis of Native Cellulose. *Biomacromolecules*, 9 (1)

Eriksen, Ø., Syverud, K. and Gregersen, Ø. 2008. The use of microfibrillated cellulose produced from kraft pulp as strength enhancer in TMP paper. *Nordic Pulp and Paper Research Journal*, 23 (3): 299–304.

Espino, E., Cakir, M., Domenek, S., Román-Gutiérrez, A., Belgacem, N. and Bras, J. 2014. Isolation and Characterization of Cellulose Nanocrystals from Industrial by-products of Agave Tequilana and Barley. *Industrial Crops and Products*, 62: 552 - 559.

Fazli, F. A., Ehsani, M. R., Ghanbarzadeh, B. and Asadi, G. H. 2012. Nano Crystalline Cellulose Production and Its Application in Novel Food Packaging. In: *Proceedings of 2012 2nd International Conference on Environment Science and Biotechnology*. Kuala Lumpur, Malaysia, IACSIT Press, Singapore, 134-137.

Garside, P. and Wyeth, P. 2003. Identification of Cellulosic Fibres by FTIR Spectroscopy I: Thread and Single Fibre Analysis by Attenuated Total Reflectance. *Studies in Conservation*, 48 (4): 269 - 275.

Grunert, M. and Winter, W. 2002. Nanocomposites of Cellulose Acetate Butyrate Reinforced with Cellulose Nanocrystals. *Journal of Polymers and the Environment*, 10 (2): 27 - 30.

Haafiz, M., Hassana, A., Zakaria, Z. and Inuwa, I. 2014. Isolation and characterization of cellulose nanowhiskers from oilpalm biomass microcrystalline cellulose. *Carbohydrate Polymers*, 103: 119– 125.

Habibi, Y., Goffin, A.-L., Schiltz, N., E.Duquesne, Dubois, P. and Dufresne, A. 2008. Bionanocomposites based on poly(ϵ -caprolactone)-grafted cellulose nanocrystals by ring-opening polymerization. *Journal of Material Chemistry*, 18

Habibi, Y., Lucia, L. and Rojas, O. 2010. Cellulose Nanocrystals: Chemistry, Self-Assembly, and Applications. *Chemical Reviews*, 110 (6): 3479–3500.

Heux, L., Chauve, G. and Bonini, C. 2000. Nonflocculating and Chiral-Nematic Self-ordering of Cellulose Microcrystals Suspensions in Nonpolar Solvents. *Langmuir*, 16 (21): 8210–8212.

Hubbe, M., Rojas, O., Lucia, L. and Sain, M. 2008. Cellulosic Nanocomposites: A Review. *Bioresources*, 3 (3): 929 980.

Hurtubise, F. and Krasig, H. 1960. Classification of Fine Structural Characteristics in Cellulose by Infrared Spectroscopy. Use of Potassium Bromide Pellet Technique. *Analytical Chemistry*, 32 (2)

Kimura, F., Kimura, T., Tamura, M., Hirai, A., Ikuno, M. and Horii, F. 2005. Magnetic Alignment of Chiral Nematic Phase of Cellulose Microfibril Suspension *Langmuir*, 21 (5): 2034–2037.

Kong, C. U. o. H. 2013. *Basic principle of transmission electron microscope*. Available: http://www.hk-phy.org/atomic_world/tem/tem02_e.html (Accessed

Kopania, E., Wietecha, J. and Ciechańska, D. 2012. Studies on Isolation of Cellulose Fibres from Waste Plant Biomass. *FIBRES & TEXTILES in Eastern Europe*, 20 (6B): 167-172.

Kumar, A., Negi, Y., Choudhary, V. and Bhardwaj, N. 2013. Characterization of Cellulose Nanocrystals Produced by Acid-Hydrolysis from Sugarcane Bagasse as Agro-Waste. *Journal of Materials Physics and Chemistry*, 2 (1): 1 - 8.

Kumar, S., Reena, Chaudhary, S., Sweetey and Jain, D. 2014. Vibrational Studies of Different Human Body Disorders Using FTIR Spectroscopy. *Open Journal of Applied Sciences*, 4: 103-129.

Lavoine, N., Desloges, I., Dufresne, A. and Bras, J. 2013. Microfibrillated cellulose – Its barrier properties and applications in cellulosic materials: A review. *Carbohydrate Polymers*, 90 (2): 735– 764.

- Li, J., Wei, X., Wang, Q., Chen, J., Chang, G., Kong, L., Su, J. and Liu, Y. 2012. Homogeneous isolation of nanocellulose from sugarcane bagasse by high pressure homogenization. *Carbohydrate Polymers*, 90: 1609– 1613.
- Li, M., Wang, L., Li, D., Cheng, Y. and Adhikari, B. 2014. Preparation and characterization of cellulose Nanofibers from de-pectinated sugar beet pulp. *Carbohydrate Polymers*, 102: 136– 143.
- Liu, D., Chen, X., Yue, Y., Chen, M. and Wu, Q. 2011. Structure and Rheology of Nanocrystalline Cellulose. *Carbohydrate Polymers*, 84: 316–322.
- Lois-Correa, J. A. 2012. Depithers for Efficient Preparation of Sugar Cane Bagasse Fibers in Pulp and Paper Industry. *XIII, XIII* (4): 17-424.
- Lu, P. and Hsieh, Y. 2012a. Cellulose Isolation and Core–shell Nanostructures of Cellulose Nanocrystals from Chardonnay Grape Skins. *Carbohydrate Polymers*, 87: 2546– 2553.
- Lu, P. and Hsieh, Y. 2012b. Preparation and characterization of cellulose nanocrystals from rice straw. *Carbohydrate Polymers*, 87: 564– 573.
- M. Roohani, Y. H., N. Belgacem, G. Ebrahim, A. Karimi, A. Dufresne. 2008. Cellulose whiskers reinforced polyvinyl alcohol copolymers nanocomposites. *European Polymer Journal*, 44: 2489–2498.

M. Sain, S. P. 2006. Bioprocess preparation of wheat straw fibers and their characterization. *Industrial Crops and Products*, 23: 1 - 8.

Maiti, S., Jayaramudu, J., Dasa, K., Reddy, S. M., Sadiku, R., Ray, S. S. and Liu, D. 2013. Preparation and characterization of nano-cellulose with new shape from different precursor. *Carbohydrate Polymers*, 98: 562– 567.

Mandal, A. and Chakrabarty, D. 2011. Isolation of Nanocellulose from Waste Sugarcane Bagasse (SCB) and its Characterization. *Carbohydrate Polymers*, 86: 1291– 1299.

Mariño, M., Silva, L. L. d., Durán, N. and Tasic, L. 2015. Enhanced Materials from Nature: Nanocellulose from Citrus Waste. *Molecules*, 20: 5908-5923.

Menezes, J. d., Siqueira, G., Curvelo, A. and Dufresne, A. 2009. Extrusion and characterization of functionalized cellulose whiskers reinforced polyethylene nanocomposites. *Polymer*, 50 (19): 4552–4563.

Missoum, K., Martoia, F., Belgacem, M. and Bras, J. 2013. Effect of chemically modified nanofibrillated cellulose addition on the properties of fiber-based materials. *Industrial Crops and Products*, 48: 98– 105.

N. L. Garcia de Rodriguez, W. T., A. Dufresne 2006. Sisal cellulose whiskers reinforced polyvinyl acetate nanocomposites. *Cellulose*, 13 (3): 261-270.

N. Lin, J. H., A. Dufresne. 2012. Preparation, properties and applications of polysaccharide nanocrystals in advanced functional nanomaterials: a review. *Nanoscale*, 4: 3274 – 3294.

Nanotechnology, C. f. S. 2013. *how-i-study-nanoparticles-interactions-with-biological-soup*. Available: <http://sustainable-nano.com/2014/07/07/how-i-study-nanoparticles-interactions-with-biological-soup/> (Accessed 15 June 2015).

Normand, M. L., Moriana, R. and Ek, M. 2014. Isolation and Characterization of Cellulose Nanocrystals from Spruce Bark in a Biorefinery Perspective. *Carbohydrate Polymers*, 111: 979–987.

O'Connor, M. N. a. R. 1960. Relation of certain infrared bands to cellulose crystallinity and crystal latticed type. Part I. Spectra of lattice types I, II, III and of amorphous cellulose. *Journal of Applied Polymer Science*, 8 (3): 1311–1324.

Online, E. 2015. *Schematic Diagram XRD*. Available: <http://electronics.robotechno.us/tag/schematic-diagram-xrd> (Accessed 12 June 2015).

Pandey, A., Soccol, C., Nigam, P. and Soccol, V. 2000. Biotechnological potential of agro-industrial residues. I: sugarcane bagasse. *Bioresources Technology*, 74: 69 - 80.

Pereira, P. H., Voorwald, H. C., Coiffi, M. O., Mulinari, D. R., Luz, S. M. D. and Silva, M. L. D. 2011. Sugarcane Bagasse Pulping and Bleaching: Thermal and Chemical Characterization. *Bio-resources*, 6 (3): 2471-2482.

Sciences, P. L. a. A. Perkin-Elmer. 2005. FT-IR Spectroscopy Attenuated Total Reflectance (ATR)- Technical Note

PhotometricsInc. 2012. *Field Emission Scanning Electron Microscopy (FESEM)*. Available: <http://photometrics.net/analytical-techniques/field-emission-scanning-electron-microscopy-fesem> (Accessed 18 June 2015).

Ponce-Reyes, C., Chanona-Pérez, J., Garibay-Febles, V., Palacios-González, E., Karamath, J. and E. Terrés-Rojas, G. C. o.-D. 1. 2014. Preparation of Cellulose Nanoparticles from Agave Waste and its Morphological and Structural Characterization. *Revista Mexicana de Ingeniería Química*, 13 (3): 897-906.

Postek, M., Moon, R., Rudie, A. and Bilodeau, M. 2013. Production and Applications of Cellulose Nanomaterials. In: Michael T. Postek, R. J. M., Alan W. Rudie and Michael A. Bilodeau ed. United States of America: TAPPI Press.

Pranger, L. and Tannenbaum, R. 2008. Biobased Nanocomposites Prepared by In Situ Polymerization of Furfuryl Alcohol with Cellulose Whiskers or Montmorillonite Clay. *Macromolecules*, 41 (22): 8682–8687.

Q. Li, J. Z. a. L. Z. 2009. Structure and properties of the nanocomposite films of chitosan reinforced with cellulose whiskers. *Journal of Polymer Science Part B: Polymer Physics*, 47 (11): 1039–1129.

R. Maryana, D. M. r., A. Wheni I., Satriyo K.W., W. A. Rizal. 2014. Alkaline Pretreatment on Sugarcane Bagasse for Bioethanol Production. *Energy Procedia*, 42: 250 – 254.

R. Wilson, H. B. 2006. Introduction to Scanning Probe Microscopy (SPM), Basic Theory Atomic Force Microscopy (AFM). Northern Kentucky University.

Rainey, T. J. 2009. A study of the permeability and compressibility properties of bagasse pulp. Doctor of Philosophy, Queensland University of Technology.

Reddy, J. and Rhim, J. 2014. Isolation and Characterization of Cellulose Nanocrystals from Garlic Skin. *Material Letters*, 129: 20–23.

Roman, M. and Winter, W. T. 2004. Effect of Sulfate Groups from Sulfuric Acid Hydrolysis on the Thermal Degradation Behavior of Bacterial Cellulose. *Biomacromolecules*, 5: 1671 - 1677.

Rosli, N., Ahmad, I. and Abdula, I. 2013. Isolation and Charecterization of Cellulose Nanocrystals from Agave angustifolia Fibre. *Bio-resources*, 8 (2): 1893-1908.

S. Beck-Candanedo, M. R. a. D. G. G. 2005. Effect of Reaction Conditions on the Properties and Behavior of Wood Cellulose Nanocrystal Suspensions. *Biomacromolecules*, 6 (2): 1048–1054.

Santos, R. M. d., Neto, W. P., A.Silvério, H., Martins, D. F., Dantas, N. O. and Pasquinia, D. 2013. Cellulose Nanocrystals from Pineapple Leaf, a new Approach for Thereuse of this Agro-Waste. *Industrial Crops and Products*, 50: 707– 714.

Segal, L., Creely, J., Martin-Jr., A. and Conrad, C. 1959. An Empirical Method for Estimating the Degree of Crystallinity of Native Cellulose Using the X-Ray Diffractometer. *Textile Research Journal*, 29: 786 - 794.

Selective Permeability of Dialysis Tubing Lab: Explained. 2016. Available:

<http://schoolworkhelper.net/selective-permeability-of-dialysis-tubing-lab-explained/>

(Accessed 20 July 2016).

Sheltami, R., Abdullah, I., Ahmada, I., Dufresne, A. and Kargarzadeh, H. 2012. Extraction of Cellulose Nanocrystals from Mengkuang Leaves (*Pandanus tectorius*). *Carbohydrate Polymers*, 88: 772– 779.

Silvério, H., Neto, W., Dantas, N. and Pasquini, D. 2013. Extraction and characterization of cellulose nanocrystals from corncob for application as reinforcing agent in nanocomposites. *Industrial Crops and Products*, 44: 427– 436.

Siqueira, G., Bras, J. and Dufresne, A. 2009. Cellulose Whiskers versus Microfibrils: Influence of the Nature of the Nanoparticle and its Surface Functionalization on the Thermal and Mechanical Properties of Nanocomposites. *Biomacromolecules*, 10 (2): 425–432.

SMRI, S. M. a. R. I. 2013. <http://www.smri.org/sasugarindustry.php>. Available: <http://www.smri.org/smricontracts.php> (Accessed 03 May 2015).

Solomon, T. W. and Fryhle, C. B. 2011. *Organic Chemistry*. John Wiley & Sons, Inc.

Souza-Lima, M. D., Wong, J., Paillet, M., Borsali, R. and Pecora, R. 2003. Translational and Rotational Dynamics of Rodlike Cellulose Whiskers. *Langmuir*, 19 (1): 24 - 29.

Spiridon, I., Teaca, C. and Bodirlau, R. 2011. Structural changes evidenced by FTIR spectroscopy in cellulosic materials after pretreatment with ionic liquid and enzymatic hydrolysis. *Bioresources*, 6 (1): 400-413.

Stuart, B. 2005. *Infrared Spectroscopy: Fundamentals & Applications*. West Sussex, UK: John Wiley & Sons.

Sun, J., Sun, X., Zhao, H. and Sun, R. 2004. Isolation and Characterization of Cellulose from Sugarcane Bagasse. *Polymer Degradation and Stability*, 84: 331-339.

Sun, X., Xu, F., Sun, R., Fowler, P. and Baird, M. 2005. Characteristics of degraded cellulose obtained from steam-exploded wheat straw. *Carbohydrate Research*, 340 (1): 97 - 106.

Syverud, K. and Stenius, P. 2009. Strength and barrier properties of MFC films. *Cellulose*, 16 (1): 75-85.

Taipale, T., Österberg, M., Nykänen, A., Ruokolainen, J. and Laine, J. 2010. Effect of microfibrillated cellulose and fines on the drainage of kraft pulp suspension and paper strength. *Cellulose*, 17 (5): 1005-1020.

Technologies, P. 2005. *ATR Theory and Applications - Application Note - 0402*.

Teixeira, E., Bondanciaa, T., Teodoro, K., Corrêa, A., Marconcini, J. and Mattosoa, L. 2011. Sugarcane Bagasse Whiskers: Extraction and Characterizations. *Industrial Crops and Products*, 33: 63–66.

Terech, P., Chazeau, L. and Cavaille, J. Y. 1999. A Small-Angle Scattering Study of Cellulose Whiskers in Aqueous Suspensions. *Macromolecules*, 32 (6): 1872–1875.

Thakur, V. K. 2015. *Nanocellulose Polymer Nanocomposites - Fundamentals and Applications*. New Jersey, USA: Scrivener Publishing.

Troedec, M. L., Sedan, D., Peyratout, C., Bonnet, J., Smith, A., Guinebretiere, R., Gloaguen, V. and Krausz, P. 2008. Influence of Various Chemical Treatments on the Composition and Structure of Hemp Fibres. *Composites Part A : Applied Science and Manufacturing*, 39: 514–522.

University, I. T. 2012. *Polymer Science and Technology*. Istanbul, Turkey:

University, P. 2014. <https://www.purdue.edu/ehps/rem/rs/sem.htm#2>. Available: <https://engineering.purdue.edu/MSE/research/facilities/CharacterizationFacilities/AtomicForceMicroscopy> (Accessed 06 July 2015).

Wikipedia. 2014. *Atomic Force Microscopy*. Available: https://commons.wikimedia.org/wiki/File:AFM_schematic_%28EN%29.svg (Accessed 15 May 2015).

Wyman, C. 1999. BIOMASS ETHANOL: Technical Progress, Opportunities, and Commercial Challenges. *Annual Review of Energy and the Environment*, 24: 189 - 226.

Yang, H., Yan, R., Chen, H., Lee, D. and Zheng, C. 2007. Characteristics of hemicellulose, cellulose and lignin pyrolysis. *Fuels*, 86: 1781 - 1788.

Yu, M., Yang, R., Haung, L., Cao, X., F.Yang and Liu, D. 2012. Preparation and Characterization of Bamboo Nanocrystalline Cellulose. *Bio-resources*, 7 (2): 1808-1812.

Zhang, J., Elder, T., Pu, Y. and Ragauskas, A. 2007. Facile Synthesis of Spherical Cellulose Nanoparticles. *Carbohydrate Polymers*, 69: 607–611.

Zhao, X., Heide, E. v. d., Zhang, T. and Liu, D. 2010. Delignification of Sugarcane Bagasse with Alkali and Peracetic Acid and Characterization of the Pulp. *Bio-resources*, 5 (3): 1565-1580.

Zhou, C. and Wu, Q. 2012. Recent Development in Applications of Cellulose Nanocrystals for Advanced Polymer-Based Nanocomposites by Novel Fabrication Strategies. In: *Nanocrystals – Synthesis, Characterization and Applications*. Baton Rouge, Louisiana, USA: 103-120.

Zhou, W., Apkarian, R., Z. L. Wang and Joy, D. 2007. Fundamentals of Scanning Electron Microscopy. In: Zhou, W. and Wang, Z. L. eds. *Scanning Microscopy for Nanotechnology*.

APPENDICES

Preparation, Isolation and Characterization of Cellulose Nanocrystals from Soda Pulped Bagasse

Ditiro V. Mashego¹, Prashant Reddy^{1, 2}, Suprakas Ray³, Alain Dufresne⁴, Nirmala Deenadayalu^{1*}

¹Durban University of Technology, Steve Biko Campus, P. O. Box 1334, Durban, 4001

²Sugar Milling Research Institute NPC, c/o University of KwaZulu-Natal, Howard College Campus, Durban, 4041, South Africa

³CSIR National Centre for Nano-Structured Materials, Building 19B Scientia Campus, CSIR, Meiring Naude Road, Brummeria, Pretoria, 0184

⁴Grenoble Pagora INP International School of Paper, Print Media and Biomaterials
461 rue de la Papeterie - CS 10065 - 38402 Saint-Martin d'Hères Cedex, France

ABSTRACT

In this study cellulose nanocrystals were prepared from bleached sugarcane bagasse pulp. The experimental procedure included acid hydrolysis of the sugarcane bagasse pulp followed by separation of the nanocrystals using a centrifuge and characterization of the nanocrystals using different analytical and imaging techniques. The techniques used were: Dynamic Light Scattering (DLS) to determine particle size distribution, Attenuated Total Reflectance-Fourier Transform Infrared Spectroscopy (ATR-FTIR) for the study of the functional group composition of the samples, X-Ray Diffraction (XRD) in conjunction with FTIR spectroscopy to determine the crystallinity of the initial samples and the prepared nanocrystals, Atomic Force Microscopy (AFM), Scanning Electron Microscopy (SEM), Transmission Electron Microscopy (TEM) to study the morphology and rheology of the nanocrystals, and Thermogravimetric Analysis and Differential Thermogravimetry (TGA and DTG) to investigate the thermal stability of the untreated samples and the cellulose nanocrystals.

KEYWORDS

Nanocrystals, acid hydrolysis, microscopy, cellulose.

* To whom correspondence should be addressed

Email: NirmalaD@dut.ac.za

1. Introduction

Value added materials obtained from biomass are the building blocks for developing bio-refineries and a sustainable bio-based economy.¹ Biomass processing offers new and environmentally friendly routes for the production of novel products. Biomass represent the most abundant source of biomass with more than 100 billion tons produced by year, and only a small amount exploited (around 6 billion tons per year).² Increasing the value of lignocellulose fraction from biomass in novel applications is a target for increasing agricultural added value.

The sugarcane plant (*Saccharum officinarum*) can provide food for people, energy and feedstock for industry. Since sugar prices on the world market have been very low since the 1980s³, the diversification of the sugar industry is an urgent requirement in sugar-exporting countries.⁴ In recent years, there has been an increasing trend towards more efficient utilization of agro-industrial residues such as sugarcane bagasse (SCB), as starting materials for industrial applications. For each ten tons of sugarcane crushed for sugar production, 3 tons of wet bagasse is produced as waste.⁵ Sugarcane bagasse (SCB) is a residue produced in large quantities by the sugar and alcohol industries. It is the fibrous residue of sugarcane after undergoing conventional milling and is mainly used as a fuel to power the sugar mill. However, the remaining bagasse, about 50%, still continues to be pollute to the environment, a suitable and sustainable utilization of this residue has become an important objective to be pursued. Several processes and products have been reported that utilize SCB as a raw material. These include electricity generation, pulp and paper production, and products based on fermentation.⁶

About 40 -50% of sugarcane bagasse is the glucose polymer cellulose, much of which is in a crystalline structure. Another 25-35% is hemicelluloses, an amorphous polymer usually composed of xylose, arabinose, galactose, glucose, and mannose. The remainder is mostly lignin plus lesser amounts of mineral, wax, and other compounds.⁷ Figure 1 shows the cellulose monomer. This is the building block of the cellulose polymer, the major components of bagasse.

Cellulose is the most abundant polymer on Earth, representing about 1.5 trillion tons of total annual biomass production.⁸ It consists of glucose-glucose linkages arranged in linear chains where C-1 of every glucose unit is bonded to C-4 of the next glucose molecule as shown

in Figure 1. These chains aggregate along the chain direction with intermolecular hydrogen bonds and hydrophobic interactions. They form fibrous structures called nanofibrils 2 to 20 nm wide depending on biological species. These nanofibers make up the structure of all plants as well as some fungi, animals, and bacteria.⁹ These cellulosic Nano dimensional building blocks have crystalline regions, they have unique distinguishing properties. They have strength properties greater than Kevlar®, piezoelectric properties equivalent to quartz, can be manipulated to produce photonic structures, possess self-assembly properties, and are remarkably uniform in size and shape. In addition, because of their abundance, we can sustainably and renewably produce them in quantities of tens of millions of tons.

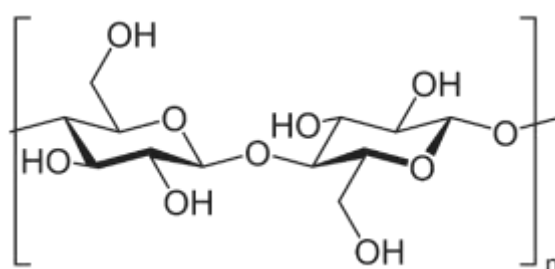


Figure 2 The cellulose monomer.

2. Experimental

2.1 Materials

Sodium hydroxide pellets, concentrated sulphuric acid were purchased from Aldrich and Fluka and were used without further purification. The sodium hydroxide used was 98-100% pure as indicated on the reagent bottle. The sulphuric acid was 98% v/v as indicated on the bottle. De-ionized water was used throughout the experimental procedure. Cellulose membrane with a molecular cut-off of 14 000 sourced from Union Carbide, USA was used in the dialysis

2.2 Experimental Procedure

The preparation of nanocellulose was adapted from literature.¹⁰ The method was adapted to suit the pulped bagasse.

(i) Neutralization of Soda Pulped Bagasse

50g of dry pulped bagasse was thoroughly rinsed in 1 3% w/v NaOH to remove any impurities and also to neutralize the pulp and aid in dispersing the cellulose fibres in solution. It was then strained with a nylon mesh to remove excess NaOH solution and then thoroughly rinsed with excess deionized water until the pH was neutral. Testing with a digital pH meter showed the pulp to have a pH 7 to 8. Sodium hydroxide absorbed by the pulp would decrease the concentration of the sulphuric acid used during the acid hydrolysis step. The neutralized pulp was analysed for moisture content using an OHAUS MB 35 moisture analyser.

(ii) Preparation of nanocellulose

An aqueous suspension of nanocellulose was prepared as follows. The neutralized and hydroxide free pulped bagasse, as obtained earlier was acid hydrolysed by treating with 60% (v/v) sulfuric acid. The water content of the pulp as determined after the neutralization was compensated by adding and corresponding amount sulphuric acid. The pulp was added using a fibre to liquor ratio of 1:20 and the hydrolysis performed for at 45 °C for 60 minutes¹¹ with strong agitation. The hydrolysis time was increased until the viscosity of the mixture was reduced and no fibre were visible when a very dilute sample of the hydrolysis mixture was viewed against sunlight in a glass vial. The hydrolysis was quenched by adding 10-fold excess iced water to the hydrolysis mixture. The resulting mixture was cooled to room temperature and centrifuged at 9500 rpm and 5 °C¹² using a Perkin Elmer refrigerated centrifuge. The fractions were dispersed and washed with 200ml deionized water, sonicated in an ultrasonic bath and re-centrifuged. The centrifugation process was stopped after five washings, while the resulting liquid turned into a milky white colloidal suspension. The suspension was then sonicated for 5 minutes. Ultrasonication and rapid cooling were done to stop the hydrolysis reaction and prevent overheating. A few drops of chloroform was added to the freshly prepared suspension to prevent degradation of the cellulose nanocrystals and stored in refrigerator at 4 °C. This solution was labelled CNC. The CNC solution was freeze dried, according to literature¹³, using a benchtop manifold freeze drier. The freeze dried CNC solution was labelled FD CNC. The solids separated during the centrifugation process were labelled as microcrystalline cellulose MCC.

2.3 Characterization of the Cellulose Nanocrystals

(i) Dynamic Light Scattering (DLS) Measurements

Particle size measurements have been widely employed in the characterization of cellulose nanocrystals. The measurements are used to determine the range of the particle size of the nanocrystals which is an indication of the extent of the hydrolysis reaction. Particle size distribution was determined using a HORIBA LB 550 (Dynamic Light Scattering) instrument. 5mL of the turbid aqueous suspension was placed in a quartz cuvette after shaking and the determination was performed between 10 – 1000 nm range.

(ii) Attenuated Fourier-Transform Infra-Red Spectroscopy

FTIR spectroscopy is the analytical technique of choice for monitoring functional group changes in biomass samples. A Perkin Elmer Spectrum 100 FTIR spectrometer equipped with an Attenuated Total Reflection Accessory was used. Dried pulped bagasse and pre-treated samples were used in the FTIR analysis. A 12 hour freeze dried sample of the cellulose nanocrystals suspension was used in the FTIR analysis. An average of 50 scans were performed in the region 4 000 – 600 cm^{-1} .

(iii) Wide Angle X-Ray Diffraction Studies

A PAN Analytical X'Pert PRO X-Ray Diffractometer fitted with a Cu $K\alpha$ radiation source was used to investigate the XRD spectra of the cellulosic sample was used. Scattered radiation was detected in the range $2\theta = 5 - 50^\circ$, at a speed of 3 $^\circ/\text{min}$ operating voltage and current of 45 kV and 40 mA respectively.

(iv) Thermogravimetric Analysis

Thermogravimetric studies were performed on a TA Q500 TGA. The heating rate was set at 5 $^\circ\text{C}/\text{min}$ from room temperature to 650 $^\circ\text{C}$ and the Nitrogen purge rate was 10 ml/min. All analyses were performed on platinum crucibles which were washed in nitric acid and dried before use.

2.4 Microscopic Analysis

(i) Atomic Force Microscopy

A Digital instruments Nanoscope, Veeco, MMAFMLN-AM Atomic Force Microscope was used to characterize the morphology and dimensions of the prepared nanocrystals. After dilution and sonication to promote dispersion, a drop was of the aqueous suspension was dried on a glass substrate, dried at ambient temperature and analysed using tapping mode.¹⁰

(iii) Scanning Electron Microscopy Studies

Scanning electron micrographs of untreated pulped bagasse, microcrystalline cellulose and cellulose nanocrystals were captured using a JEOL- JSM 7500F Field Emission - Scanning Electron Microscope. Prior to imaging, the samples were coated using the gold sputtering method.¹⁰

(iv) Transmission Electron Microscopy

Transmission electron micrographs were captured using a JEOL-Jem 2100 with a Leica EMFC6 (LN2 attachment). A dilute aqueous suspension of the nanocrystals was sonicated and deposited on a carbon substrate on a copper grid where it was allowed to dry at room temperature and subsequently viewed.

3. Results and Discussion

(i) Dynamic Light Scattering (DLS) Measurements

Figures 2 and 3 below show the particle size (volume) percent and particle number results respectively for the prepared CNC solution.

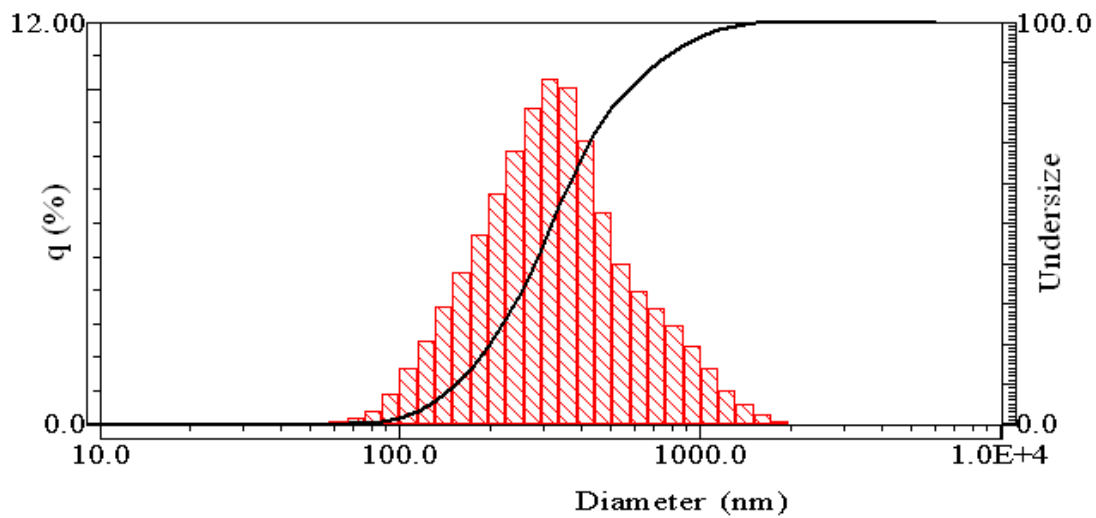


Figure 3 Distribution curve for CNC volume percent.

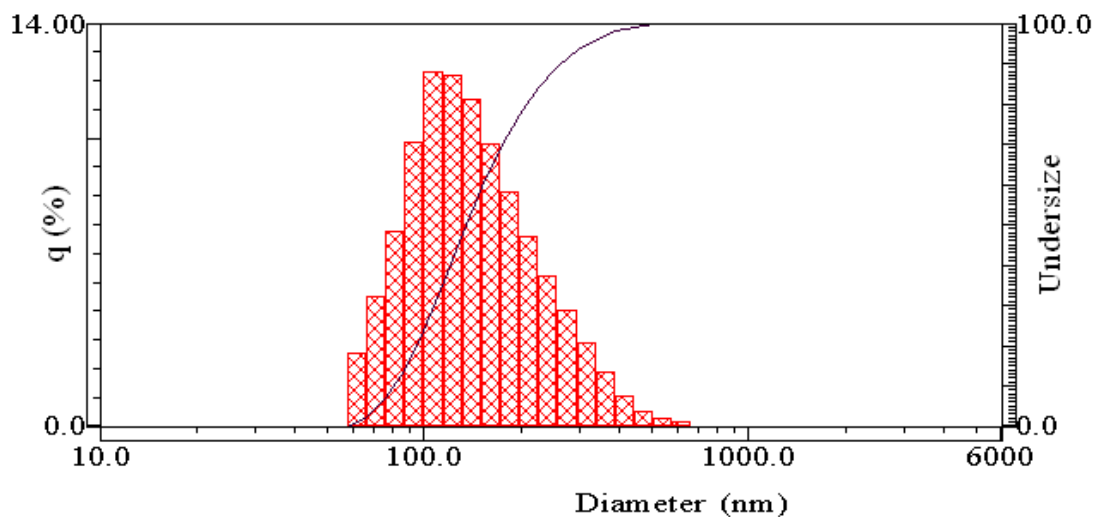


Figure 4 Distribution curve for CNC particle volume number.

Figures 2 and 3 show a homogenous distribution of the particle volume and number over the illustrated ranges. The distribution range of the diameter of the CNC particles was between 66 nm and 1.98 μm . The CNC data shows that diameter of the smallest particle of the prepared nanocrystals is 66nm which is accountable for nearly 0.1% of the volume fraction. The distribution peaked at 339 nm which had 39% of the volume fraction. 79% of the nanocrystals prepared had a diameter less than 500 nm.

The distribution curve for the CNC volume number in Figure 3, showed that all the nanocrystals produced were in the nanometre range. The particle number distribution peaks at

115 nm and then decreased with increasing size of the prepared cellulose nanoparticles. The largest particle size group was found to be 669nm in diameter which accounted for less than 0.15 % of the particles. 12,3 % of the particles number distribution belonged to particles 115 nm in diameter.

(ii) Fourier Transform Infra-red Spectroscopy

Figure 4 below shows the combined FTIR spectra of pulped bagasse, MCC and FD CNC. The band between $3500\text{-}3200\text{ cm}^{-1}$ for all spectra corresponds to the O-H stretching vibration of the hydroxyl groups in cellulose, hemicellulose and lignin.¹⁴ The characteristic band at 2891 cm^{-1} in all spectra corresponds to the C-H stretching vibration of alkyl groups in aliphatic bonds of cellulose, lignin and hemicellulose.¹ The band between $1700\text{--}1650\text{ cm}^{-1}$ corresponds to the C=O stretching vibration of the acetyl and uronic ester groups, from pectin, hemicellulose or the ester linkage of carboxylic group of ferulic and p-coumaric acids of lignin and/or hemicellulose.¹⁰

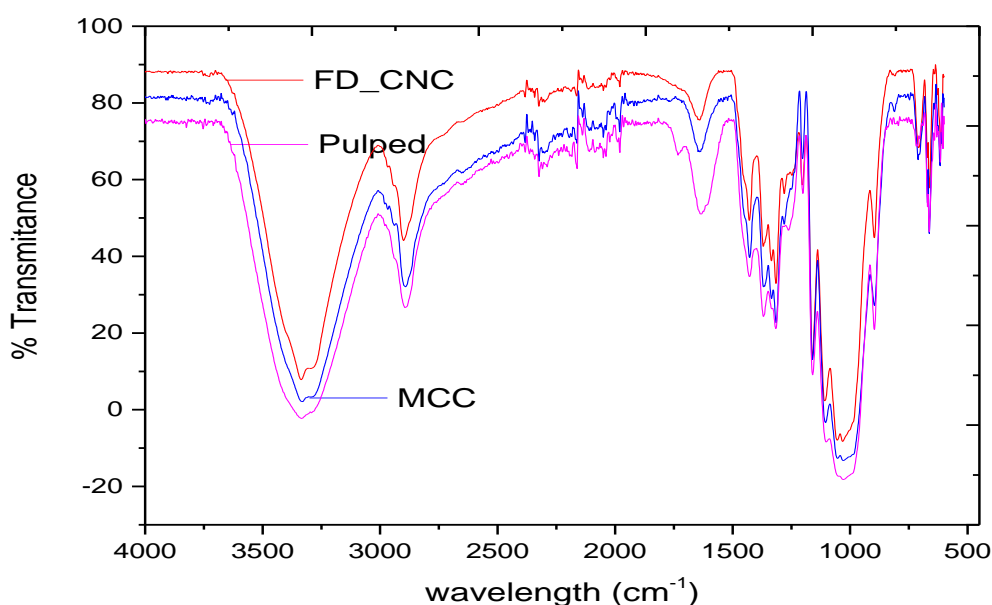


Figure 4 Combined spectra of Pulped bagasse, MCC and FD CNC.

This band is not visible for MCC and CNC. Cellulose does not contain any C=O and therefore this band cannot be attributed to any vibrations within the cellulose

polymer. This is due to alkali treatment which drastically reduced the hemicellulose and lignin content of the pulped bagasse. A band positioned around 1640 cm^{-1} corresponds to the O-H bending of water absorbed into cellulose fibre structure and is present in all samples.^{14,15} The bands located at 1500 cm^{-1} and around 1400 cm^{-1} are associated with the aromatic C=C in plane symmetrical stretching vibration of aromatic ring present in lignin.¹⁰ The peak at 1245 cm^{-1} as present only in spectra of pulped bagasse corresponds to the C–O out of plane stretching vibration of the aryl group in lignin.¹⁶ FTIR spectra of pure CNCs having sharp bands but similar to that observed in the pulped bagasse and MCC. The bands at $1430\text{-}1420\text{ cm}^{-1}$ are due to CH₂ scissoring vibrating motion in cellulose¹⁷, $1382\text{-}1375\text{ cm}^{-1}$ (C-H bending), 1336 (O-H in plane bending) 1317 cm^{-1} (CH₂ wagging), 1054 cm^{-1} (C–O–C pyranose ring stretching vibration), $902\text{-}893\text{ cm}^{-1}$ (associated with the cellulosic β -glycosidic linkages), around 1150 cm^{-1} (C–C ring stretching band), and at 1105 cm^{-1} (the C–O–C glycosidic ether band).^{16,18} The band at 895 cm^{-1} corresponds to cellulose¹⁷ and an increase in the absorbance of this band corresponds with removal of amorphous cellulose and the increased availability of the crystallite portion of the crystalline cellulose polymer.¹⁹

The crystallinity of the samples can be calculated using the IR bands between $1500 - 850\text{ cm}^{-1}$.^{13,20} This only applies to samples containing cellulose I or cellulose II or a mixture of the two and or the amorphous cellulose.²¹ The above mentioned IR region is sensitive to crystal structure of the cellulosic material. Spectral bands at $1420\text{-}1430\text{ cm}^{-1}$ and $893\text{-}897\text{ cm}^{-1}$ are very important to explain the crystal structure of cellulosic material.²² The following ratios show how the Lateral Orientation index (LOI) and the Total Crystallinity Index (TCI) are calculated using IR ratios:

$$\text{Lateral Orientation Index (LOI)} = \frac{1430\text{cm}^{-1}}{890\text{cm}^{-1}} \quad 21$$

Equation 1 Lateral Orientation Index calculated using IR ratios.

$$\text{Total Crystallinity Index (TCI)} = \frac{1375\text{cm}^{-1}}{2900\text{cm}^{-1}}$$

Equation 2 Total Crystallinity Index calculated using IR ratios.

An increase in both LOI and TCI ratios was observed from pulped bagasse to MCC to CNC as can be seen in in Table 1. An increase in these ratios corresponds to the formation of ordered crystallite within the samples. Higher value of the given index (LOI, TCI) reveals that the given material contains a highly crystalline and ordered structure. This can be attributed to the removal of amorphous cellulose as the acid hydrolysis separates the amorphous cellulose from the cellulose crystallites to form the nanocrystals.¹⁷

(iii) Wide Angle X-Ray Diffraction Studies

Figure 5 below shows the combined X-ray diffractograms of pulped bagasse, MCC and FD CNC. The figure shows characteristic cellulose peaks around $2\theta = 15$ and 22.5° . The XRD profiles are similar suggesting that all three samples contain cellulose.

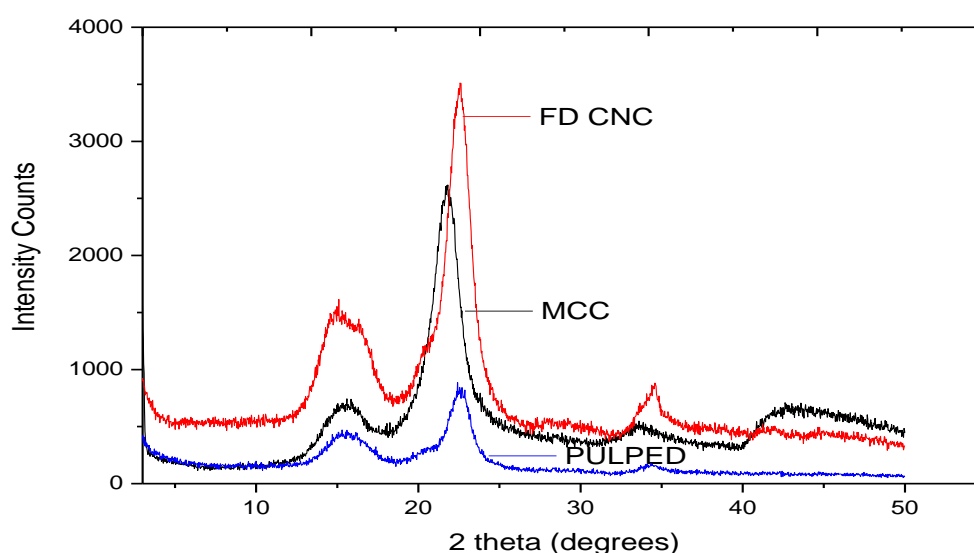


Figure 5 Combined X-ray diffractograms of pulped bagasse, MCC and FD CNC.

$$CrI = \frac{I_{200} - I_{am}}{I_{200}} \times 100$$

Equation 3 Percent Crystallinity calculated using XRD intensities.

	TCI	LOI	CrI
Pulped Bagasse	0.99	0.962	41.28
MCC	1.10	1.231	53.93
FD CNC	1.06	1.245	46.31

Table 1 The TCI, LOI and CrI calculated using XRD intensities and

An increase in crystallinity index was observed from pulped bagasse to MCC to CNC. It can be seen from diffractograms that the fibres show increasing crystalline orientation along a certain axis after subsequent treatment as the non-cellulosic amorphous polysaccharides are removed and the highly crystalline cellulose is left over. All three diffractograms display two well-defined peaks around $2\theta = 15.5^\circ$ (for 1 1 0 plane) and $2\theta = 22.5^\circ$ (for 2 0 0 plane). These two planes are characteristic of cellulose.^{12, 24-26}

The final increase in percent crystallinity was due to the acid hydrolysis. Literature references^{14, 27, 28} show CrI values of 39,%, 54,9 % and 63,0 % respectively when calculating for the percent crystallinity index. The CrI obtained in this study was found to be 46, 3%. Literature references^{10, 29} who used sugarcane bagasse as their source of cellulose fibres show a trend of increasing CrI values as the CNC are isolated from the bagasse. The results of the XRD studies collaborated with those from the FTIR studies which also show an increase in the crystallinity indices.

(iv) Thermal Analysis (TGA & DTG)

Figure 6(a) and Figure 6(b) show the combined TGA and the DTG profiles of pulped bagasse, MCC and FD CNC respectively.

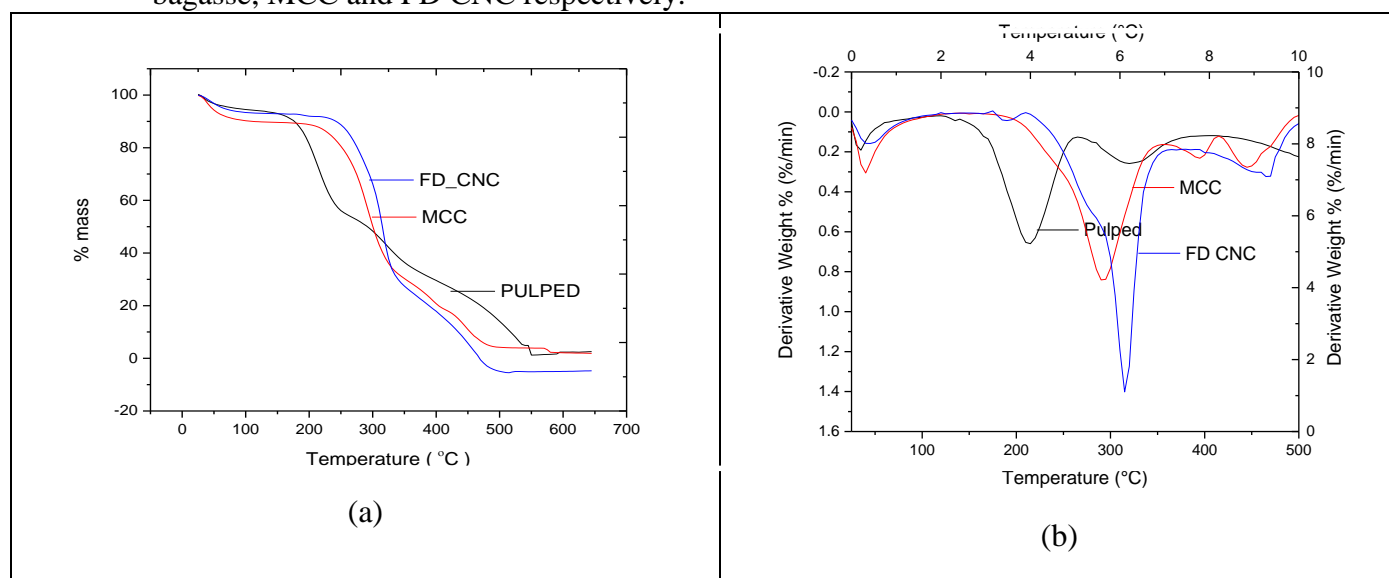


Figure 6 The combined TGA DTG curves of Pulped Bagasse, MCC and FD CNC.

The TGA curves showed three degradation steps related to moisture evaporation, hemicellulose, cellulose and lignin degradation. From the TGA curves above it is clear to see that from 25 -120 °C there is a slight decrease in the mass of all samples. This is due to the removal of surface bound moisture on the samples being removed. The degradation onset temperature of pulped bagasse was the lowest at 190 °C due to a higher content of lignin and hemicellulose. After the initial mass loss of about 10% due to moisture content, the degradation of pulped bagasse was a multi stage degradation starting at 190 - 270 °C. This degradation was responsible for about 30% of the total mass loss of the sample. The DTG curve of pulped bagasse shows two prominent peaks at 210 °C and at 320 °C. The two peaks are for the amorphous and crystalline cellulose respectively. The second step in the thermal degradation of pulped bagasse in Figure 6(a) was between 250 -325 °C. This accounted for 25 % of the total weight loss. The final step was accountable for 32% of the mass loss of sample. FD CNC exhibited a degradation profile wherein the onset temperature was higher than that of pulped bagasse. The onset degradation temperature of FD CNC as per the Figure 6(a) was about 250 °C. This was corroborated by Figure 6(b) which shows a shoulder on the

peak of the CNC. This shoulder, observed in the DTG curve, at around 300 °C likely reflects the presence of a portion of the hemicellulose.¹² Crystalline cellulose has a much ordered structure making it more thermally stable. The FD CNC were of higher purity and hence exhibited a smoother curve when subjected to similar degradation conditions. After the initial mass loss between 25 -120 °C due to the loss of surface bonded moisture, FD CNC started degrading at around 260 °C peaking at 310 °C. The lower degradation onset temperature of pulped bagasse compared to that of FD CNC is due to the presence of lignin, hemicelluloses and other non-cellulosic segment which decompose at low temperature.²⁹

Microscopic Analysis

(i) Atomic Force Microscopy (AFM)

The following AFM micrographs show the results obtained from an analysis of an aqueous solution of the prepared CNC nanocrystals.

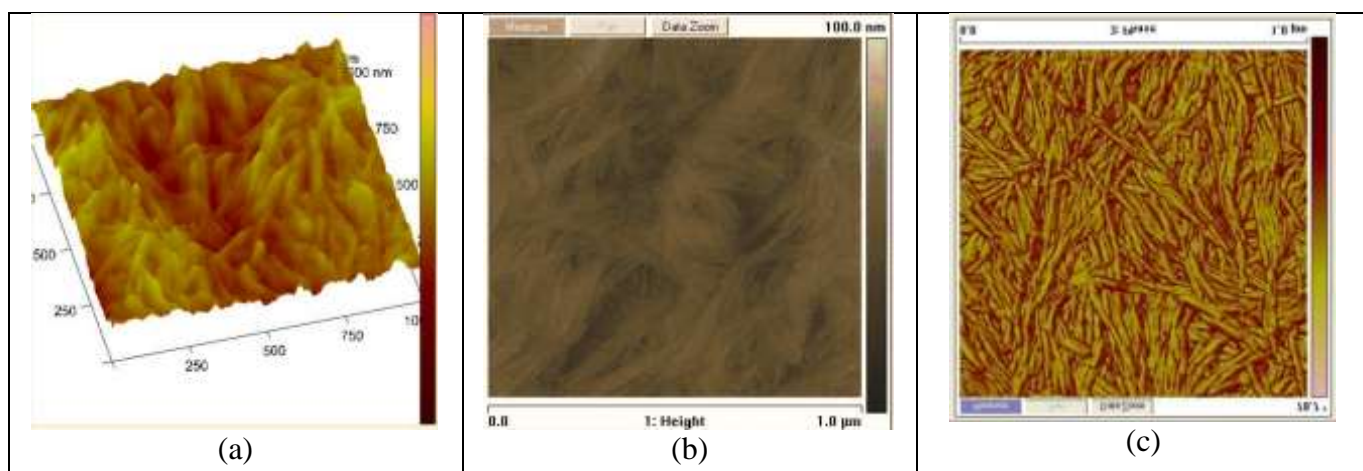


Figure 7 The 3D view, height and phase AFM images of FD CNC.

The atomic force micrograph of cellulose nanocrystals are shown above. A 3D view, height view and phase micrograph are shown in Figures 9 (a) to (c) respectively. From Figure 9(a) the dimension of the microcrystals are in the 300- 400 nm range. The 3D mode, Figure 9(a) is a combination of both the height and the amplitude scans which gives a clearer image of the crystals and their dimension. The phase mode micrograph, Figure 9(b) shows the majority of the agglomerated crystals to be less than 500nm in length. Though agglomeration during drying makes it difficult to see the length of an

individual nanocrystal, other techniques like DLS measurements and confer with these findings.

(ii) Field Emission Scanning Electron Microscopy (FE-SEM)

The following SEM micrographs shown were obtained after viewing pulped bagasse, MCC and CNC via SEM.

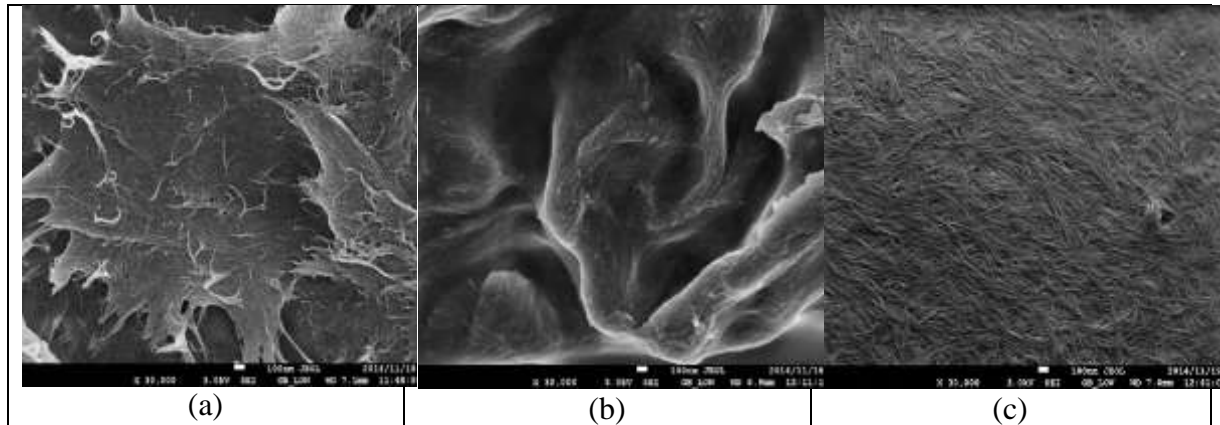


Figure 8 The SEM micrographs of Pulped bagasse, MCC and FD CNC

The FE-SEM micrographs of pulped bagasse, MCC and CNC are shown in Figure 9(a)-(c) respectively. Pulped bagasse contains cellulose fibres still bound by lignin and hemicellulose. The fibres are orientated in fibre axis direction. The soda pulping loosens the fibres to a certain extent allowing for easier acid hydrolysis. At this stage the fibres are bound by acid soluble lignin and hemicellulose. Partial acid hydrolysis yields the microcrystalline fibres which have a reduced diameter. Figure 9(b) shows the reduced fibres still bound by acid soluble components of biomass. Size reduction to the nanometre range Figure 9(c) is achieved by the prolonged hydrolysis which completely removes the amorphous cellulose and yields the nanocrystals with no apparent defect. From the pulped bagasse to the microcrystalline bagasse to the nanocrystals, it is evident that the acid hydrolysis was effective in removing the amorphous celluloses and reducing the fibre dimension. The nanocrystals have a high aspect ratio with lengths in the 250-350nm range.

(iii) Transmission Electron Microscopy (TEM)

The TEM micrographs shown below are of a dilute solution of the prepared CNC nanocrystals after sonication and drying at ambient temperature.

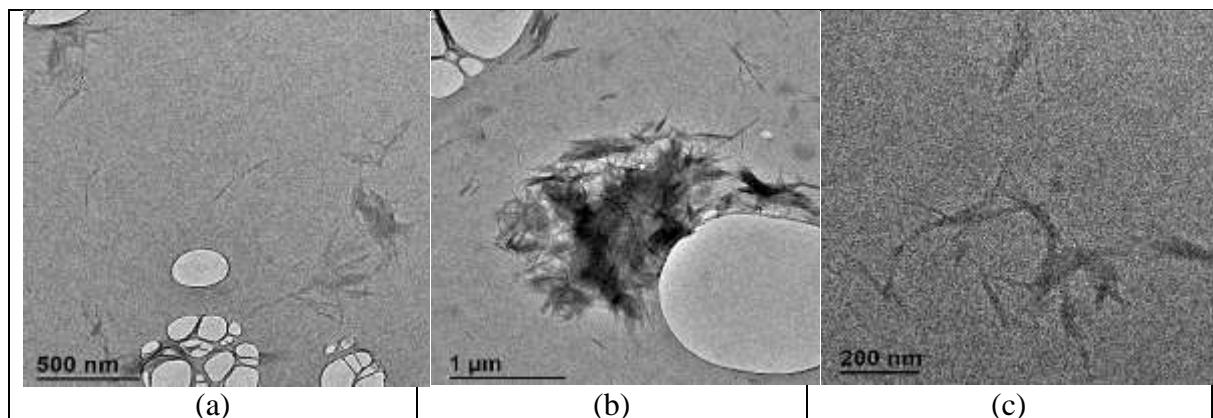


Figure 5 The TEM micrographs of FD CNC.

The TEM micrographs shown in Figure 9 (a) and (b) show cellulose nanocrystals which have agglomerated due to drying of the dilute aqueous suspension after sonication. The holes in both micrographs are due to the carbon substrate used to deposit drops on the copper grids during sample preparation. The average crystal size is in the 200 -300 nm range. The diameter of the crystals is nanometric giving them a high aspect ratio. Figure 9(c) clearly shows the nanocrystals. In this micrograph single crystal length and diameter can be clearly seen.

4. Conclusion

The soda pulped bagasse yielded nanocellulose with a reasonable content of cellulose. The Nanocellulose was obtained in the form of a stable milky white dispersion where the surface anionic charges help to bring forth the necessary stabilization of the nanocellulose. The TEM, SEM & AFM studies gave supporting evidence for the formation of nanocellulose. This observation was further been corroborated by given the DLS studies which indicate that majority of the hydrolysed particles lie in the Nano range. The crystallinity of the CNC depends is greatly affected by hydrolysis times. Extended hydrolysis times lead to partial degradation of the cellulose crystallites in the polymer. Different sources of cellulose require different hydrolysis times to reduce the size of the

cellulose particles to the Nano range. These hydrolysis times can be greatly reduced by appropriate pre-treatment of the lignocellulosic biomass being used as starting material.

5. Acknowledgements

The authors would like to acknowledge the National Research Foundation South Africa for a scholarship for D. Mashego, the staff at CSIR NCNSM- Pretoria and the Durban University of Technology.

6. References

1. B. Noorder, L. Jasinska-Walc, I. van der Meulen, R. Duchateau, C. Koning, Novel biomass-based polymers : synthesis, characterization and application. In *Biobased Monomers, Polymers and Materials*, American Chemical Society. : **2012**; pp 281 - 322.
2. E. Espino, M. Cakir, S. Domenek, A. Román-Gutiérrez, N. Belgacem, J. Bras, Isolation and Characterization of Cellulose Nanocrystals from Industrial by-products of Agave Tequilana and Barley. *Industrial Crops and Products* **2014**, *62*, 552 - 559.
3. J. Nyberg, *Sugar International Market Profile*; Markets and Trade Division, Food and Agriculture Organization of the United Nations: **2006**; pp 1-14.
4. C. Martin, M. Galbe, F. Wahlbom, B. Hahn-Hägerdal, L. Jönsson, Ethanol production from enzymatic hydrolysates of sugarcane bagasse using recombinant xylose-utilising *Saccharomyces cerevisiae*. *Enzyme and Microbial Technology* **2002**, *31*, 274 - 282.

5. B. Mtunzi, N. Mampwheli, E. Meyer, Wilson Mungwena, , Bagasse-based co-generation at Hippo Valley Estates sugar factory in Zimbabwe. *Journal of Energy in Southern Africa* **2012**, 23 (1), 15-22.
6. P. Singh, A. P., Biotechnology for Agro-Industrial Residues Utilisation: Utilisation of Agro-Residues. 2009; p. 241.
7. S. Jacobsen, C. Wyman, Xylose monomer and oligomer yields for uncatalyzed hydrolysis of sugarcane bagasse hemicelluloses at varying solids concentration. *Industrial & Engineering Chemistry Research* **2002**, 41 (6), 1454–1461.
8. M. Poletto, V. Pistor, A. Zattera, Structural Characteristics and Thermal Properties of Native Cellulose. In *Cellulose - Fundamental Aspects*, M. Poletto, V. P. a. A. J. Z., Ed. 2013; pp 45 - 68.
9. G. Siqueira, J. Bras and A. Dufresne, Cellulosic Bionanocomposites: A Review of Preparation, Properties and Applications. *Polymers* **2010**, 2, 728-765.
10. A. Mandal, D. Chakrabarty, Isolation of Nanocellulose from Waste Sugarcane Bagasse (SCB) and its Characterization. *Carbohydrate Polymers* **2011**, 86, 1291– 1299.
11. M. Haafiz, A. Hassana, Z. Zakaria, I. Inuwa, Isolation and characterization of cellulose nanowhiskers from oilpalm biomass microcrystalline cellulose. *Carbohydrate Polymers* **2014**, 103, 119– 125.
12. R. Sheltami, I. Abdullah, I. Ahmada, A. Dufresne, H. Kargarzadeh, Extraction of Cellulose Nanocrystals from Mengkuang Leaves (*Pandanus tectorius*). *Carbohydrate Polymers* **2012**, 88, 772– 779.
13. E. Dinand, M. Vignon, H. Chanzy, L. Heux, Mercerization of primary wall cellulose and its implication for the conversion of cellulose I→cellulose II. *Cellulose* **2002**, 9 (1), 7-18.

14. P. Lu, Y. Hsieh., Cellulose Isolation and Core–shell Nanostructures of Cellulose Nanocrystals from Chardonnay Grape Skins. *Carbohydrate Polymers* **2012**, *87*, 2546–2553.
15. M. Yu, R. Yang, L. Haung, X. Cao, F. Yang, D. Liu, Preparation and Characterization of Bamboo Nanocrystalline Cellulose. *Bio-resources* **2012**, *7* (2), 1808-1812.
16. A. Pandey, C. Soccol, P. Nigam, V. Soccol, Biotechnological potential of agro-industrial residues. I: sugarcane bagasse. *Bioresources Technology* **2000**, *74*, 69 – 80.
17. I. Spiridon, C. Teaca, R. Bodirlau, Structural changes evidenced by FTIR spectroscopy in cellulosic materials after pretreatment with ionic liquid and enzymatic hydrolysis. *Bioresources* **2011**, *6* (1), 400–413.
18. C. Wyman, Biomass Ethanol: Technical Progress, Opportunities, and Commercial Challenges. *Annual Review of Energy and the Environment* **1999**, *24*, 189 - 226.
19. M. Hubbe, O. Rojas, L. Lucia, M. Sain, Cellulosic Nanocomposites: A Review. *Bioresources* **2008**, *3* (3), 929–980.
20. N. Lin, J. Huang, A. Dufresne, Preparation, properties and applications of polysaccharide nanocrystals in advanced functional nanomaterials: a review. *Nanoscale* **2012**, *4*, 3274 – 3294.
21. F. Hurtubise, H. Krasig, Classification of Fine Structural Characteristics in Cellulose by Infrared Spectroscopy. Use of Potassium Bromide Pellet Technique. *Analytical Chemistry* **1960**, *32* (2).
22. X. Sun, F. Xu, R. Sun, P. Fowler and M. Baird, Characteristics of degraded cellulose obtained from steam-exploded wheat straw. *Carbohydrate Research* **2005**, *340* (1), 97 - 106.

23. M. Nelson, R. O'Connor, Relation of certain infrared bands to cellulose crystallinity and crystal latticed type. Part I. Spectra of lattice types I, II, III and of amorphous cellulose. *Journal of Applied Polymer Science* **1960**, 8 (3), 1311–1324.
24. L. Segal, J. Creely, A. Martin Jr., C. Conrad, An Empirical Method for Estimating the Degree of Crystallinity of Native Cellulose Using the X-Ray Diffractometer. *Textile Research Journal* **1959**, 29, 786 – 794
25. X. Zhao, E. van der Heide, T. Zhang, D. LiuX. Zhao, E. v. d. H., T. Zhang and D. Liu, Delignification of Sugarcane Bagasse with Alkali and Peracetic Acid and Charecterization of the Pulp. *Bio-resources* **2010**, 5 (3), 1565-1580
26. D. Liu, X. Chen, Y. Yue, M. Chen, Q. Wu, Structure and Rheology of Nanocrystalline Cellulose. *Carbohydrate Polymers* **2011**, 84, 316–322.
27. C. Ponce-Reyes, J. Chanona-Pérez, V. Garibay-Febles, E. Palacios-González, J. Karamath, E. Terrés-Rojas, G. Calderón-Domínguez, Preparation of Cellulose Nanoparticles from Agave Waste and its Morphological and Structural Characterization. *Revista Mexicana de Ingeniería Química* **2014**, 13 (3), 897-906
28. J. Reddy, J. Rhim, Isolation and Characterization of Cellulose Nanocrystals from Garlic Skin. *Material Letters* **2014**, 129, 20–23.

29. A. Kumar, Y. Negi, V. Choudhary, N. Bhardwaj, Characterization of Cellulose Nanocrystals Produced by Acid-Hydrolysis from Sugarcane Bagasse as Agro-Waste. *Journal of Materials Physics and Chemistry* **2013**, 2 (1), 1 - 8.